A search for $t\bar{t} \rightarrow$ *electron* + $\not\!\!E_T$ + *jets* signature in $p\bar{p}$ collisions at $\sqrt{s} = 1.8$ TeV with the DØ detector

A Dissertation Presented

by

Dhiman Chakraborty

to

The Graduate School

in Partial Fulfillment of the Requirements

for the Degree of

Doctor of Philosophy

in

Physics

State University of New York
at
Stony Brook

September 1994

State University of New York
at Stony Brook

The Graduate School

Dhiman Chakraborty

We, the dissertation committee for the above candidate for the Doctor of Philosophy degree, hereby recommend acceptance of the dissertation.

---

dissertation director
Professor Roderich J. Engelmann

---

chairman of defense
Professor Paul D. Grannis

---

committee member
Professor Jack Smith

---

outside member
Dr. Serban D. Protopopescu
Physics Department, Brookhaven National Laboratory

This dissertation is accepted by the Graduate School.

Graduate School

Abstract of the Dissertation

A search for $t\bar{t} \rightarrow$ *electron* + $\not\!\!E_T$ + *jets* signature in $p\bar{p}$ collisions at $\sqrt{s} = 1.8$ TeV with the DØ detector

by

Dhiman Chakraborty

Doctor of Philosophy

in

Physics

State University of New York at Stony Brook

1994

A search has been carried out for the production of $t\bar{t}$ in $p\bar{p}$ collisions at a center-of-mass energy of 1.8 TeV in the final state signature consisting of a single isolated electron, missing E_T and multiple jets using the DØ detector. The data corresponds to an integrated luminosity of 13.5 ± 1.6 pb^{-1} collected during the 1992-1993 run of the Tevatron collider at Fermilab. The analysis exploits the differences in kinematic as well as topological features of signal and backgrounds assuming the predictions of the Standard Model for the production and decay of top (t) quarks. The search was fo-

cused in the region of top mass (M_t) above the current lower limit of 131 GeV obtained from a previous analysis of the same data set. The cross-section for the process calculated using different methods are consistent within experimental uncertainties. We obtain a mean value of $\sigma(t\bar{t} \rightarrow p\bar{p}) = 5.1 \ \pm 7.9$ (stat.) ± 1.3 (sys.) pb with an upper limit of 29.0 pb (95% C.L.) for $M_t \approx 160$ GeV. This result is consistent with theoretical calculations and results from other experiments.

To my parents.

Acknowledgements

It is more than a word of thanks that I owe to the many people who have made my life as a graduate student, the past six years, an enriching experience. I hope to be able to reciprocate someday by giving, perhaps to another set of people, what I have received from these.

First, I would like to thank my advisor, Rod Engelmann, for advising me no more than necessary, no less than sufficient. His practical, straightforward and patient approach to every issue set an example for me.

Being a strand in the strong and colorful fabric of DØ has been simply wonderful. I am honored to have had the opportunity to work with such a dedicated bunch who have taught me the meaning of teamwork and camaraderie. I wonder what it takes to lead a team of such size and variety the way Paul Grannis has done over the past ten years with such amazing success.

I am thankful to the entire high-energy group at Stony Brook for inspiring my interest in the subject in the first place. Special thanks are due to Qizhong Li-Demarteau and Domenico Pizzuto who were my mentors in the subject of CDC software, the main area of my involvement in the "public service" sector at DØ . After moving to Fermilab, I learnt a great deal about the CDC also

from Jim Cochran, Joey Thompson and Chris Klopfenstein. Working with the Central Detector (CD) group was fun in general. Srini Rajagopalan taught me the little I came to know about DBL3 in course of developing the online monitoring routine for the CDC. I am grateful to Paul Rubinov who was quick to relieve me of my CDC responsibilities when I was feeling compelled to appropriate more of my time to thesis research.

I received a lot of guidance help from Rajendran Raja and Meenakshi Narain while working as a member of the electron-id group.

I thank Jim Cochran for suggesting the topic of this thesis to me. Following that, it is the top group that made the past three years of my life worth living. Most of my thesis research was done in close collaboration with Serban Protopopescu although I received useful inputs more or less from all of the members of the group. In particular, I am deeply indebted to Raja and Serban who, beside leading the group ably until a few months ago, acted as my mentors throughout this period. Guidance, encouragement, criticism or just an open ear: they provided whenever I sought or needed any. I learnt a lot by watching them.

Walter Giele, the author of VECBOS, merits a special mention for many enlightening discussions about the main background process ($W + jets$) as well as the signal. I am deeply indebted to Chip Stewart for incorporating VECBOS at DØ and teaching me its fundamentals. Jae Yu also helped me in my first encounters with VECBOS. Much of the work on the non-W background was done in collaboration with Mirek Fatyga. The hours of discussions I had with him proved very useful to me. Rich Astur was always quick and willing to

respond to my endless questions on the topic of jet energy correction.

The life at the Stony Brook ghetto will remain a cherished memory for years to come. Marc (Paterno) and Jae, aside from answering all my stupid calorimeter questions, helped me along with Jim and Joey, with many stimulating discussions not only on physics, but on just about anything under the sun. A special note of thanks goes to Jim for proof-reading my thesis more thoroughly than I ever hope to do myself. Scott Snyder has been a Genie in granting me my software wishes ... I hope to come up with a software question someday for which he doesn't have an answer. Dan Claes has always been willing to explain the trigger issues to me whenever I have asked.

Among the friends I made as a graduate student but outside DØ , a special mention is due to Renu Joseph, Arul Lakshminarayan and Hidayat Hasan. I shall cherish their friendship forever.

For the past few months, I have found a fun gang to hang around with among the bozos at the 8, Sauk Circle (if-you-have-nothing-to-do-just-park-here), Sailesh, Vipin, Mrinmoy and some of their semi-permanent guests. I am mentioning them here only because they said that it would hurt their feelings if I didn't. Brajesh has always been a good friend to volunteer a helping hand whenever my perspective on life has needed straightening.

No words can express my debt to my family: my parents, my wife and my sister who have always put my interests before theirs. Whatever I am and whatever I shall be, I owe it all to them.

Contents

List of Figures

List of Tables

Chapter 1

Introduction

"So, Nat'ralists observe, a Flea
Hath smaller fleas that on him prey
And these have smaller fleas to bite 'em,
And so proceed ad infinitum."
— Jonathan Swift

It has been many millenia since the first human to ask himself, "What are I and everything around me made of?" breathed his last. Yet, the question is very much alive and kicking more vigorously today than ever before as we continue our intriguing quest for the fundamental building blocks of the universe. Over the centuries, our understanding of nature's ingredients has taken a tortuous path through rare successes and frequent failures of theories and experiments to where it has reached today. We have learnt that the reply to the question, "What is the universe made of?" is "How closely do you care to look?" And ever since, we have striven tirelessly to look closer and closer. As our inward journey into the heart of the matter continues to gain

momentum, surprises keep popping up from the horizon which continues to hide the "final and complete" answer. And every once in a while we can't help but tip our hats to the guy who conceived the whole mess in the first place.

For various reasons that we will come across in this chapter, theoretical expectations for the existence of the *top* or *"t"* quark, the sixth member of a family of fundamental pointlike particles as we know them today, are extremely high. The remaining five have been experimentally observed and the sixth is now of crucial importance: proof of its existence will be a powerful vindication for today's best theoretical model which successfully explains all the experimental observations while proof on the contrary would deal a fatal blow to it. Such is the context that motivates the work to be presented in this thesis.

In the first section of this chapter, we will give a brief account of the history that has led to the current state of affairs. In the next section, we will quickly review the "Standard Model" which best accommodates all the experimental observations made to date, requiring the least beyond. Finally, in the last section, we shall discuss the relevance and the scheme of our work.

1.1 History

More than five thousand years ago, the Hindu scholars of India postulated the universe to be composed of five fundamental elements: earth, water, fire, air and sky. Views not too dissimilar prevailed in other civilizations as well. Gradually, the understanding of elemental composition of matter evolved and

chemists of ancient times were successful in isolating metals from their ores to remarkable purity. By the end of the eighteenth century, most of the stable chemical elements had been discovered. Still, all materials could be argued to be continuous, sidestepping the question of the smallest unit of matter.

The atomic nature of matter began tickling the philosophers' fancy before the birth of Christ, but technological limitations forbade the testing of their hypotheses until about two hundred years ago. The chemists of the late eighteenth century were able to identify many gaseous substances and isolate them to good purity. Immediately, they took note of the fact that equal volumes of light gases at the same temperature and pressure bear ratios of small integers between their weights. This was the first hint that there may be some lowest common denominator after all. The ensuing deductions from numerous experiments on chemical analysis and synthesis of compounds established the atomic picture of matter on a firm ground.

The curious repetitive pattern in the chemical properties of the elements that Mendeleev listed in increasing order of atomic weights (the name "periodic table" says it all) made a suggestion of subatomic structures that was too strong to deny. Subsequently, a series of experiments culminating in one by Thomson in 1897 established electrons in bound state to be a component of the atom [1]. Studies of the behavior of electrons in free as well as bound states and research on its applications led to a revolution, still in progress, unparalleled in the history of human civilization. In 1911, Rutherford's scattering of doubly ionized helium atoms (α particles) on a thin foil of gold led him to deduce that the positive charge in an atom occupies a negligible fraction of its volume,

yet accounts for almost all of its mass. This volume containing the positive charge of an atom was named "nucleus". The nucleus of hydrogen, the lightest element, was called "proton". James Chadwick's experiment in 1932 proved the existence of "neutron", the electrically neutral particle of about the same mass as proton, in heavier nuclei [2]. Thus, by the 1930's, electron, proton and neutron were able to serve as the complete set of fundamental building blocks of matter. However, some "curious" phenomena such as the nuclear β emission in a continuous spectrum discovered by Chadwick in 1914 [3] and the binding of protons in the nucleus remained unresolved.

Meanwhile, advances were being made at the theoretical front at an incredible speed. Maxwell's theory of electromagnetism formulated in the 1860's laid the firmest of groundings. Planck's study of black-body radiation followed by the discovery of the photoelectric effect resulted in the deduction of the quantum nature of electromagnetic radiation by Planck and Einstein in 1905. In 1913, Bohr combined the "nuclear" model of the atom with the quantum theory of light to form the basis of his famous theory of the hydrogen atom [4].

In 1915, Einstein formulated the general theory of relativity, one of the most important elements in the present-day understanding of physics and cosmology. Quantum mechanics, the other theory to play a key role, came into being in the 1920's as Shrödinger's wave equation modelled the hydrogen atom successfully from a probabilistic viewpoint and Heisenberg's uncertainty principle paved the way to the formulation of operator algebra of physical observables. A breakthrough of crucial importance was achieved when Dirac com-

bined the theory of relativity and quantum mechanics into relativistic quantum mechanics in 1927 [5]. This theory accommodated more facts than any before and predicted the existence of antiparticles. Indeed, the existence of positrons (anti-electrons) was established experimentally by C. D. Anderson in 1932.

Boltzmann's pioneering work on statistical mechanics was soon adapted into the framework of quantum mechanics resulting in the broad classification of all particles into "fermion"s and "boson"s. The connection between the spin angular momentum of a particle, a quantum number written as $\frac{n}{2}$ and the statistical distribution law it obeys was established by Pauli in 1940. The particles for which n is odd (fermions) were found to have categorically distinct properties compared to those for which n is even (bosons).

Dirac's work was carried further by Feynman who greatly generalized the essential ideas and re-molded relativistic quantum mechanics into his "propagator" formalism in 1949 [6]. The resulting theory, which he named "Quantum Electrodynamics", (QED) had the attractive feature of renormalizability which circumvents the annoying singularities encountered by its predecessors [7]. To date, QED gives a description of electromagnetic interactions that is more accurate than any other theory tested.

Yet, there were experimental observations which these theories of "electromagnetic interactions" didn't explain. To answer questions like "what is the source of the electron and positron emissions (nuclear β-decay) accompanied by the transmutation of the associated nuclei?" and "what holds the protons together in a nucleus against the intense electromagnetic repulsive force at such short distances?", one had to look outside the framework of QED. On

related grounds, the discovery of neutrons spurred Heisenberg to come up with the concept of "isospin" in 1932 which would prove to be much more useful in another sector 22 years later [8]. In an attempt to explain the continuous β spectrum, Pauli postulated "neutrino"s in 1930. In 1934, Fermi came up with the first explanation of the anomalously long lifetime of neutrons in free state by postulating the first version of the theory of "weak interactions" which also solved the puzzle of nuclear β-decay [9]. In 1935, Yukawa offered a radical solution to the second problem by postulating a new kind of interaction, the "strong interaction" between the protons and the neutrons in nuclei, mediated by massive particles which he called "π meson"s [10]. The π's were experimentally found in 1947 with a mass very close to that predicted by Yukawa.

However, neutrons, protons and π's turned out to be but only the lightest members of a large family of particles, called "hadron"s, that participate in strong interactions. Dozens of hadrons were found by various scattering experiments before 1964 when Gell-Mann proposed the $SU(3)$ gauge theory of strong interactions which models all hadrons as being made of "fractionally" charged, eternally "confined" "color"-ed particles that he called "quark"s [11]. Zweig also hit upon this idea independently [12].

All these breakthroughs completely rearranged our perspective of the universe within a span of about fifty years. A complete "theory of everything" was missing, but it was only a matter of time before the many components at hand were put together towards its construction. To this end, Yang and Mills formulated the concept of a "local isospin symmetry" in 1954 which was later generalized to any theory with a local non-Abelian gauge invariance [13].

In 1956, Lee and Yang suggested the possibility of "parity violation" in weak interactions [14]. Immediately, Wu and her collaborators conducted an experiment confirming within the year that parity is indeed not conserved in weak interactions [15]. In 1957 two groups: Marshak and Sudarshan and Feynman and Gell-Mann independently and simultaneously proposed the "$V-A$" nature of weak interactions [16] [17]. These progresses culminated in the formulation of the theory of "electroweak interactions". In 1961, Glashow unified the electromagnetic and weak interactions into a single framework and in 1967 Weinberg and Salam showed how the weak gauge bosons could acquire mass without spoiling the renormalizability [18][19][20]. Major experimental support for the model came from the observation of neutral currents in 1973 [21], followed by the discovery of the massive gauge bosons themselves ($W^{\pm}$ and Z) in 1983 [22][23][24][25]. Works of Gell-Mann, 't Hooft, Gross, Wilczek and Politzer resulted in the first and almost complete version of "Quantum Chromodynamics" (QCD) as a non-Abelian gauge theory of strong interactions in 1972. Together, these two theories comprised "The Standard Model" which triggered the dawn of a new era in the "quest for the tiniest".

1.2 The present state of affairs: the Standard Model (SM)

The minimal SM, as we know it today, came into being around 1973. It describes the universe as being made of matter particles which can be classified

Particle class	Particle name	Spin	Charge [1]	Mass (GeV) [2]
Quarks	down (d)	$\frac{1}{2}$	$-\frac{1}{3}$	~ 0.35 ($\sim 5.6 \times 10^{-3}$)
	up (u)	$\frac{1}{2}$	$+\frac{2}{3}$	~ 0.35 ($\sim 9.9 \times 10^{-3}$)
	strange (s)	$\frac{1}{2}$	$-\frac{1}{3}$	~ 0.55 (~ 0.20)
	charm (c)	$\frac{1}{2}$	$+\frac{2}{3}$	~ 1.6 (~ 1.35)
	bottom (b)	$\frac{1}{2}$	$-\frac{1}{3}$	~ 4.5
	top (t)	$\frac{1}{2}$	$+\frac{2}{3}$	> 131
Leptons	electron (e)	$\frac{1}{2}$	-1	5.11×10^{-4}
	e-neutrino (ν_e)	$\frac{1}{2}$	0	$< 7.3 \times 10^{-6}$
	muon (μ)	$\frac{1}{2}$	-1	0.1057
	μ-neutrino (ν_μ)	$\frac{1}{2}$	0	$< 2.7 \times 10^{-4}$
	tauon (τ)	$\frac{1}{2}$	-1	1.784
	τ-neutrino (ν_τ)	$\frac{1}{2}$	0	$< 3.5 \times 10^{-2}$
Gauge Bosons	gluons ($g_i (i = 1 \ldots 8)$)	1	0	0
	photon (γ)	1	0	0
	$W^\pm$	1	± 1	80.2
	Z	1	0	91.19
Higgs Boson	H^0	0	0	> 48

Table 1.1: The "fundamental" particles in the minimal Standard Model.

into two types of fermions: quarks and leptons. These fermions interact by the exchange of gauge bosons. The masses of all particles are attributed to their couplings with the Higgs boson(s). The world around us seems to be governed by four kinds of interactions: electromagnetic, weak, strong and gravitational. Of these, no quantum theory exists for the last one. However, the gravitational force between any two particles known is so feeble compared to the rest at the length scales of our interest that it can be safely ignored. Hence, we shall leave it out in our description of the Standard Model of particle physics. Table

1.1 summarizes the classification of the fundamental particles of the minimal SM. The six quark flavors are divided into three generations, each consisting of a doublet: (u,d), (c,s), (t,b); and similarly for the leptons: (e,ν_e), (μ,ν_μ), (τ,ν_τ). The SM can be formulated with just one generation each of quarks and leptons. The number of generations is purely an empirical observation, the SM makes no predictions about it. However, as we shall see in a moment, it does require that both the quarks and the leptons appear in doublets and that's why the t quark is needed to complete the doublet of which one member, the b, has been discovered.

To take part in electromagnetic interactions (mediated by photons) a particle has to have electric charge. Photons couple with all fermions except the neutrinos. All particles except gluons partake in weak interactions. Strong interactions (mediated by gluons) are limited between particles with "color" charge which is unique to the quarks and the gluons. The electromagnetic and the weak interactions have been unified into the electroweak model. The strong interactions described by QCD forms a disjoint sector. After a quick glance at the underlying principle common to both, we will briefly review the two separately and say a few words about the Higgs sector.

---

[1] $e \equiv -1$

[2] Given as constituent (current) mass if the two are different. The current or "running" masses are evaluated at 1 GeV.

1.2.1 Gauge theories in particle physics

According to Noether's theorem, for a system described by a Lagrangian, any continuous symmetry that leaves the action invariant leads to the existence of a conserved current. In gauge theories of quantum fields, for each such symmetry, one performs a phase transformation of the wave function of a particle (the fermion field) and subtracts a term for the associated potential (the gauge boson field) from the canonical momentum (∂_μ) of the particle in order to obtain its kinetic momentum ($\mathcal{D}_\mu$) relevant to the Lagrangian [26][27][28]:

$$\psi_0(x) \rightarrow \psi(x) = \psi_0(x) e^{ig_j \alpha_j(x) T_j} \tag{1.1}$$

$$\partial_\mu \rightarrow \mathcal{D}_\mu = \partial_\mu - i g_j T_j^k R_{j\mu}^k \tag{1.2}$$

where for the j-th symmetry ($j = 1 \ldots n$), $R_{j\mu}^k$ are the potentials, T_j^k are the generators of the symmetry group obeying the appropriate Lie algebra, g_j is the (arbitrary) strength of the coupling and $\alpha_j(x)$ is an arbitrary function of space-time. Summation over the repeated indices is implied. Each conserved current corresponds to an intermediate gauge boson.

1.2.2 The Electroweak Model

The electroweak model is a gauge theory based on the broken symmetry group $U(1) \times SU(2)_L$. The fermions are introduced in "left-handed" doublets and "right-handed" singlets in the $SU(2)$ part where "handedness" refers to the helicity of the fermion i.e. the component of its spin along its direction

of motion (right (left) handed $\Rightarrow \vec{\sigma}\cdot\hat{p} = +1(-1)$) helicity): $\psi_{iL} = \begin{pmatrix} \nu_i \\ l_i^- \end{pmatrix}_L$ and $\begin{pmatrix} u_i \\ d_i' \end{pmatrix}_L$; $\psi_{iR} = l_{iR}^-, u_{iR}, d_{iR}'$, where $d_i' \equiv V_{ij}d_j$, and V is the Cabbibo-Kobayashi-Maskawa (CKM) quark mixing matrix [29]. Generation-mixing via charged currents (CC) is greatly suppressed for leptons i.e. the off-diagonal elements of the 3×3 matrix of CC amplitudes connecting the heavier leptons to the neutrinos are very small (perhaps zero). The CKM matrix has four parameters, namely three mixing angles and one observable phase angle, whose values are not predicted by the SM. The phase angle implies CP-violating interactions (CP $\equiv$ Charge·Parity quantum number). Experimental observation of CP-violation is needed as a vital validation of the electroweak model.

The generator of the $U(1)$ symmetry is called "hypercharge" (Y) and that of the $SU(2)_L$ is called "weak isospin" $(\vec{T} \equiv \frac{\vec{\tau}}{2})$. The fermion kinetic momentum for the electroweak interaction is then given by

$$\mathcal{D}_\mu = \partial_\mu - ig_1 Y B_\mu - ig_2 \frac{\tau^i}{2} W_\mu^i \tag{1.3}$$

where τ_i $(i = 1,2,3)$ are the Pauli spin matrices for the left-handed fermions and identically 0 for the right-handed ones. The corresponding Lagrangian for the unbroken $SU(2)_L \times U(1)_Y$ symmetry is

$$\mathcal{L} = \bar{\psi} i\gamma^\mu \mathcal{D}_\mu \psi - \frac{1}{4} B^{\mu\nu} B_{\mu\nu} - \frac{1}{4} W_i^{\mu\nu} W_{\mu\nu}^i \tag{1.4}$$

with a separate term for each fermion field ψ_L and ψ_R in the 4-component Dirac spinor notation. The fermion-independent terms in $\mathcal{L}$ are required by the non-Abelian nature of the symmetry and give rise to cubic and quartic

self-couplings of the boson fields. The gauge field tensors are defined as

$$B_{\mu\nu} \equiv \partial_\mu B_\nu - \partial_\nu B_\mu \tag{1.5}$$

and

$$W^i_{\mu\nu} \equiv \partial_\mu W^i_\nu - \partial_\nu W^i_\mu - g_2 \varepsilon_{ijk} W^j_\mu W^k_\nu \tag{1.6}$$

The mechanism of mass-generation via spontaneous symmetry breaking (SSB) is under the jurisdiction of the Higgs sector at which we shall take a passing look in the next section. Here we only note that the four mass eigenstates γ, W^+, W^- and Z are orthogonal linear combinations of B_μ, W^i_μ:

$$\begin{pmatrix} W^+_\mu \\ W^-_\mu \\ Z_\mu \\ A_\mu \end{pmatrix} = \begin{pmatrix} \frac{1}{\sqrt{2}} & -\frac{i}{\sqrt{2}} & 0 & 0 \\ \frac{1}{\sqrt{2}} & +\frac{i}{\sqrt{2}} & 0 & 0 \\ 0 & 0 & \cos\theta_W & \sin\theta_W \\ 0 & 0 & -\sin\theta_W & \cos\theta_W \end{pmatrix} \begin{pmatrix} W^1_\mu \\ W^2_\mu \\ W^3_\mu \\ B_\mu \end{pmatrix} \tag{1.7}$$

while W^+_μ, W^-_μ and Z_μ represent the three weak boson fields, A_μ is the electromagnetic potential associated with the photon (γ). θ_W, known as the "weak mixing angle" (or "Weinberg angle"), is a parameter of the gauge sector and

$$\sin^2\theta_W \equiv \frac{g_1^2}{g_1^2 + g_2^2} \tag{1.8}$$

has been measured experimentally to be 0.232 [30]. As a result of the construction, the right-handed fermions do not interact with $W^\pm$.

The hypercharge and weak isospin quantum numbers of the first generation leptons and fermions are listed in Table 1.2. The electric charge of a fermion (Q) is actually a linear combination of these two quantum numbers.

$$Q = T_3 + Y \tag{1.9}$$

Particle	T	T_3	Y	Q
ν_e	$\frac{1}{2}$	$\frac{1}{2}$	$-\frac{1}{2}$	0
e_L^-	$\frac{1}{2}$	$-\frac{1}{2}$	$-\frac{1}{2}$	-1
e_R^-	0	0	-1	-1
u_L	$\frac{1}{2}$	$\frac{1}{2}$	$\frac{1}{6}$	$\frac{2}{3}$
d'_L	$\frac{1}{2}$	$-\frac{1}{2}$	$\frac{1}{6}$	$-\frac{1}{3}$
u_R	0	0	$\frac{2}{3}$	$\frac{2}{3}$
d'_R	0	0	$-\frac{1}{3}$	$-\frac{1}{3}$

Table 1.2: Weak isospin and hypercharge quantum numbers of the first generation of leptons and quarks.

The absence of right-handed neutrinos in the picture causes no breakdown so long as the neutrino masses are zero because then the helicity of a neutrino is frame-independent (helicity is a conserved quantity in a given frame of reference). Since a right-handed neutrino has no coupling with any gauge boson, its existence would have no bearing on the SM. Although the question of neutrino mass is an open one at this time, this picture is consistent with the fact that no evidence of a right-handed neutrino has yet been found.

At its inception, QCD had only three quarks: u, d and s. This caused problems in the electroweak sector as the predicted existence of flavor-changing neutral currents (FCNC) was flatly contradicted by experiments. In a groundbreaking development, Glashow, Iliopoulos and Maiani (GIM) proposed a solution [31] that eliminated the need for FCNC by bringing in an additional quark flavor, the c quark, whose existence was experimentally confirmed in

1974. In 1976, the b quark was found and an extension of the GIM mechanism, in order to accommodate a third generation of quarks, now requires the existence of an $SU(2)_L$ partner for it.

The electroweak potential has the following spatial dependence:

$$V(r) = \frac{e^{-Mr}}{r} \tag{1.10}$$

where M is the mass of the intermediate gauge boson. The extremely short range of the weak interactions is explained by the high masses of their mediators which results in a sharp cut-off beyond the Fermi distance: $r \sim 10^{-24}$ m. The fact that the weak interactions are so much weaker than the electromagnetic also has its explanation in the high masses of the weak bosons which are less likely to be produced when the mass of the virtual boson propagator exchanged in an interaction is closer to M_γ (=0) than to M_W or M_Z, which is the case at low energies.

1.2.3 The Higgs sector

In our discussions so far, we have sidestepped the question of the masses of the particles. The unbroken $U(1)_Y \times SU(2)_L$ symmetry is valid for massless fermions and gauge bosons, but it turns out that many of these particles are attributed with non-zero masses. Experimental confirmation pending, the Higgs mechanism provides a meaningful gauge theory which can accommodate such a scenario where the particles have mass [32][33]. In essence, the assumption is made that the universe is filled with a spin-0 field, called a "Higgs" field (H), that is a doublet in the $SU(2)$ space of isospin and carries non-zero

$U(1)$ hypercharge, but is a singlet in the $SU(3)$ color space. This is meant in much the same sense that the vacuum is filled with electromagnetic fields whose sources are electrically charged particles (however, we shall not seek the sources of H here). The gauge bosons and the fermions can interact with H and in its presence they no longer appear to have zero mass. A crucial ingredient is that states with one or more H are not orthogonal to the ground state (i.e. the vacuum) even though these states carry non-zero T and Y quantum numbers. This means that these quantum numbers of the vacuum are non-zero, so the $SU(2)_L$ and $U(1)$ symmetries are effectively broken. When a symmetry is broken in this way, i.e. the symmetry is valid for the Lagrangian but not for the ground state of the system, it is said to be a spontaneously broken symmetry.

In the minimal electroweak model there is a single complex Higgs field that transforms as a doublet under the $SU(2)$ of isospin: $\phi \equiv \begin{pmatrix} \phi^+ \\ \phi^0 \end{pmatrix}$

After SSB, the fermionic part of the Lagrangian can be expressed as

$$\begin{aligned} \mathcal{L}_F &= \bar{\psi}_i(i\gamma^\mu\partial_\mu - M_i)\psi_i \\ &\quad -eq_i\bar{\psi}_i\gamma^\mu\psi_i A_\mu \\ &\quad -\frac{g}{2\sqrt{2}}\bar{\psi}_i\gamma^\mu(1-\gamma^5)(T^+W_\mu^+ + T^-W_\mu^-)\psi_i \\ &\quad -\frac{g}{2\cos\theta_W}\bar{\psi}_i\gamma^\mu(V-A)\psi_i Z_\mu \\ &\quad -\bar{\psi}_i\frac{g_2 m_i H}{2M_W}\psi_i \end{aligned} \tag{1.11}$$

where $e = g_2 \sin\theta_W$ is the positron electric charge, M_i and q_i are the mass and electric charge (in units of e) of the fermions respectively, T^+ and T^- are the

weak isospin raising and lowering operators:

$$T^{\pm} \equiv \frac{1}{\sqrt{2}}(T_1 \pm iT_2) \tag{1.12}$$

The vector and axial couplings are

$$\begin{aligned} V &\equiv T_3 - 2q\sin^2\theta_W \\ A &\equiv T_3\gamma^5 \end{aligned} \tag{1.13}$$

H is the physical neutral Higgs scalar which is the only remaining part of ϕ after SSB. The first term in $\mathcal{L}_F$ gives the Dirac equation for a free fermion, the second corresponds to its electromagnetic interaction, the third and the fourth terms correspond to the charged and neutral weak current interactions respectively and the last term accounts for the Higgs interaction (it shows that the Yukawa coupling of H to ψ_i is flavor-diagonal in the minimal model). The full Lagrangian contains additional terms for the interactions between the Higgs and the weak fields as well as their self-interactions.

Despite objections made on aesthetic grounds, the Higgs mechanism serves as an excellent working hypothesis providing the simplest known scheme to generate masses for the W and Z as well as for the quarks and the leptons. Search for the Higgs boson(s) is one of the major challenges to experimental particle physics today. While there is no water-tight limit from theory, there is a general consensus is that the mass of the Higgs (M_H) is most likely to be below 1 TeV. The strength of the coupling between the Higgs and a particle increases with the latter's mass. So, if the mass of the Higgs is higher than some threshold, new physics will be needed to accommodate its self-coupling.

Indirect constraints on the lower limit come from the fact that for a given mass of the top quark, if the Higgs' mass were below a certain value, its coupling with virtual top quarks would disrupt the stability of the vacuum.

1.2.4 Quantum Chromodynamics (QCD)

Strong interactions are described by a local non-Abelian (Yang-Mills) gauge theory of quarks and gluons in which $SU(3)$ is the gauge group and gluons are the gauge bosons. In each flavor, a quark has three available "color" states (Red (R), Green (G) and Blue (B)) to form a triplet in the fundamental representation of $SU(3)_C$ while eight gluons form an octet in the adjoint representation (defined to have the same dimensions as the group). The covariant derivative acting on a quark field is

$$\mathcal{D}_{\mu,jk} = \delta_{jk}\partial_\mu - ig_3\lambda^a_{jk}G^a_\mu \tag{1.14}$$

resulting in the Lagrangian

$$\mathcal{L} = \bar{\psi}_j(i\gamma^\mu\mathcal{D}_{\mu,jk} - M_j\delta_{jk})\psi_k - \frac{1}{4}F^{\mu\nu}_a F_{a\mu\nu} \tag{1.15}$$

where the indices a, j and k refer to color and assume the values $a = 1, \ldots, 8$ and j, k = 1,2,3. ψ_j are the 4-component Dirac spinors representing the quark fields, G^μ_a are the gluon fields, λ_a are the generators of the $SU(3)_C$ symmetry group, g_3 is the strong coupling coefficient and M_j is the quark mass. In analogy with equations (1.4) and (1.5), the gluon field tensor is defined as

$$F^{\mu\nu}_a \equiv \partial^\mu G^\nu_a - \partial^\nu G^\mu_a - g_3 f_{abc} G^\mu_b G^\nu_c \tag{1.16}$$

where f_{abc} are the structure constants of $SU(3)$.

The strong interaction potential between two quarks takes the form

$$V(r) \propto \frac{\alpha_s(r)}{r} \tag{1.17}$$

The dependence of α_s on r is such that we have $V(r) = \lambda r$ as $r \to \infty$. Due to the self-coupling of the gluons, the lines of color force attain a constant flux at large separations. As a result, when more and more energy is injected into a $q\bar{q}$ bound state, a phenomenon analogous to "ionization" in electromagnetic bound states never takes place. Instead, new $q\bar{q}$ states keep popping up from the vacuum. This explains "confinement", the reason why single quarks and gluons can never be isolated: they can only be found in colorless composite states. It also suggests that at very small separations, the quarks should behave essentially as "free" particles as far as strong interactions are concerned ("asymptotic freedom").

1.2.5 The missing pieces

The current Standard Model of particle physics is a partially unified gauge theory of quantum fields for the electromagnetic and weak interactions which, together with QCD, the theory of strong interaction, exhibits a broken $U(1)_Y \times SU(2)_L \times SU(3)_C$ symmetry. It seems to give a fairly satisfactory account of the interactions of the "fundamental" particles, which are the quarks and the leptons. Their gravitational interactions appear to be entirely in accord with classical general relativity, but so far no consistent quantized version of this theory has been formulated. The standard model is satisfactory in

the sense that it accommodates all the observed phenomena and all of its predictions checked so far have been very accurate. On the other hand, it has several "ugly" features. Most undesirable of these is the presence of so many parameters (seventeen, to be exact: nine fermion masses, three coupling coefficients, four angles of the CKM matrix and the mass of the Higgs boson) for whose values it has no explanation: they seem to be completely arbitrary in its context. The left-right asymmetry of the electroweak sector is aesthetically unpleasant and can be cured by including some extra massive gauge bosons in an extension of the model without any concurrent anomalies. There are also questions of quantum gravity and, ultimately, a grand unified theory (GUT) for all the known interactions. While there are theoretical grounds to believe that a more elegant and more powerful model, free of the above-mentioned blemishes, must exist, the SM in its present form remains a strong candidate for one that is at least asymptotically valid. The fact that the fraction of the SM that overlaps with verifiable reality is larger than any other around also makes it the most relevant at this time.

Of the electroweak theory and QCD, the latter is the tougher beast to tame. The perturbative methods that work such miracles for QED, do not do so well in QCD, the coupling coefficient in the latter being much stronger at the shortest distances we can probe today. Consequently, QCD cannot make predictions with the precision of QED. The saving grace is that its large uncertainties accommodate all the experimental observations more or less satisfactorily and it does not predict much beyond what we see. However, some crucial predictions of the more precise electroweak sector of SM remain

unverified, viz.

- The top quark has not been found yet.
- The Higgs boson remains to be discovered.
- The triple and quartic couplings of the gauge bosons needed to establish the non-Abelian nature of the theory need better understanding.
- CP violation predicted by the model awaits an experimental verdict.
- Our knowledge of the neutrino sector is rather poor.

It is therefore natural to seek to resolve these issues, among which the discovery of the top quark is expected to be most imminent (the remaining tests of the electroweak model will probably take some time). It is towards this goal that the efforts of this thesis are aimed.

1.3 The *top* quark in the Standard Model

In this section we will discuss briefly the grounds of theoretical expectations and indirect experimental evidences for the existence of the t quark, the mechanisms of its production and decay, the decay channel pursued in this thesis and finally, the relevance of the search for top quark which motivates our work. All of our arguments will be based on the framework of the minimal SM.

1.3.1 Why t?

Ever since the discovery of the b quark, physicists have been looking for another one, the t quark, to form an $SU(2)_L$ doublet with it. If the b quark does not have a partner, it must be an $SU(2)_L$ singlet. As one would expect, whether the b quark is in a singlet or a doublet has serious implications on its couplings with the weak bosons. Over the past 10 years or so, after the discovery of the weak bosons and with the advent of high-energy, high-luminosity colliders where b quarks and weak bosons are produced in abundance, we have learnt a great deal about the properties of the b quark from precision measurements.

First, consider the reaction $e^+e^- \rightarrow (\gamma, Z) \rightarrow b\bar{b}$. The contribution from the γ's to the angular distribution of the b's about the plane perpendicular to the beamline in the CM frame is always symmetric but that from the Z's should be asymmetric if the b quark is an $SU(2)_L$ doublet. The forward-backward asymmetry is defined as

$$A_{FB}^b \equiv \frac{\sigma_F^b - \sigma_B^b}{\sigma_F^b + \sigma_B^b} \tag{1.18}$$

where σ_F^b and σ_B^b are the cross-sections of b jets in the forward and backward directions respectively. If the Z is real, A_{FB}^b is proportional to $T_{3L}^b - T_{3R}^b$. Thus, if b is an $SU(2)_L$ singlet, then $T_{3L}^b = T_{3R}^b$ and, consequently, $A_{FB}^b = 0$ at the Z pole. The current measured value $A_{FB}^b = 0.107 \pm 0.013$ from LEP contradicts such a scenario but agrees, within errors, with the SM prediction otherwise [34]. In fact, T_{3L}^b and T_{3R}^b can be calculated from another measured

quantity, $\Gamma(Z \to b\bar{b})$, which is also a function of either:

$$\Gamma(Z \to b\bar{b}) \propto (T_{3L}^b + \frac{1}{3}\sin^2\theta_W)^2 + (T_{3R}^b + \frac{1}{3}\sin^2\theta_W)^2 \qquad (1.19)$$

The constant of proportionality has been calculated to good accuracy. A calculation using the measured values of A_{FB}^b and $\Gamma(Z \to b\bar{b})$ yields $T_{3L}^b = -0.504^{+0.018}_{-0.011}$, $T_{3R}^b = -0.008^{+0.056}_{-0.056}$ which suggests very strongly that the b quark has a $SU(2)_L$ doublet partner, namely the t quark [35].

Second, if the b quark is an $SU(2)_L$ singlet, it cannot decay via charged current. Then, the fact that it does decay requires the existence of FCNC. FCNC is suppressed for doublet quarks by the GIM mechanism which requires all left- and right-handed components of the same charge in the different quark generations to have the same weak isospin. Without this suppression, FCNC should be observed in the B mesons several orders of magnitude above the experimental upper limit [35].

Third, there are purely theoretical arguments in favor of the existence of top. These include the cancellation of anomalies which arise if the sum of the absolute electric charges within a fermion generation is not unity and the explanation of the observed rate of $B^0 - \bar{B}^0$ mixing which has contributions from virtual t quarks in the loop diagrams. However, it is not yet clear whether the anomalies would have an observable effect or whether the $B^0 - \bar{B}^0$ mixing can have an alternative explanation. Yet, in a nutshell, since the topline is "there is a bottom", the bottomline is "there must be a top".

The first question, then, is,"what is the mass of the top quark (M_t)?" To our advantage, M_t affects the cross-sections of other processes through radia-

tive corrections (all the more reason for us to be interested in it). For example, the mass and width of W as well as those of Z depend on M_t, but in somewhat different ways. Taking the ratios such as $\frac{M_W}{M_Z}$ and $\frac{\Gamma(W)}{\Gamma(Z)}$ many systematic uncertainties can be cancelled. Precision measurements of these and several other quantities impose constraints on M_t. Unfortunately, the unknown mass of the Higgs boson (M_H) also affects these calculations. A recent combined fit to several of these quantities measured at LEP and elsewhere (CDF, UA2, CDHS, CHARM, CCFR) results in the following prediction [36]:

$$M_t = 178 \pm 11^{+18}_{-19} \text{ GeV} \tag{1.20}$$

The central value and the first set of errors correspond to M_H fixed at 300 GeV while the second set of errors are obtained by letting M_H vary between 60 GeV and 1000 GeV. Physics beyond the SM will be required to account for the experimental results should the top quark not be found within this predicted mass window.

The experimental lower limit on M_t based on the assumptions of SM prior to the recent publication from DØ came from CDF [37]:

$$M_t > 91 \text{ GeV} \quad (95\%\text{C.L.}) \tag{1.21}$$

A previous analysis of the data collected by the DØ experiment resulted in the most recent lower limit on M_t [38]:

$$M_t > 131 \text{ GeV} \quad (95\%\text{C.L.}) \tag{1.22}$$

More recently, the CDF collaboration has published its results on the same subject. They see what they call an "evidence", barely shy of a "proof" for

the existence of the t quark. Analysis of their candidate events results in an estimate for M_t [39]:

$$M_t = 174 \pm 10^{+13}_{-12} \text{ GeV} \tag{1.23}$$

The production cross-section, using this mass to compute the acceptance, is measured to be

$$\sigma(t\bar{t}) = 13.9^{+6.1}_{-4.8} \text{ pb} \tag{1.24}$$

There are also (almost) model-independent ways of setting such limits. For example, the mass-region below $\frac{M_Z}{2}$ can be probed for the existence for t looking at the production of quark pairs in e^+e^- collisions. Measurements of the partial widths of W decay is a little more difficult, but allows exploration of higher mass regions since a W can decay to a real t and a b if $M_t < M_W - M_b$. Although these methods are based on SM couplings, they do not depend on the details of the decay of the top quark. Currently, the highest model-independent lower limit comes from the CDF collaboration: $M_t > 62$ GeV [40].

1.3.2 Production and decay of the top quark

For $M_t > M_W$, top quarks are expected to be produced dominantly in pairs via strong interactions at the Tevatron. In this thesis, we will concentrate only on the production of top in pairs which has a much larger cross section than that of the production of a single top and is also a whole lot easier to look for. in the mass range of current interest ($M_t > 91$ GeV). The leading order QCD diagrams are shown in Figure 1.1. Figure 1.2 shows that as M_t increases, $q\bar{q}$ annihilation dominates the production since the valence quarks

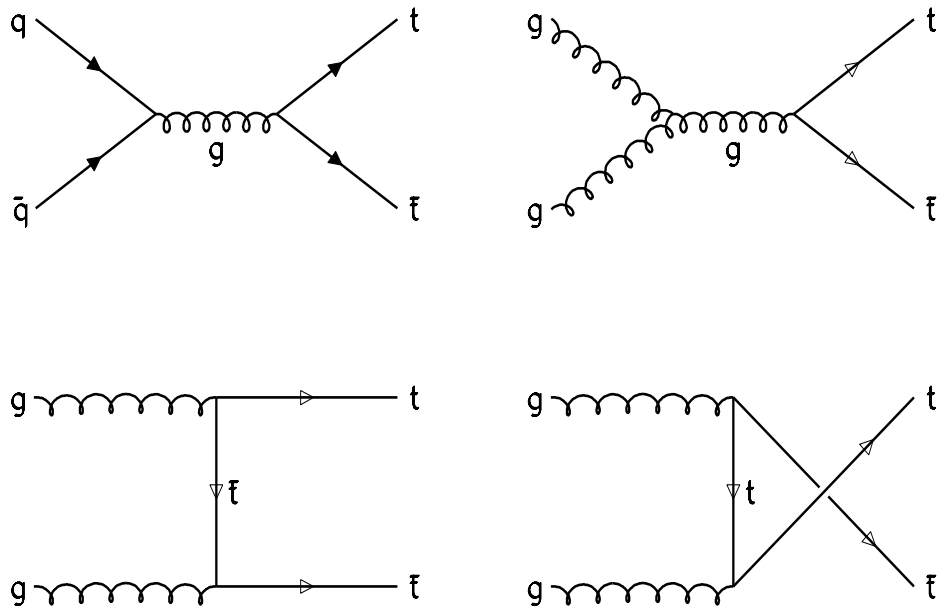

Figure 1.1: The leading order Feynman diagrams for QCD production of $t\bar{t}$.

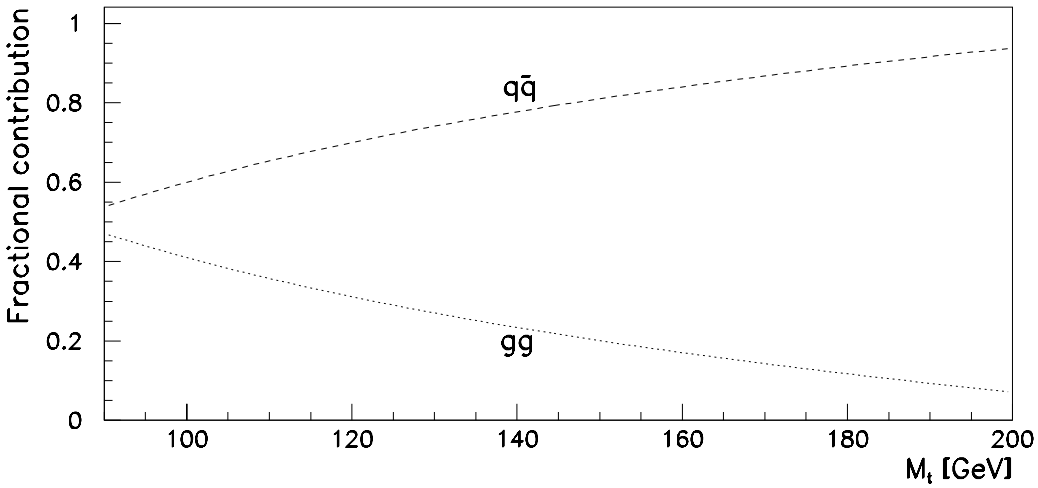

Figure 1.2: Fractional contributions of $q\bar{q}$ and gg processes (NLO) to the production of $t\bar{t}$ at the Tevatron.

are then more likely than gluons to have sufficient momenta to produce it. In collisions at much higher energies, for example, at the LHC ($\sqrt{s}$ = 16 TeV), gg processes will by far dominate if M_t is anywhere near where it is currently expected to be. The theoretical cross-section for the production of $t\bar{t}$ at the Tevatron has been calculated as a function of M_t taking into account exactly up to next-to-leading order (NLO) QCD processes and extending it to higher orders by applying the technique of soft-gluon resummation [41]. We shall use these cross sections, plotted in Figure 1.3, for comparison at the end of our analysis. The solid line shows the central value, the dotted lines represent the uncertainties.

Due to its large mass, the t quark has a wide phase space available for its decay which makes it extremely short-lived (lifetime $\sim 7 \times 10^{-24}$ sec for M_t = 100 GeV). According to the CKM matrix, the weak decay branching ratio (BR) of a t quark into a b quark and a real W boson exceeds 0.998 if $M_t > M_W + M_b$ [42] (decays such as $t \rightarrow bH^+$ etc. are beyond the scope of the minimal SM and will not be explored here). So, almost exclusively, we have two W's and two b's from the decay of the two t's. Each W can decay either leptonically : BR($W \rightarrow l\nu_l$) = $\frac{1}{3}$ where l represents a lepton from any generation ($e/\mu/\tau$), or hadronically: BR($W \rightarrow q_1\bar{q}_2$) = $\frac{2}{3}$ where q_1, q_2 are quarks from the first two generations (u, d, c, s). Due to the lepton universality of real weak currents, the leptonic BR of the W is divided equally between the three lepton generations.

Thus, at the first partonic level after the W decay, we have six partons. The distribution of these partons in the phase space depends primarily on

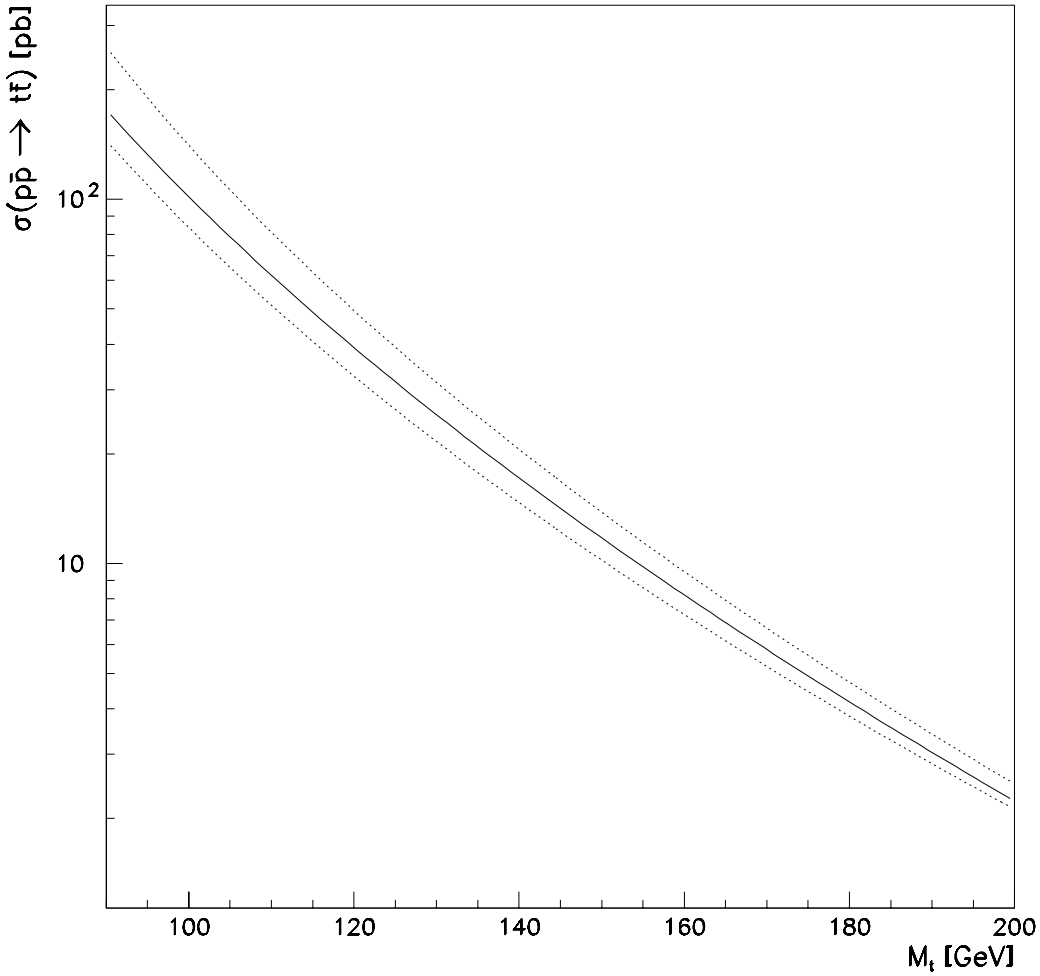

Figure 1.3: Cross-section of the process $p\bar{p} \rightarrow t\bar{t}$ at the Tevatron (NLO + soft-gluon resummation).

two related factors: the transverse momentum of the top ($p_T(t)$) and M_t. For $M_t < 220$ GeV, $p_T(t)$ is expected to peak around $\frac{M_t}{2}$ at the Tevatron with most of the spectrum between $\frac{M_t}{3}$ and M_t. For us, this is very favorable since the lower edge is high enough to give the final-state partons sufficient p_T for detection and the higher edge is low enough for their isolation. Note that the situation could be very different at $\sqrt{s} = 40$ TeV where $p_T(t)$ would be so high compared to M_t (assuming, once again, $M_t < 220$ GeV) that the $t\bar{t}$ system would appear essentially as two back-to-back jets in the detector, making it difficult to separate the decay products of a t that decays into $q_1\bar{q}_2 b$. At the other extreme, if the $p_T(t)$ spectrum peaked very sharply at zero and if, further, ΔM ($\equiv M_t - M_W - M_b$) were to be very small, the b's would be so soft that we would often be unable find it as a single hadronic jet in our detector. Fortunately for us, distributions of the absolute and relative p_T's of the six partons all peak more or less between $\frac{M_W}{4}$ and M_W in the range of M_t under current scrutiny. This leaves the partons nicely separated in the configuration space yet beefy enough for efficient detection.

The dileptonic decay channel (where both W's decay leptonically) has the least backgrounds of all, but unfortunately it also has the smallest BR. The non-leptonic channel (where both W's decay hadronically) has the lion's share of the total decay width but it also has a huge background from QCD multijet processes that do not have any real t quarks in them. The monoleptonic channel (where precisely one of the two W's decays leptonically) is somewhere in-between with regards to both BR and backgrounds.

1.3.3 Search for $t\bar{t}$ in the electron + $\not\!\!E_T$ + jets final state

In this thesis, we go after a subchannel of the monoleptonic decays searching for $t\bar{t}$ in the final state where one of the t's has decayed into $e\nu_e b$ and the other into $q_1 q_2 b$ as shown in Figure 1.4. S represents the hard-scattering process and X represents anything else that may have been produced in addition to the $t\bar{t}$ system. Straightforward arithmetic from the BR's given above yields:

$$\mathrm{BR}(t\bar{t} \to e\nu_e q_1 \bar{q}_2 b\bar{b}) = \frac{4}{27} \approx 0.15 \tag{1.25}$$

In our detector, each of the 4 quarks is expected to show up as a hadronic jet, the electron as an electromagnetic cluster with an associated track found in the central tracking volume and the neutrino through the $\not\!\!E_T$ that would put the net transverse momentum of the event to zero.

The background has two major components. The first one is the physical background arising from the continuum production of $W + jets$ (as opposed to production of $W + jets$ through resonances as in our signal). For the leptonic signatures coming from a genuine W which, furthermore, has a p_T spectrum that happens not to be too unlike that expected from the signal, we only have the jet kinematics, event topologies and heavy-flavor contents of the jet for discriminants. Fortunately, this background can be brought down to a level below the signal without suffering a debilitating slashing of the efficiency. The second background is attributed to imperfect instrumentation which will occasionally allow multijet events not containing a real W to mimic

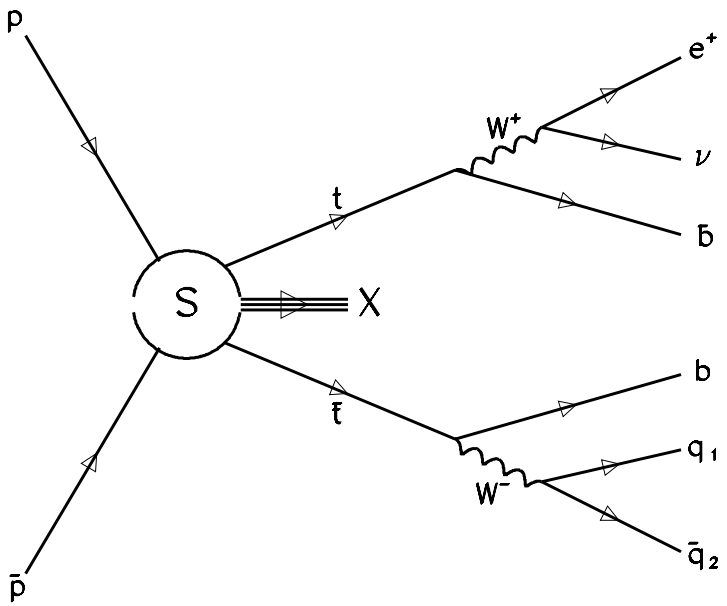

Figure 1.4: The Feynman diagram for the partonic decay sequence of $t\bar{t}$ produced in a $p\bar{p}$ collision into a final state containing an electron, a neutrino and four quarks.

the signature of our signal by statistical fluctuations in measurement. Here, in addition to the jets, the electron and the $\not\!\!E_T$ can be used to reduce the contributions well below the physics background.

Since the backgrounds have a smaller fraction of b quarks, if one can identify the b-jets, an excessive fraction of the candidate events in any channel containing b-jets would be a strong hint for signal. At DØ , the only way to accomplish this, at present, is using muon tags ($b \to \mu$, $b \to c \to \mu$). The probability of finding a prompt muon in the decay products of a b quark is approximately 0.22 [43]. For $p_T(b) \gg M_b$, such a muon is expected to be buried in the b jet. Such non-isolated muons (as opposed to prompt leptons from W decay which are isolated) can thus be used to tag b jets. Although we do not specifically look for such tags in our analysis, after we are done, we examine the candidate events to see if there is any. No conclusion is drawn from the observation.

1.3.4 What do we do once the top quark is found?

First and foremost, the discovery of the t quark will be a major victory for the Standard Model. Next, it will pave the way for many a new advance in particle physics. The first thing to do after its discovery will be to determine its mass. Until the turn of the century, Tevatron will be the only place to produce and study top quarks if $M_t < 250$ GeV. The accuracy of the measurement of M_t will increase with the amount of available data and it will be a check for the theoretical prediction (equation 1.20). Studies of the kinematics and the

cross-section of the production and decay of the $t\bar{t}$ system will also calibrate the theory, particularly in the QCD sector, at a new energy scale. A good knowledge of M_t will reduce the uncertainties in the theoretical calculations which are sensitive to it (mostly due to loop corrections). One of the most important is that it will tighten the constraints on M_H. The Higgs boson should couple more strongly with t than with other particles owing to the the higher mass of t. Discovery of t will thus improve our understanding in the Higgs sector which in turn could help us understand the mechanism of mass-generation. It will also lead to searches for possible resonances (e.g. $H \rightarrow t\bar{t}$) or bound states (e.g. $\eta_T \rightarrow t\bar{t}$ or $v_8 \rightarrow t\bar{t}$) involving t quarks [44].

Chapter 2

The collider: Tevatron

Tevatron is the machine at Fermilab that provides the collisions we study. It collides protons with antiprotons at a center-of-mass energy ($\sqrt{s}$) of 1.8 TeV [45],[46]. At present, it is the highest center-of-mass energy available anywhere in the world. In this chapter, we shall present a sketchy overview of the principles of operation of the Tevatron in the collider mode.

The collider at Fermilab, shown in Figure 2.1, is a sophisticated device consisting of seven major components: (1) A Cockroft-Walton accelerator (the Pre-accelerator), (2) A linear accelerator (the Linac), (3) The Booster synchrotron, (4) The Main Ring synchrotron, (5) The Antiproton Source, (6) The Antiproton Debuncher, and (7) The Tevatron Ring.

First, H^- ions are created in an "ion source" by passing Hydrogen gas over a catalytic surface in the presence of free electrons. These ions are released into the pre-accelerator which produces a static electric field to propel the ions to 750 KeV. The ions are then injected into the 150 meter long Linac. This device induces an oscillating electric field between a series of electrodes

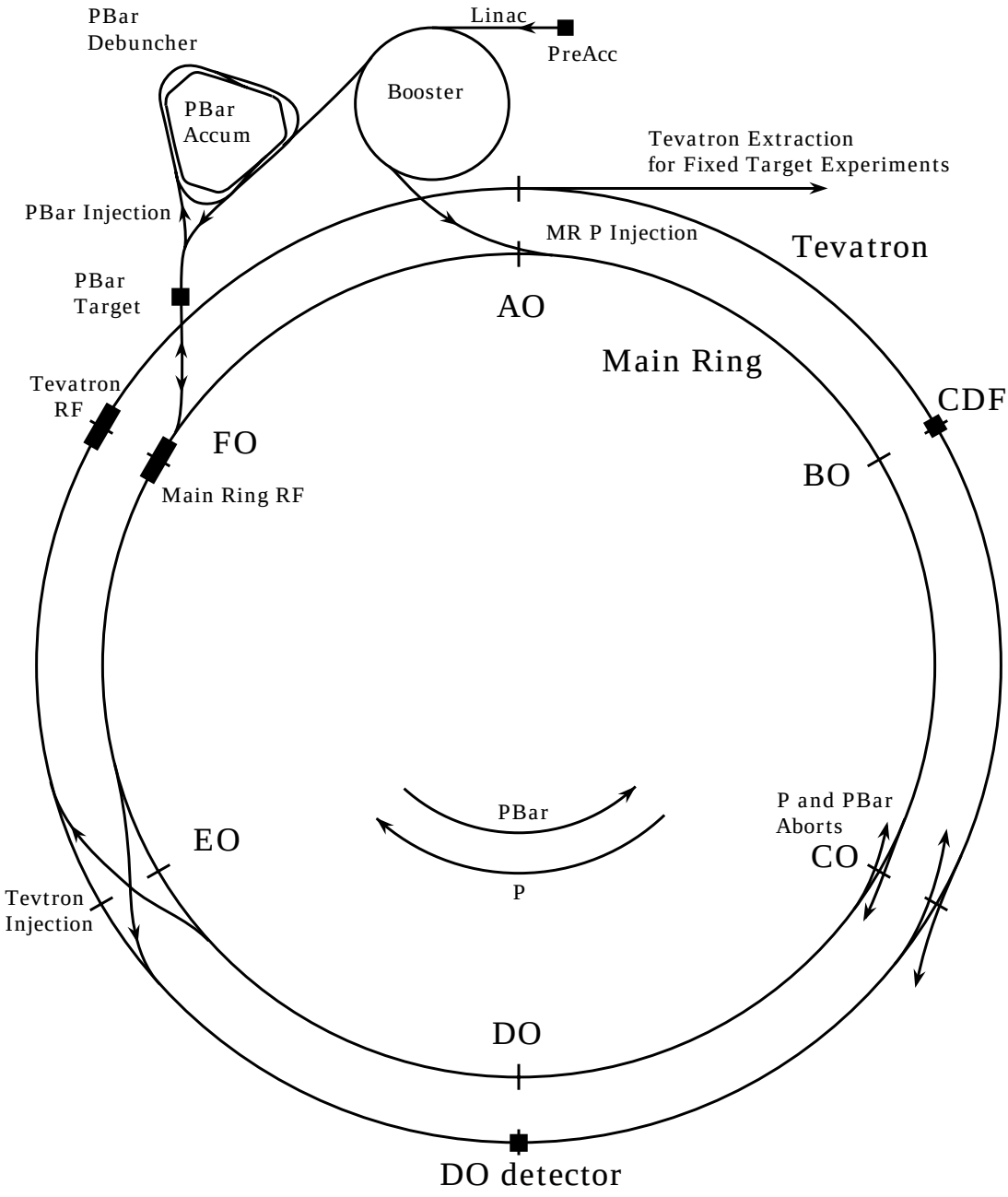

Figure 2.1: The Tevatron at Fermilab (collider mode)

which accelerates the ions to 200 MeV. The H^- ions are then sent through a carbon foil which strips both the electrons off each ion. What come out of the carbon foil are protons (H^+ ions). The protons are steered into the Booster synchrotron ring (500 meters in circumference). A synchrotron is a cyclic accelerator in which the particles are confined to a closed orbit by a series of bending magnets. Quadrupole focusing fields keep the beam from diverging. On each pass around the ring, the particle's energy is increased by acceleration in a set of synchronized Radio Frequency (RF) cavities. As the momentum increases, the magnetic field in the bending magnets must be increased to keep the particles in the ring:

$$p = qBr \tag{2.1}$$

where p is the particle momentum, q its charge, B the magnetic field and r the radius of curvature. Hence, the maximum particle energy is limited by the strength of the magnetic field and the radius of the ring. Protons exiting the Booster have an energy of 8 GeV. These protons are injected into the Main Ring (MR) which is a synchrotron consisting of more than 1,000 conventional copper-coiled magnets in a ring 6 Km in circumference. The MR accelerates the protons and coalesces them into shorter bunches. When the protons have attained 120 GeV, the bunches are extracted and directed onto a nickel/copper target creating about 2×10^7 antiprotons per bunch. For every 10^6 protons which strike the target, only about 20 antiprotons make it to the next step. A cylinder of liquid lithium creates a focusing magnetic field from a pulsed current of 600,000 amperes. This acts as a lens which keeps the antiproton

beam from diverging. Following this treatment, the antiprotons are injected into the first of two antiproton storage rings.

This first ring is known as the "Debuncher" which uses sophisticated RF techniques to "squeeze" the antiproton beam further into as compact a phase space as possible. This process is known as "cooling". The Debuncher uses two cooling processes. The first, called "debunching", was invented at Fermilab. As a bunch of antiprotons circulates around the ring, computer controlled RF manipulations reduce fluctuations in the longitudinal component of the antiproton momenta. The second process, known as "stochastic cooling", restricts the transverse oscillations of the antiproton beam. Fluctuations in the circulating current are detected by sensors which send correction signals to "kicker" electrodes that, on the average, adjust the path of the wayward particle. When the process is complete, the antiprotons form a ring that looks almost static in a rotating frame of reference. The "cooled" antiprotons are transferred into the antiproton storage ring known as the "Accumulator" 2×10^{10} at a time. The Debuncher and the Accumulator are in the same tunnel which is 520 meters in circumference. Several different systems within the Accumulator provide further cooling and increase the density of the antiprotons by a factor of about 10^6. It takes four to six hours for the antiproton population in the Accumulator to reach $\sim 2 \times 10^{11}$ which is enough for a "shot" into the MR.

Next, the antiprotons are transferred to the MR, accelerated to 150 GeV and then injected into the Tevatron, travelling in the direction opposite to that of the protons. The Tevatron is in the same tunnel as the MR, but uses

much stronger superconducting magnets which, operating at a temperature of 4.7 K, produce a field of $\sim$ 4 Tesla. In the final step, the 6 bunches of protons (typically 1×10^{11} per bunch) and six bunches of antiprotons (typically 5×10^{10} per bunch) are simultaneously raised to full energy i.e. 0.9 TeV for run the 1992-1993 run (christened "run 1A"). Once at full energy, the beams are squeezed very hard at two beam crossing points, BØ (CDF) and DØ . Due to all the manipulation, the beams freshly injected into the Tevatron carry a considerable amount of halo and other debris which must be removed. This is accomplished by a process known as "scraping" whereby metal plates collimate the beam. This must be performed before the detectors start collecting data. Over time, the beams decrease in density due to scattering with residual beam gases in the vacuum tube, beam-beam effects (obeying the second law of thermodynamics) and $p\bar{p}$ collisions. The typical lifetime of a beam is approximately 20 hours after which its quality falls below the lowest acceptable standard. During this time, the antiproton source runs continuously so that a "stack" of antiprotons is ready when the next shot is needed. Thanks to improvements in several aspects of the accelerator system, run 1A saw a record instantaneous luminosity ($\sim 9.0 \times 10^{30} \mathrm{cm}^{-2}\mathrm{s}^{-1}$), a record stacking rate (4.54×10^{10}/hour), and a record Integrated Luminosity in a week (1.48 pb^{-1}).

Chapter 3

The detector: DØ

The DØ detector presently in operation at the DØ collision hall at Fermilab has been constructed to study $p\bar{p}$ collisions at $\sqrt{s} = 2$ TeV in the Tevatron collider. Figure 3.1 shows a cut-away view of the detector.

The prime focus of the DØ experiment is to study high mass states and large p_T phenomena. This includes the search for the top quark, critical tests of the standard electroweak theory through precision study of the W and Z bosons, various studies of perturbative QCD (PQCD), the production of b quark hadrons as well as searches for new phenomena beyond the "Standard Model". Such goals call for the features on which the detector has been optimized [47], namely, excellent identification and measurement of electrons, photons, muons and good measurement of parton jet momenta covering the full 4π solid angle and the resultant fine measurement of the missing transverse energy ($\vec{\not{E}}_T$) which is the signature of neutrinos and other non-interacting particles. The detector design that emerged from the negotiation between these ambitions and the obvious constraints on available resources featured

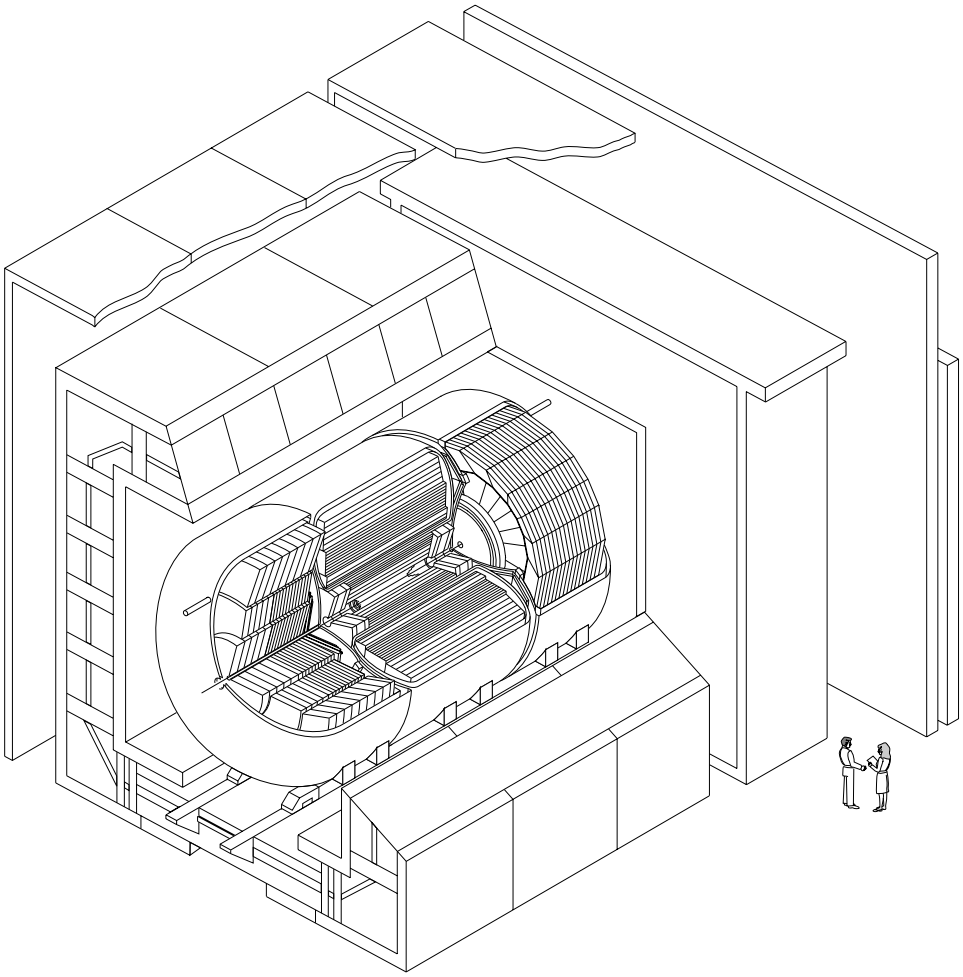

three major components:

Figure 3.1: A cutaway isometric view of the DØ detector.

• A compact non-magnetic central tracking system at the core. This system consists of four subdetectors and is known collectively as the Central Detector (CD). The CD traces the charged particle trajectories with adequate spatial resolution and also offers measurements of the absolute charge (using $\frac{dE}{dx}$ in drift chambers) and the absolute charge-to-mass ratio (using transition radiation) of the particles. These measurements are crucial in suppressing the backgrounds to electrons.

• A finely segmented thick sampling calorimeter that is hermetic, radiation-hard, compensating and stable over an extended period of time. The detector employs liquid argon (LAr) as the active material and uranium, stainless steel and copper plates as absorbers. The calorimeter forms the layer between the innermost CD and the outermost muon system. It is the heart of the DØ detector that provides accurate measurement of energy for photons, electrons and jets and the total transverse momenta of neutrinos and other non-interacting particles. It also offers confirmation for muons based on its trace of a minimum ionizing particle (MIP).

• A muon system with thick magnetized iron absorbers sandwiched between layers of proportional wire drift chambers. This allows momentum measurement for muons while keeping backgrounds from hadron punchthrough to a minimum.

All of the above components have a common denominator in that they rely on the production of charged particles in their sensitive volumes initiated by the particles of primary interest. Consequently, each component requires strong, well-controlled electric fields to drive these charged secondaries which carry all the available information about the primary to the readout channels in an orderly manner. It is thus of vital importance to develop and maintain a robust and reliable high-voltage system that keeps the detector alive.

Finally, all of these are of little use without a system that allows the experimenters to be in continuous communication with the detector. The huge amount of information coming out of more than 100000 channels at a tremendous rate requires an extremely sophisticated data acquisition system

(DAQ) to make efficient use of it. At DØ , this comprises of 3 levels of online triggers that sequentially sift out the most interesting events and store them for offline scrutiny.

In this chapter we will present a brief overview of some of these subsystems, a thorough understanding and proper functioning of which is essential for our analysis.

First, let us define the coordinate system we shall be using. Following the common practice, we use a right-handed cylindrical coordinate system to describe the events at DØ. The pole is at the nominal interaction vertex about which the detector is centered. The direction of the proton defines the polar axis (the z axis, $\theta = 0$). The azimuthal axis is horizontal such that $\phi = \pi/2$ points vertically upward. The center of mass (CM) of the partons involved in the hard-scattering is not necessarily at rest in the laboratory frame at a hadron collider. Only the z component of its boost is likely to be significant. This fact motivates the definition of "rapidity" of a parton:

$$y = \ln(\frac{E + p_z}{E - p_z}) \tag{3.1}$$

$\frac{d\sigma}{dy}$ is invariant under the Lorentz transformation for β_z. Conventionally, the "pseudorapidity" defined as

$$\eta \equiv -\ln(\tan\frac{\theta}{2}) \tag{3.2}$$

is measured. For $M \ll E$, $\eta \approx y$. Vectors in the detector are usually defined by r,η and ϕ.

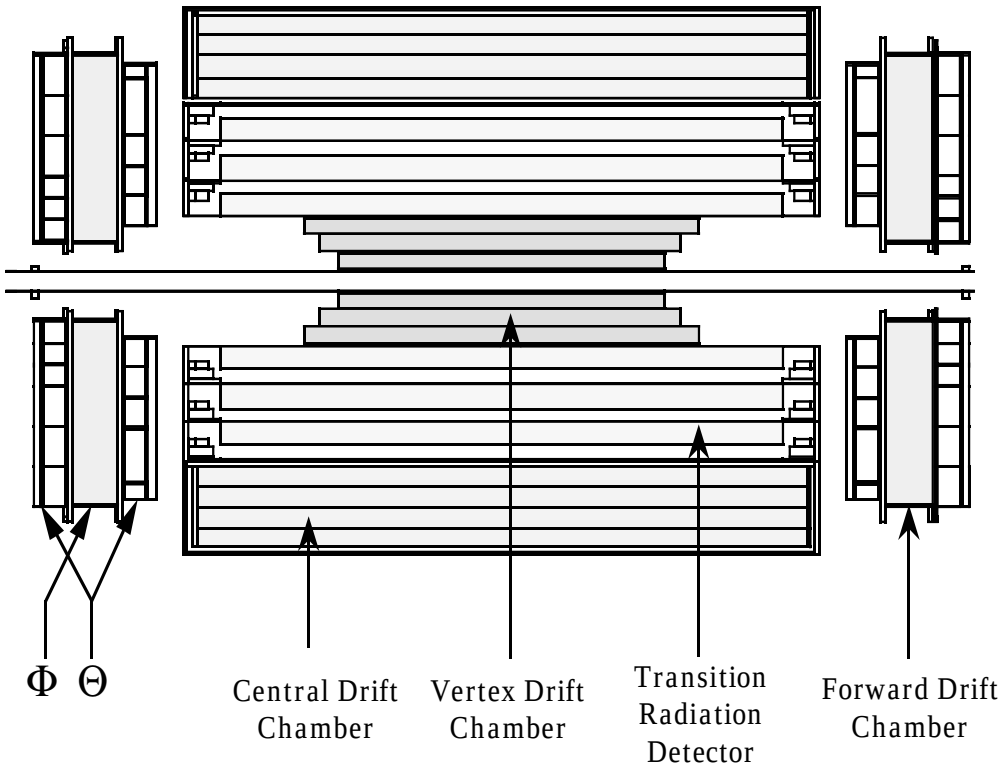

Figure 3.2: A side-view of the DØ central tracking system.

3.1 The central tracking system

A side-view of the the central tracking system at DØ , commonly known as the central detector (CD), is shown in Figure 3.2. It consists of four subdetectors. The lack of a magnetic field within the tracking volume has the obvious disadvantage of rendering the CD incapable of determining the momenta of the particles it tracks. However, it has some advantages too. A non-magnetic volume simplifies the job of tracking. For a given technology, it also allows a smaller volume: a consideration that becomes of critical importance as one moves outwards to the calorimeter and the muon systems where the size is a major limiting factor. Simpler technology and smaller size of the CD results in substantial savings in the overall cost of the detector.

3.1.1 Principle of operation of drift chambers

Three of the four subdetectors of the CD are drift chambers. The fourth employs drift chambers too, as one of its two components. We shall review the basic working principle of drift chambers before going on to describe each subdetector individually. A detailed account of the principle of operation of drift chambers can be found in References [48],[49]. In the gaseous medium of a drift chamber, an energetic charged particle causes ionization along its trajectory by Coulomb interactions. Sometimes the liberated electrons have sufficient energy to cause further ionization in the medium. Within statistical fluctuations in the macroscopic scale, the number of ion-pairs thus produced is proportional to the magnitude of the charge on the particle and independent of its energy in the highly relativistic limit. Particles such as the high-energy electrons that we are interested in cause sufficient ionization for detection at the cost of a negligible fraction of their total energy.

A well-controlled electrostatic field leads the swarm of electrons to drift towards an anode wire commonly known as a "sense wire" (SW). A multiwire drift chamber has several SWs strung parallel to each other forming a plane which usually divides the chamber in two symmetric halves. Consequently, this plane is often referred to as the "wire midplane". A detector typically has dozens of independent drift chambers, each called a "cell". The size of a cell is limited by the time-interval between successive bunch-crossings and the velocity of drift electrons in the gaseous medium. The electrostatic field in a cell divides its active volume into parts bearing a one-to-one correspondence with

the SWs. Roughly speaking, an ionization electron finds its way to the sense wire closest to its site of creation. The small diameter of a SW (typically 20 μm - 50 μm) makes the field very strong in its immediate vicinity. This accelerates the drift electrons to energies high enough to cause further ionization in the medium leading to an avalanche multiplication. The signal amplification factor defined as the ratio between the number of electrons arriving at the SW to the number before the commencement of the avalanche effect is known as the "gas gain". Physical parameters are tuned to achieve a gas gain typically of a few tens of thousands which yields the optimal detection efficiency. The pulse formed by the electrons deposited on an SW are read out at one or both ends. A set of thicker field-shaping wires is usually strung between each pair of SWs to control the field near the latter and to reduce the coupling between them.

The velocity of the drift electrons is determined by the strength of the field and the composition, pressure and temperature of the medium with no dependence on the particle that initiated the process. The time spent by the pulse in traversing the path in the wire and the time between the collision and the initiation of the ionization process being negligible compared to the drift time, the difference between the known time of collision and the time of arrival of the signal at the readout gives the drift time. With a properly calibrated and monitored medium, this can be readily translated into a drift distance. The resolution is limited by the statistical fluctuations in the gaseous medium which are much higher compared to the denser solid state tracking devices. The solid state trackers are also faster and more compact.

Since the individual drift times do not tell which side of the midplane the electrons drifted from, each signal on a SW can be mapped onto two points on the plane perpendicular to it: one corresponding to the true track and the other to its mirror image. Thus arises the so-called question of "left-right ambiguity" for each segment (of a track) in a cell. This dilemma is easily resolved. A slight staggering of the SWs about the midplane breaks the symmetry between its two sides. Then the set of points corresponding to the segment of a true track, which is known to be a straight line in a non-magnetic volume, lends itself to a straight-line fit better than the set of mirror-images. If a track is built of multiple segments, a more powerful rejection of mirror images is achieved by the relative staggering of wire midplanes between cells in different layers (which contain the segments). Again, the idea is the same. A cut on the quality of the fit thus does a very good job of rejecting the mirror tracks with an excellent efficiency for the true tracks. This technique is applied in all the drift chambers at DØ whenever there is a left-right ambiguity to be dealt with.

The drift-distance information from a set of SWs forming a single midplane defines only the plane parallel to the individual SWs which contains the track (this plane is not necessarily parallel to the SW plane). By itself, this is not sufficient for the complete reconstruction of the track in three dimensions. One needs to fix another plane in order to solve for the track as the line of intersection between the two. Having another set of SWs forming a different midplane in a subsequent layer is one way of doing it. However, this would double the thickness of the tracking volume. Alternatives requiring

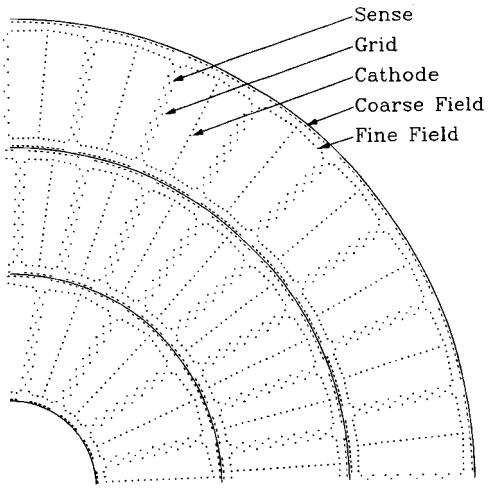

Figure 3.3: An end-view of one quadrant of the DØ vertex detector.

less additional volume are available and employed at DØ at the cost of some resolution. Each of the three tracking detectors at DØ has its own way of handling this which we will discuss individually. Finally, once the track is fully reconstructed in three dimensions, the amount of charge deposited on a sense wire, which is a measure of ionization per unit length of the charged particle track ($\frac{dE}{dx}$) can be used to determine the number of charge quanta associated with it.

A charged particle going through the "crack" of the boundary wall between two cells eludes either. To make up for this, it is often necessary to split the available depth into two or more layers of chambers with cell boundaries of subsequent layers staggered with respect to each other. The part of a track reconstructed by a cell is termed a "segment". This way, even if one segment is lost in a crack, a track can be built from those which are not.

Volume covered	r: 3.7 cm - 16.2 cm (in 3 layers of equal thickness) z: $\pm$48.5 cm (L0); $\pm$53.5 cm (L1); $\pm$58.5 cm (L2)
Cells	16 in Layer 0, 32 each in Layers 1 & 2
Sense wires (SW)	8 per cell; radial separation = 4.6 mm; stagger = 100 μm
Wire specifications	Anode: 25 μm NiCoTin; Field wires: 152 μm Au plated Al
Total channels	1280 (2 per SW)
SW voltage	+2.5 KV
Gas	CO_2 (0.95) + C_2H_6 (0.05) + H_2O (0.005) P = 1 atm; T = 25°C
Gas gain	$\sim 4 \times 10^4$
Mean drift field	$\sim$ 1 KV/cm
Mean drift velocity	$\sim$ 7.3 μm/ns
Resolution	$r\phi$: $\sim$ 60 μm; z : $\sim$ 1.5 cm

Table 3.1: Some important parameters for the DØ VTX.

3.1.2 The Vertex Chamber (VTX)

The innermost of the detectors, the VTX's main purpose is to determine the co-ordinates of the primary vertex (or vertices in case of multiple interactions). This knowledge is crucial for the calculation of the transverse energy of the objects detected by the calorimeter. It should be mentioned here that at DØ we do not rely exclusively on the VTX for this piece of information.

As shown in Figure 3.3, the VTX has 3 layers (numbered from 0 to 2) each supported by thin G10 bulkheads mounted on carbon fiber support tubes. Titanium tie rods connect each bulkhead to the next inner carbon fiber tube to support the wire tensions. The wire midplanes project onto the beamline

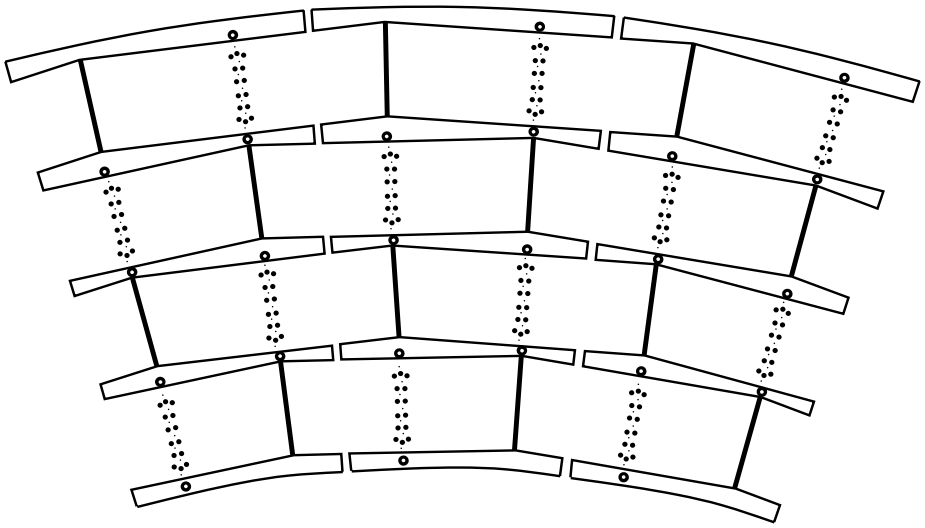

Figure 3.4: An end-view of one "3/32" of the DØ central drift chamber.

with the SWs, of which there are 8 per cell, running parallel to it. Drift distances are used to determine the coordinates of the vertex in the $r\phi$ plane. The resistive SWs are read out at both ends. The relative strength of the signals at the two ends is then translated into the z co-ordinate of the hit on a SW. This technique, known as "charge division", provides the supplementary information necessary for the complete reconstruction of a track in 3 dimensions. Some key numbers are summarized in Table 3.1 [50][51]. The very high flux density and limited space makes the reconstruction a difficult job in the VTX. Although the spatial resolution is quite good for a drift chamber, its efficiency for finding secondary vertices necessary for tagging b quark jets is rather poor.

3.1.3 The Central Drift Chamber (CDC)

The CDC performs the task of tracking in the Central volume of $| \eta | < 1.2$. It has a modular construction. 32 separate identical modules are assembled into a cylindrical shell, a part of which is shown in Figure 3.4. Each module is made from a Rohacell structure ("shelves" connected by "side-walls") covered with epoxy-laden Kevlar and coated with a double layer of 50 μm Kapton. Grooves are cut into each shelf to accommodate a Teflon tube containing the delay line (DL) where the wire midplane intersects the shelf. A field-shaping cage is printed with resistive ink on the Kapton surface with resistive ink. This cage, together with the anode wires (two between every pair of SWs) and the SWs themselves provide the desired field pattern inside the chamber. Each cell has 7 SWs parallel to the beam line with the wire midplane projecting onto it. The drift distance measurements are used for tracking in the $r\phi$ plane. The z coordinate is measured using the DLs of which there are two in each cell. A DL in the CDC consists of a coiled wire wound on a carbon fiber rod. A pulse on the nearest SW induces a signal on a DL. A higher gas gain (using higher voltage) and a grounded guard wire separates each outer SW (OSW) from the inner SWs (ISW) in an effort to minimize the possibility of an ISW inducing a signal on a DL. The signal induced on a DL propagates in either direction with a known velocity and is recorded at both ends. The time interval allows one to calculate the z-position of the inducing pulse. Thus, for a single track, there is a maximum of 28 points for a fit in the $r\phi$ plane and 8 in the rz plane. Some key numbers are listed in Table 3.2 [50][52][53][54].

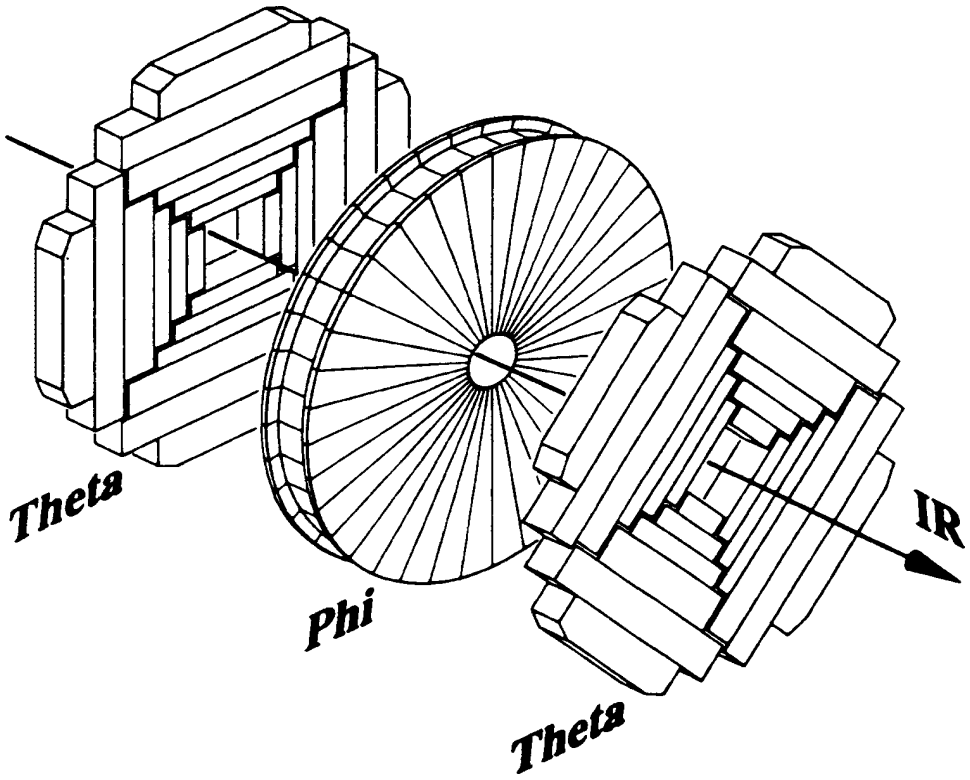

Figure 3.5: An exploded isometric view of one of the DØ forward drift chambers.

3.1.4 The Forward Drift Chambers (FDC)

As the name suggests, the purpose of the FDC is to perform tracking in the forward region which it does down to $|\eta| \approx 3.1$. One at each end, an FDC package consists of 3 modules: a Φ module sandwiched between a pair of Θ modules. Figure 3.5 shows an exploded isometric view of one FDC package. The Φ module performs tracking in the $r\phi$ plane and the Θ module, in the $r\theta$ plane. The FDC thus uses drift distances to construct two planes whose line of intersection gives the track. The materials used for construction are similar to those for the CDC. Each cell in a Φ module has 16 SWs strung radially with the wire midplanes projecting onto the beamline. A Θ module has four

mechanically disjoint quadrants, each containing 6 cells. The length of a cell is proportional to its distance from the beamline. The 3 inner cells have the wire planes close to a wall. In these cells, there is no left-right ambiguity to be resolved. Each cell in a Θ module has 8 SWs and one delay line. For an event consisting of a single charged particle passing through the FDC, the two planes determined by the Φ and the Θ chambers would suffice for a complete 3D reconstruction of the track, rendering the delay line information superfluous. However, in the rather busy environment of the FDC in a typical hard-scattering process, there are often many tracks passing through a cell giving rise to many close combinations of planes. In such cases, the delay line provides a local measurement of ϕ to aid the correct matching of planes. Some key numbers are listed in Table 3.3 [50][55][56].

3.1.5 The Transition Radiation Detector (TRD)

When a charged particle crosses the boundary between two media with different dielectric or magnetic properties, photons are emitted in order to accommodate the abrupt change in the electromagnetic field. This phenomenon is known as "transition radiation" [57]. For highly relativistic particles ($\gamma > 10^3$), the radiation is primarily in the X-ray band, emitted strongly forward into a cone described by an angle $\alpha \propto \frac{1}{\gamma}$ with respect to the particle direction. An important feature of such radiation is that its intensity increases linearly with γ. The lightest of the charged hadrons, a pion is 275 times heavier than an electron. So, to produce transition radiation of the same intensity, ideally a

charged pion would have to have 275 times the energy of an electron. At the Tevatron, electrons are the only charged particles likely to be produced with sufficient energy to induce detectable transition radiation. The DØ TRD is built to exploit this fact (however, let us not forget that nothing is ideal in the real world where separation of signal and background using the TRD proves to be a little more complicated than this might lead one to imagine).

For us, the most serious background to electrons comes from the electromagnetic jet produced by an energetic π^0 (decaying to $\gamma\gamma$) which has an associated track due to an overlapping low-energy charged particle. A magnetic field in the tracking volume would provide an excellent handle for the suppression of this background. In a detector like DØ , which has no magnetic field in its central tracking system, the measurement of transition radiation intensity can be used as a viable alternative.

One interface between two media of different dielectric constants does not suffice for reliable signal detection. Practical detectors are made up of stacks of thin foils, thereby providing many interfaces. The DØ TRD occupies the annular region between the VTX and the CDC. and is likewise cylindrically symmetric with respect to the beam-line [47][58]. It has three layers, each employing a "radiator stack" comprised of 393 layers of 18 μm thick polyethylene foil with a mean separation of 150 μm in a volume filled with nitrogen gas. Following each radiator stack radially outward, there is a two-stage drift chamber to accomplish the detection of the X-rays. Photoelectric absorption of the X-rays results in ionization of the gaseous medium producing a swarm of electrons mainly in the 15 mm first ("conversion") stage of the chamber. The

charged primary also causes some direct ionization by Coulomb interactions. These electrons drift radially outward to the 8 mm second ("amplification and detection") stage of sense cells where the avalanche occurs. Xenon is employed as the drift gas because of its small attenuation length for X-rays. The 2 m long TRD has a pseudorapidity coverage of $-1.0 < \eta < 1.0$. 256 sectors covering the full azimuth give the TRD a fine segmentation in ϕ. In principle, the z-coordinate of a hit can be determined from the helical cathode pads, but this has not yet been achieved in practice. This limits its utility to relatively clean events only. Its signal rapidly loses meaning as the activity in an event in addition to the electron candidate to be tagged increases. A likelihood analysis of the TRD signal offers a rejection factor of 50 against pions with an efficiency of 0.90 for the electrons under the test-beam conditions.

3.2 The calorimeter

We shall first discuss the principles of operation of the DØ calorimeter briefly and then give some details of the apparatus.

3.2.1 Principles of sampling calorimetry

The purpose of a calorimeter is to measure energy. In particle detectors, this means measuring the energies of various particles. In the suitably chosen medium of a calorimeter, a particle is made to pass through so much material that it comes to rest after transferring all of its energy to the medium. This energy goes into the production of secondary particles. Some of the secondaries

may be energetic enough to produce tertiaries and so on. The cascade that ensues is called a "shower" which continues to develop until a final state is reached where all the particles have energies below the threshold required for the production of a further generation. By studying the distribution of charged particles in the fully developed shower, one can classify it as either an electromagnetic or a hadronic shower with good confidence and also estimate its energy.

In a "sampling calorimeter" such as the one at DØ , "absorber" plates made of some material of very high density are arranged to form layers alternating with layers of an "active" medium [59]. The layers usually form planes normal to the direction of the incident primary. The absorber plates help contain the shower in a manageable volume, but the part of a shower contained in the absorber volume cannot be read out. It is the live material that allows the study of charged particle distribution. The name "sampling calorimeter" owes its origin to the fact that only that fraction of the shower's total energy which is deposited in the active volume is sampled. Not surprisingly, this fraction is known as the "sampling fraction". The detector is calibrated by measuring the sampling fractions accurately at the test-beam facility.

Electromagnetic and hadronic showers have marked differences in their characteristics owing to the fundamental difference between the dominant physical processes underlying them [60]. At high energies the electromagnetic showers result predominantly from bremsstrahlung losses by electrons and pair production by photons passing through a material medium. On an average, the energy retained by an electron of incident energy E_0 after passing

through a distance x in a medium is given by

$$\langle E(x) \rangle = E_0 e^{-\frac{x}{x_0}} \tag{3.3}$$

x_0 is known as the radiation length and is a characteristic of the medium given approximately by

$$x_0 \frac{A}{Z^2} \times 180 \text{ gcm}^{-2} \tag{3.4}$$

where Z is the number of protons and A, the number of nucleons in the nuclei of the medium. DØ uses an electromagnetic calorimeter that is $20.5x_0$ thick in order to ensure that no electron would carry a significant fraction of its incident energy beyond it. The bremsstrahlung cross-section is inversely proportional to the square of the mass of the incident particle and increases logarithmically with the square of its Lorentz γ factor. At the Tevatron energies, any charged particle other than the electron is too heavy to lose a significant fraction of its energy by direct bremsstrahlung in the electromagnetic section (or in any other section) of the calorimeter. Charged particles also deposit some energy by ionization in the medium. For electrons, this effect dominates only below 100 MeV. Muons, which lose very little energy by bremsstrahlung, however do leave a trail of ionization in the calorimeter. Such a trace associated with a so-called "minimum ionizing particle" (MIP) plays a decisive role in the identification of muons at DØ .

In the following discussion, we shall use the terms "electron" and "positron" interchangeably. Our model assumes that at the energies of our interest, the sign of the charge is of no consequence; what is said of electrons applies to

equally to positrons and this model does indeed work very well. Above $\sim$ 100 MeV, electrons lose energy almost entirely by bremsstrahlung. For photons with energy greater than $\sim$ 100 MeV, the dominant process is production of an e^+e^- pair. These two processes keep repeating alternately until all the final state particles are below $\sim$ 100 MeV. In either case, the final state particles have an opening angle that is relatively small. This means that electromagnetic showers (which can be initiated either by an electron or by a photon) tend to be rather narrow compared to hadronic showers which we'll discuss next. Below 100 MeV, electrons lose energy primarily by ionization and photons by photoelectric absorption or Compton scattering. The expected number of charged particles in the shower is proportional to the energy of the initial electron or photon.

The development of a hadronic shower in matter is quite a bit more complex than that of an electromagnetic shower, making in unamenable to analytic treatment which makes it less well understood [61]. A high-energy hadron incident on a block of material eventually interacts with a nucleus of the medium via strong interaction. A generation of strongly interacting particles is thus produced to which the largest fraction of the incident hadron's energy is transferred on an average. A typical secondary hadron is produced with a transverse momentum of 350 MeV, so that hadronic showers tend to be more spread out both laterally and longitudinally than electromagnetic showers. A large portion goes into the production of π^0s (a π^0 decays promptly into two photons) and photons that initiate localized electromagnetic subshowers within the hadronic shower. The charged secondary hadrons cause ionization in the

medium creating electric charge, the only quantity that the device can read. However, typically a third of the incident hadron's energy goes into processes that leave little or no signature in the calorimeter. These include the binding energy needed to break up the nuclei and the energy carried off by neutrinos and muons. Sometimes long-lived neutral hadrons like neutrons and K_L^0s can also escape undetected. The fraction of unseen energy has a much larger fluctuation in hadronic showers than in electromagnetic showers rendering the resolution of the former's energy proportionately poorer. The longitudinal and lateral development of hadronic showers scale with the nuclear interaction length defined as

$$\lambda \approx \frac{Z}{A\sigma_{\rm abs}} \tag{3.5}$$

where σ_{abs} is the cross-section for the nucleus-hadron inelastic collision. The relation

$$\frac{\lambda}{x_0} = 0.12Z^{\frac{4}{3}} \tag{3.6}$$

holds for high-Z materials, indicating that the higher the Z of the material, the easier it is to distinguish between electromagnetic and hadronic showers on the basis of their profiles. There are other criteria that dictate the choice of the live and the absorber materials in a calorimeter. One desirable feature is that the calorimeter's response to a shower should be independent of the size of its electromagnetic component at all energies, i.e. if e is the calorimeter's response to an electron and h that to a hadron (eg. $\pi^{\pm}$), both of energy E, then one would like to have $\langle e/h \rangle = 1$ for any E. A calorimeter with this feature is called "compensating". The choice of uranium as the absorber and liquid argon

(LAr) makes the DØ calorimeter nearly compensating with $\langle e/h \rangle = 1.11$ at 10 GeV falling to $\langle e/h \rangle = 1.04$ at 150 GeV. In some sections, stainless steel (SS) or copper (Cu) is used as the absorber. The very high Z of uranium helps make the detector compact and offers good hadron rejection from electromagnetic showers. Use of LAr also makes the calorimeter "unit gain", i.e. one in which no amplification (by avalanche multiplication) is needed for the detection of the charged secondaries. This makes the calorimeter stable over time: a single round of calibration before the first online commissioning can be expected to suffice for the entire life of the detector. One disadvantage and a major technical challenge is that the whole calorimeter must be kept in a cryostat to maintain the low temperature. A few words about energy resolution is in order before we review the DØ calorimeter briefly in the next section. The resolution of a sampling calorimeter can be expressed as follows [62]:

$$(\frac{\sigma_{_E}}{E})^2 = C^2 + \frac{S^2}{E} + \frac{N^2}{E^2} \tag{3.7}$$

where E is the energy of the incident particle and $\sigma_{_E}$ its resolution. The first of the three terms on the right hand side corresponds to the constant errors due to miscalibration such as fluctuations in the energy of the test-beam, the thickness of the LAr gaps etc. The second and the most important term is due to the sampling fluctuations. This is purely statistical in nature and can be justified by a naive treatment: Since the number of ions produced ($N_{\rm ion}$) is expected to be proportional to E,

$$\langle N_{\rm ion} \rangle = \alpha E \tag{3.8}$$

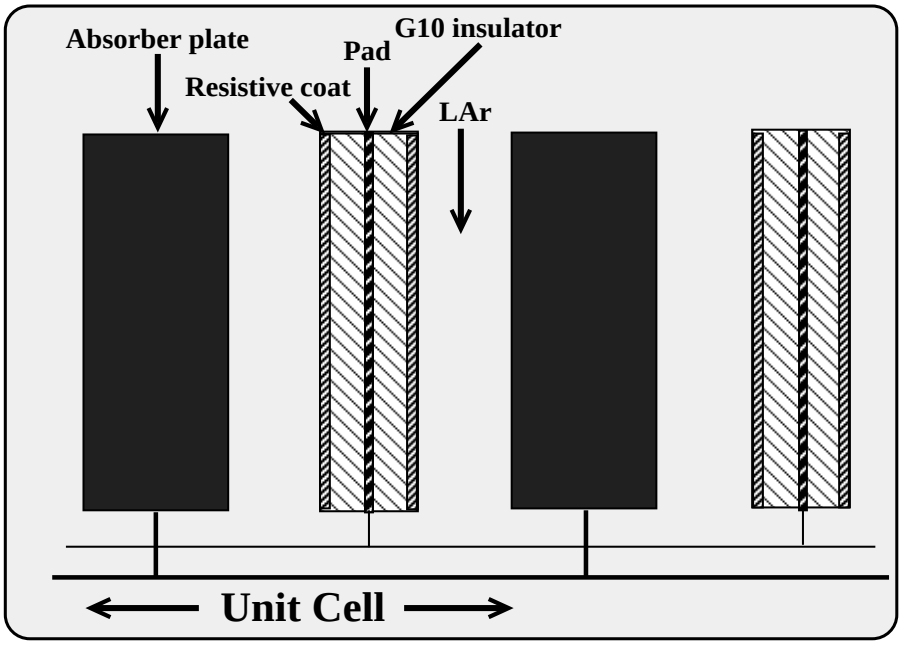

Figure 3.6: A schematic view of a unit cell of the DØ sampling calorimeter

and the detected signal D is proportional to $N_{\rm ion}$,

$$D = \beta N_{\rm ion} \tag{3.9}$$

therefore, applying Gaussian approximation to the Poisson distribution of $N_{\rm ion}$ ($N_{\rm ion}$ is large enough to justify this approximation) we get

$$\frac{\sigma(D)}{\langle D\rangle} = \langle N_{\rm ion}\rangle^{-1/2} = \alpha^{-1/2}\langle E\rangle^{-1/2}. \tag{3.10}$$

The last term arises from the noises such as electronic noise and the noise induced by the radioactivity of the absorber.

3.2.2 The apparatus

Figure 3.6 gives a schematic view (not to scale) of a single cell of the DØ calorimeter [47]. The thickness of an absorber plate varies between 3 mm

and 46.5 mm depending on the module. LAr fills the gap of 2.3 mm between two adjacent absorber plates. A signal board is placed in the gap. The signal board consists of a copper readout pad sandwiched between two layers of G10 with a resistive layer of epoxy coating on their outer surfaces [63]. The epoxy is maintained at a positive potential with the copper plates at ground, the typical field strength being 8.7 KV/cm. The charge collected by the epoxy induces a signal on the readout pad. As opposed to a drift chamber or a scintillator, no amplification of the signal takes place in the medium itself, so the signal can be quite small. Thus, several cells are ganged together to increase the signal size and reduce the number of electronic channels. To allow access to the CD enclosed by the calorimeter, DØ has its main calorimeter system divided in 3 parts: one central and two endcaps, each submersed in a separate double-walled stainless steel cryostat. The central calorimeter (CC) provides coverage for roughly $\mid \eta \mid < 1$. Two endcap calorimeters (EC), each a mirror image of the other, extend the coverage to $\mid \eta \mid = 4$. There are also devices to plug some cracks that remain between the main systems. The calorimeters are modular in construction with a rather complicated geometry, but the general features are described below.

To best exploit the differences between the developments of electromagnetic and hadronic showers within the physical constraints, the modules are divided into three distinct classes: electromagnetic (EM), fine hadronic (FH) and coarse hadronic (CH). The names and locations of the various calorimeter module types at DØ are shown in Figure 3.7 which is a magnification of Fig-

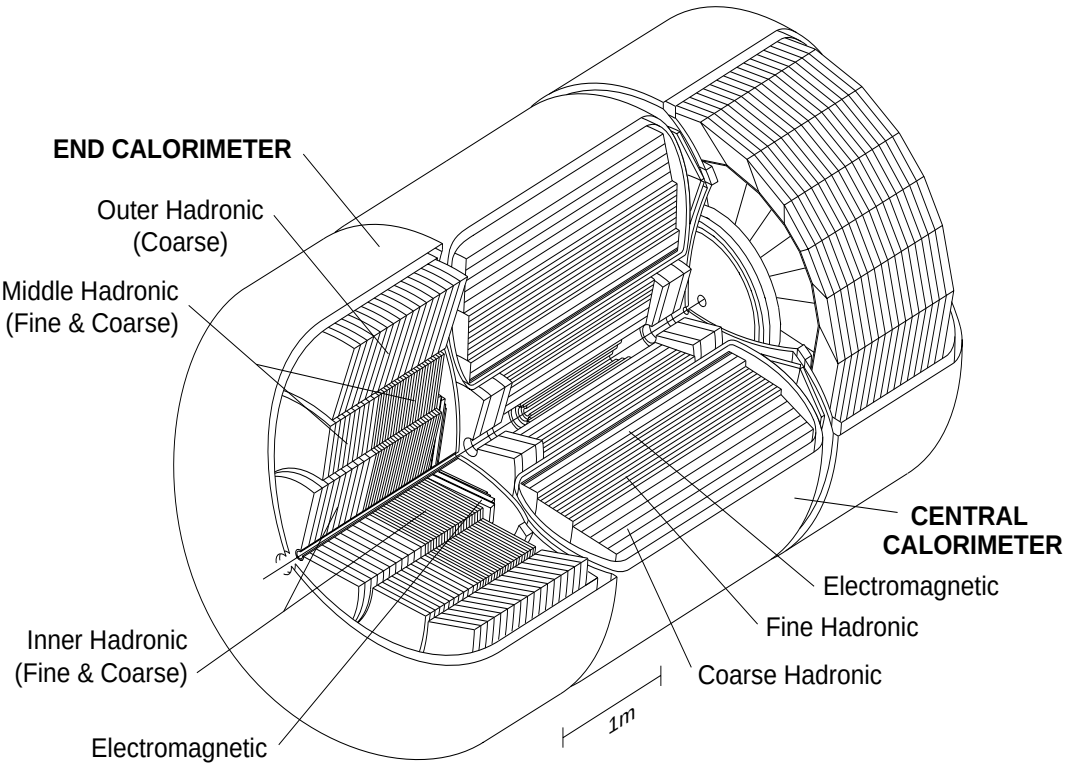

Figure 3.7: A cut-away view of the DØ calorimeter.

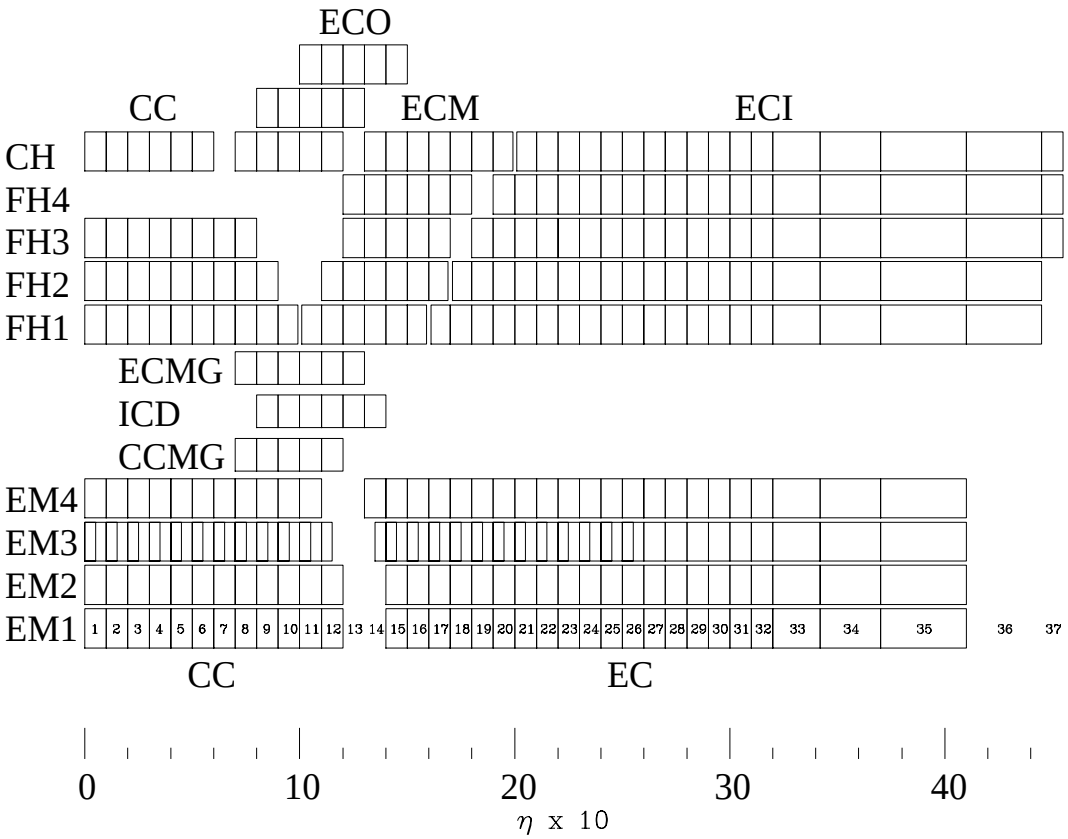

Figure 3.8: Projection of the DØ calorimeter on the $r\eta$ plane.

ure 3.1 without the muon system. The lateral and longitudinal segmentation of the DØ calorimeter is shown in Figure 3.8. The EM modules are closest to the nominal interaction point and are designed for full containment of electromagnetic showers. Their fine segmentation, longitudinally as well as laterally, is necessitated by the relatively short and narrow shape of electromagnetic showers. The EM modules have thin (3 to 4 mm) U plates. The FH modules have thicker U plates (6 mm). The bulk of a hadronic shower is expected to be contained within the EM and FH modules. The CH modules with their Cu (in CC) and SS (in EC) absorber plates are intended for the final containment of hadronic showers should any portion of it extend beyond the FH modules.

The lateral segmentation of the entire calorimeter is based on pseudo-

projective towers. Most of the towers have a projective dimension of $\Delta\phi = 0.1$, $\Delta\eta = 0.1$. One exception is the third of the 4 layers in the EM section where an electromagnetic shower is expected to deposit most of its energy. Lateral segmentation in this layer is $\Delta\phi = 0.05$, $\Delta\eta = 0.05$. Fine segmentation such as this would be harder to implement using, for example, scintillator tiles or proportional wire chambers for the live volume. For large η, the spatial dimensions of $\Delta\eta = 0.1$ is rather small. Hence, in the high η region, some towers have a coverage of $\Delta\eta$ larger than 0.1. As a reference, a typical hadronic jet is expected to be contained within a cone of $\Delta R \equiv \sqrt{\Delta\phi^2 + \Delta\eta^2} \approx 0.7$.

There is a fair amount of uninstrumented material in the region of $0.8 <\mid \eta \mid < 1.4$ due to the cryostat walls and the support hardware. Two additional subsystems are employed to sample the showers in this region: the massless gaps (MG) and the intercryostat detectors (ICD). An MG has no absorber; it consists of a single readout board placed between the cryostat wall and the calorimeter modules. There are 160 readout channels per CCMG and 192 per ECMG. The ICDs are mounted outside the cryostats between the CC and each EC. They consist of plastic scintillator tiles with photomultipliers at the readout. The ICD tiles match the pseudoprojective structure of the rest of the calorimeter totalling 192 channels for each detector array.

Some parameters for the CC and the EC modules are shown in Tables 3.4 and 3.5 respectively [45]. The radiation and interaction lengths quoted apply to normal incidence. In the EC, the fine and coarse hadronic modules are grouped into middle (MFH, MCH) and inner (IFH, ICH) sections for readout purposes. There is also an additional outer hadronic (OH) section in the EC to

plug a gap. The MCH and the OH readout channels are summed for $|\eta| > 1.4$. Thus, the table shows that these two module types share 64 channels.

The performance of the DØ calorimeters have been extensively studied at the test-beam facility. $C = 0.003 \pm 0.002$ and $S = 0.157 \pm 0.005\ \sqrt{\text{GeV}}$ were obtained for electrons in the ECEM and $C = 0.032 \pm 0.004$ and $S = 0.41 \pm 0.04\ \sqrt{\text{GeV}}$ for pions in the ECMH. The noise terms are negligible compared to these.

The position resolution is critical for electromagnetic jets since electrons are identified by matching a calorimeter cluster with a track in the CD. This resolution varies from 0.8 mm to 1.2 mm in the EM3 layer (shower maximum) over the full range of impact positions for 100 GeV electrons. The position resolution varies approximately as $E^{-1/2}$.

3.3 The muon system

Being too heavy for substantial bremsstrahlung and not participating in strong interactions, highly relativistic muons which are stable particles for the purpose of our detector, penetrate the calorimeter leaving only the trace of a minimum ionizing particle. In fact, other than the neutrinos, these are the only known particles capable of carrying a large transverse momentum past the calorimeter. They are measured in the muon detection system which forms the outermost layer of the DØ detector. The sideview of the entire DØ detector in Figure 3.9 highlights the muon system. The DØ muon detection system has five separate solid-iron toroidal magnets, namely three for the Wide An-

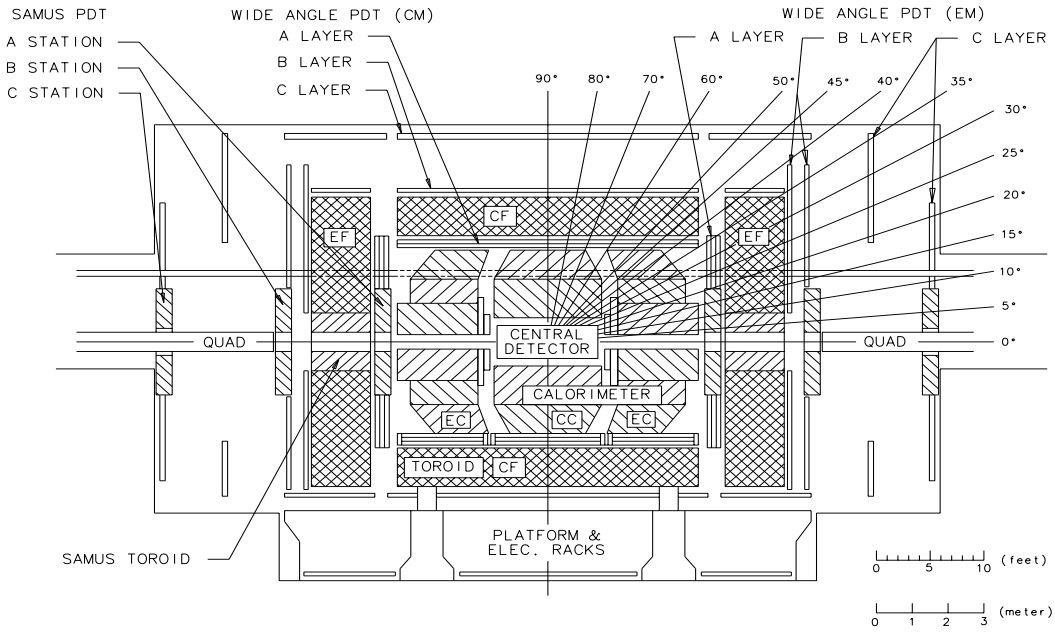

Figure 3.9: Elevation of the DØ detector.

gle MUon Spectrometer (WAMUS, one central iron (CF) and two end iron (EF) pieces) and two for the Small Angle MUon Spectrometer (SAMUS) [47]. Each of these magnets is sandwiched between layers of proportional drift tubes (PDT). The incident trajectory is determined from the interaction vertex and one layer (A) of PDTs that tracks the particle immediately before it enters the magnetic field of about 1.9 Tesla in the 1.7 m thick iron and two layers (B and C), separated by 1.7 m or more, track it after it has emerged from the field. The muon momentum is determined from the bend angle. The momentum resolution is limited mainly by multiple Coulomb scattering in the calorimeters and the iron. Each PDT has a rectangular cross-section and contains a single sense wire strung through its center. Several decks of PDTs make up a layer. The magnetic field bends the trajectory of a particle originating from

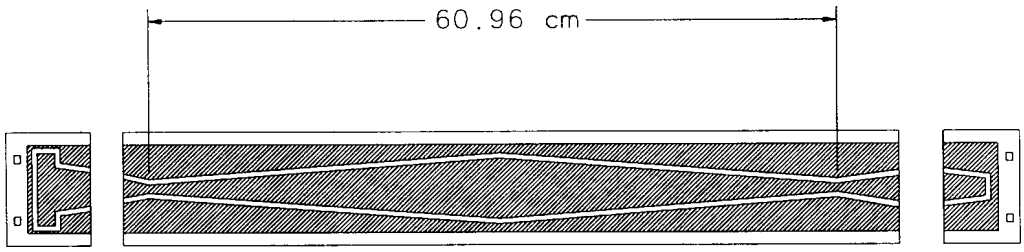

Figure 3.10: A WAMUS cathode pad.

the vertex mainly in the $r\eta$ plane. The sense wires run perpendicular to the beam direction so that the bend angle can be calculated from the accurate measurement of the drift distances. The time-to-distance map for the drift is fairly non-linear due to non-uniformity of the drift field. To map the track in the $r\phi$ plane, measurements of position have to be performed along the direction of the sense wires. This is done in two stages [64]. In the first stage, each sense wire is read out at both ends. The interval (Δt) between the times of arrival at the two ends provide a primary coarse measurement with a resolution of $\sim$ 10 cm. Each of the two walls of the PDT that are hit by a particle originating from the vertex have two cathode pads etched on them. The widths of the pads vary along the length in the shape of repeated diamond-like patterns with a wavelength of $\sim$ 61 cm as shown in Figure 3.10. A pulse on the sense wire induces one on each of the cathode pads. The widths of the cathode pads being a function of the position of the pulse on the sense wire along its length, so are the relative strengths of the induced pulses on the inner and the outer pads. Therefore, in the second stage, the measurements of the charge deposited on the cathode pads can be translated into the longitudinal position of the hit on the sense wire modulo the half-wavelength of the periodic pattern.

The Δt measurement performed in the first stage helps resolve this periodic ambiguity in the second stage where the resolution is about 3 mm. The muon system can measure the charged particle trajectories down to approximately 3° from the beam pipe.

Table 3.6 summarizes some of the important characteristics of the muon system.

3.4 The data acquisition system

The total cross section of $\overline{p}p \rightarrow X$ is approximately 70 mb ($= 7 \times 10^{-26}$ cm^2). At the typical luminosity of 5×10^{30} cm^{-2}s^{-1}, this translates into $\overline{p}p$ collisions at the rate of about 350 KHz. Only a very small fraction of these interactions are of interest to the experimenters. The DØ data acquisition (DAQ) system comprises of 3 levels of triggering to filter out the uninteresting events during online operation (i.e. these events are not recorded) and to perform a preliminary classification of the interesting events retained for offline analysis [47][65]. We shall briefly describe each of the levels individually before concluding this chapter. A simplified schematic diagram of the DØ DAQ is presented in Figure 3.11.

3.4.1 Level Ø (LØ)

LØ is a hardware trigger whose purpose is to tag the bunch-crossings which contain events that can be labeled "hard (or inelastic) scattering". To accomplish this, two hodoscopes in the forward regions are employed, one

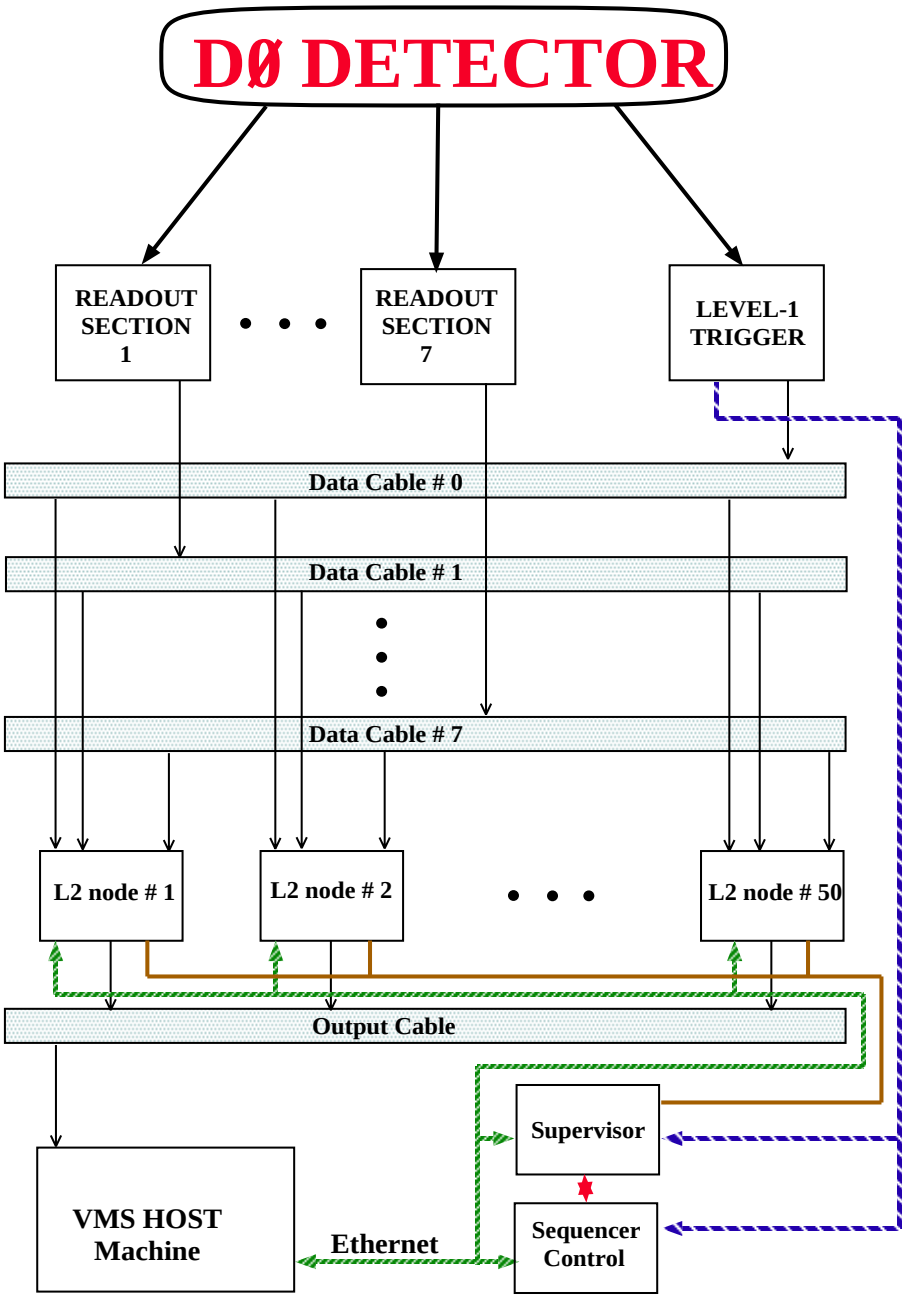

Figure 3.11: A schematic block-diagram of the DØ data acquisition system.

between each FDC and the neighboring EC cryostat [66],[67]. Each hodoscope consists of two arrays of rectangular scintillator tiles arranged at right angles to each other. Coverage in pseudo-rapidity is full between $2.3 <| \eta |< 3.9$. Due to the rectangular shape, only a partial coverage extends up to another 0.4 units in η on either side.

The LØ trigger registers the presence of an inelastic collision by detecting particles produced at low angles with respect to the beam. The probability of the requirement of coincidence between signals from the two hodoscopes being met by an inelastic collision exceeds 0.99. Timing information on the arrival of a signal at each array allows a crude determination of the z coordinate of a collision. A fast decision can be obtained within 800 ns of the beam-crossing with a resolution of 15 cm. A slower decision with a resolution of 3.5 cm takes about 2.1 μs. However, due to technical problems, this z information was not available for a part of run 1A.

3.4.2 Level 1 (L1)

L1 is another level of hardware triggers. A total of 32 triggers were available at L1 for run 1A. Each trigger is a logical combination of 256 programmable bits whose inputs come from LØ , the calorimeter and the muon system [68]. Since the L1 has only the 3.5 μs between two bunch crossing to make a decision, it can afford only the "fast z information" from LØ although for run 1A this provision was not enabled; only a fixed nominal value was used to calculate the transverse energies. The calorimeter trigger coverage extends

to $\mid \eta \mid = 3.2$ in towers of 0.2×0.2 in the $\eta\phi$ space. Each "trigger tower" is further divided longitudinally into electromagnetic and hadronic sections. Thresholds on the E_T in the electromagnetic section of a trigger tower were used for various electromagnetic triggers (provisions for hadronic veto were available, but never used) while thresholds on the E_T in the entire tower (electromagnetic + hadronic) were used to tag jet candidates. Scalar and vector sum (for $\not\!\!E_T$) of the tower E_T's were also used for some triggers. For the muons, a loose requirement is made on aligned hits in the wire chambers. Hits are required in at least two layers within a 3-column ($\sim$ 60 cm) wide road in the WAMUS. Also used were some configurations of level 1 muon triggers which took several bunch-crossing intervals for decision. These are called level 1.5 triggers.

3.4.3 Level 2 (L2)

When an event is validated by L1, a complete digitization of the signals followed by a readout of the entire detector takes place. The event is then passed on to the L2 "software trigger system" for final filtering [69]. One member of the L2 computer farm consisting of 48 Microvax 4000-60's partially reconstructs and tests the event under a set of algorithms (also called "tool"s) for every L1 trigger satisfied. Specific tools for jets, electrons, photons, muons, $\not\!\!E_T$ and scalar E_T add up to a total of 128 [70].

The events passed by L2 proceed to the "host" computer system to be logged on tape under the template of "ALL stream". The maximum rate

at which L2 could handle input events was about 200 Hz for run 1A. The pass rate into the ALL stream was limited to about 2 Hz. This rate is still too high for the offline reconstruction farm to keep up with in real time. A subset of the ALL stream events that passed some particularly stringent L2 tools are labeled "EXPRESS stream" to merit special special attention as the most interesting events. These events are immediately processed with the current reconstruction code and are recorded on separate tapes (these events are written on the ALL stream tapes as well). The pass rate into the EXPRESS stream is approximately 0.2 Hz.

3.5 Remarks

The overview presented in this chapter is only intended to provide the bare minimum of a groundwork deemed necessary for understanding the data analysis that follows. Several critical aspects such as the detailed organization of the data acquisition system, the high-voltage system, the monitoring and control systems, the clock etc have been completely omitted. Sufficient details of these systems are available in Reference [47].

Volume covered	r: 49.5 cm - 74.5 cm (in 4 layers of equal thickness); z: $\pm$90.0 cm
Cells	32 per layer
Sense wires (SW)	7 per cell; radial separation = 6.0 mm; stagger = 200 μm
Wire specifications	Anode: 30 μm Au plated W; Cathode: 125 μm Au plated CuBe
Delay lines (DL)	2 per cell
DL velocity	2.35 mm/ns
Total channels	1408 (1 per SW, 2 per DL)
SW voltage	+1.45 KV (ISW); +1.58 KV (OSW)
Gas	Ar (0.93) + CH_4 (0.04) + CO_2 (0.03) + H_2O (0.005)
	P = 1 atm; T = 25°C
Gas gain	$\sim 2 \times 10^4$ (ISW); $\sim 6 \times 10^4$ (OSW)
Mean drift field	$\sim$ 620 V/cm
Mean drift velocity	$\sim$ 34 μm/ns
Resolution	$r\phi$: $\sim$ 180 μm; z : $\sim$ 2.9 mm
Tracking efficiency	0.89 (for isolated tracks)

Table 3.2: Some important parameters for the DØ CDC.

Chamber	Φ	Θ
Volume covered	r: 11.0 cm - 61.3 cm	11.0 cm - 62.0 cm (almost)
	$\mid z \mid$: 113.0 cm - 127.0 cm	104.8 cm - 111.2 cm (inner layer)
		128.8 cm - 135.2 cm (outer layer)
Cells	36	6 per quadrant
		(4 quadrants per layer, 2 layers)
Sense wires (SW)	16 per cell	8 per cell
	separation = 8.0 mm; stagger = 200 μm	
Wire specifications	Anode: 30 μm Au plated W; Cathode: 163 μm Au plated Al	
Delay lines (DL)	None	1 per cell
DL velocity	-	2.35 mm/ns
Total channels	576 (1 per SW)	480 (1 per SW, 2 per DL)
SW voltage	+1.50 KV	+1.55 KV (ISW)
		+1.65 KV (OSW)
Gas	Ar (0.93) + CH_4 (0.04) + CO_2 (0.03) + H_2O (0.005)	
	P = 1 atm; T = 25°C	
Gas gain	$\sim 3.6 \times 10^4$	$\sim 2.3 \times 10^4$ (ISW)
		$\sim 5.3 \times 10^4$ (OSW)
Mean drift field	$\sim$ 950 V/cm	$\sim$ 750 V/cm
Mean drift velocity	$\sim$ 37 μm/ns	$\sim$ 40 μm/ns
Resolution (drift)	$\sim$ 200 μm	$\sim$ 300 μm
Tracking efficiency	0.85 (for isolated tracks)	

Table 3.3: Some important parameters for the DØ FDC.

Calorimeter	EM	FH	CH
Number of modules	32	16	16
Absorber	U	UNb	Cu
Absorber thickness (mm)	3.0	6.0	46.5
LAr gap (mm)	2.3	2.3	2.3
Number of readout layers	4	3	1
Number of cells per layer	2,2,7,10	20,16,14	9
Total radiation lengths (x_0)	20.5	96.0	32.9
Total interaction lengths (λ)	0.76	3.23	3.17
Sampling fraction	0.1179	0.0679	0.0145
Total channels	10368	3000	1224
η coverage	$\pm$1.2	$\pm$1.0	$\pm$0.6

Table 3.4: Some important parameters for the DØ Central Calorimeter.

Calorimeter	EM	IFH	ICH	MFH	MCH	OH
Number of modules	1	1	1	16	16	16
Absorber	U	UNb	SS	UNb	SS	SS
Absorber thickness (mm)	3.0	6.0	6.0	6.0	46.5	46.5
LAr gap (mm)	2.3	2.1	2.1	2.2	2.2	2.2
Number of readout layers	4	4	1	4	1	3
Number of cells per layer	2,2,6,8	4×16	14	4×15	12	3×8
Total radiation lengths (x_0)	20.5	121.8	32.8	115.5	37.9	65.1
Total interaction lengths (λ)	0.95	4.91	3.57	4.05	4.08	7.01
Sampling fraction	0.1190	0.0566	0.0153	0.0668	0.0164	0.0164
Total channels	7488	4288	928	1472	384+64+896	
$\mid \eta \mid$ coverage	1.3-3.7	1.6-4.45	2.0-4.45	1.0-1.7	1.3-1.9	0.7-1.4

Table 3.5: Some important parameters for the DØ Endcap Calorimeters.

Number of layers	3 (2 or 4 in some regions)
Number of decks per layer	4,3,3
Total number of modules	164
Total number of cells	11386
Interaction lengths (λ)	9.5 - 18.7
$\mid \eta \mid$ coverage	3.6
Drift gas	Ar (0.90) + CO_2 (0.05) + CF_4 (0.05) P = 1 atm; T = 25°C
Wire specifications	50 μm Au plated W; tension = 300g
High voltage	Anode (sense wires) : +4.56 KV Cathode pads: +2.3 KV
Max. drift distance	5.0 cm
Mean drift velocity	65 mm/μs
Resolution	drift distance: 0.2 mm position along the sense wire: 3 mm bend angle: 0.2 mrad momentum: $\delta p/p = ((0.18)^2 + (0.01 \cdot p)^2)^{\frac{1}{2}}$

Table 3.6: Some important parameters for the DØ muon detector.

Chapter 4

Particle identification and measurement

In this chapter we will discuss the identification and measurement of various particles/partons of our interest such as electrons, quarks (or gluons) and neutrinos, from the electronic readout of the detector. The quarks and gluons, after hadronization, appear as jets in the calorimeter. In general, these jets will not overlap with an electron by our definition (a part of our backgrounds owes its source to the rare occasions when statistical fluctuations lead to such overlaps as we shall see in the next chapter). The ability to differentiate between the signature of a quark from that of a gluon of equal energy would be very precious to us since all the jets from our signal, with the exception of possible gluon radiations in the initial and final states, are originated by quarks whereas most of our backgrounds come from jets initiated by gluons. Unfortunately, as of now, we do not have this ability. Thus, we shall discuss the two in the same subsection under the common heading of "jets". As discussed in the previous chapter, neutrinos appear as $\not\!\!E_T$ in our detector.

Since muons, photons and taus are not of primary interest to us, we shall

not cover them here. The identification and measurement of muons is a process more involved than that of any other object at DØ . The interested reader is referred to the excellent discussion provided in Reference [45]. As with the quarks and the gluons, at present we cannot discern between the calorimetric signatures of an electron and a photon of the same energy. However, the central tracking system offers strong discrimination between the two exploiting the difference in their electric charges. The tracking part aside, everything said about the electrons is equally valid for the photons. W's and Z's are tagged neither by the trigger framework nor by the global reconstruction program although many triggers are designed specifically to accept the events containing them. We study these gauge bosons based on their decay products ($W \rightarrow e\nu$, $Z \rightarrow ee$).

Most of the primary calibration of our detector was done at the test-beam (TB) facility. There are various characteristics of collisions that cannot be simulated by the TB. Also, there are unavoidable, albeit undesirable, differences between the prototypes calibrated at the TB and the actual modules used to study the collisions. Hence, the measurements obtained using the calibration constants carried over from the studies of the TB data need to be corrected for these effects. For each particle/parton or "object", we shall devote a section, with a subsection each for the object's "definition", "correction" to the measured value and the "resolution" of the measurement.

The identification of an object is done at various stages. First, a preliminary tagging of candidates is done online by the trigger framework. Offline, the first pass on the reconstruction of an event is performed by a software package

called "DØRECO ". For each event, this rather elaborate program first converts the electronic signals into measurements in the position and momentum spaces using the calibration constants stored in static parameter (STP) banks. Subsequently, it identifies various physical entities such as electrons, photons, muons, jets and neutrinos in the event using those measurements. The final definition of an object in terms of the observed signatures often depends on the topic of interest. The natures, cross-sections and levels of understanding of the signal and background processes determine the optimal set of cuts. Therefore, in defining an object, DØRECO uses rather loose selection criteria in an attempt to form a generic superset of objects, retaining enough information about each to allow finer discrimination downstream. We will give the definition of each object relevant to us first as it is in the trigger system, then as in DØRECO and finally, as in our analysis where we impose the tightest set of cuts.

4.1 Electrons

4.1.1 Definition

An electron is identified by detecting an electromagnetic (EM) shower in the calorimeter with an associated track in the central tracking system. At the trigger level, no tracking requirement was enforced during run 1A. At Level 1 (L1), only a trigger tower (0.2×0.2 in the $\eta\phi$ space) above a certain threshold in the electromagnetic section of the calorimeter is required (several

pass/fail bits are available for different thresholds). When such a threshold requirement is met, Level 2 (L2) examines the candidate's longitudinal and transverse profiles in a cluster formed around the L1 EM trigger tower [71]. The longitudinal shower shape is determined from the energy depositions in the 4 EM layers ($EM_i(i = 1 \ldots 4)$) and the innermost of the fine hadronic layers ($FH_1 \equiv EM_5$) in a 3×3 column around the hottest EM cell. The energy fractions are defined as

$$f_i \equiv \frac{EM_i}{\sum_{i=1}^{5} EM_i} \tag{4.1}$$

Upper and lower cuts are made on various f_i's. The most important requirements are $f_5 < \delta$ (the value of δ ranges from 0.03 to 0.15 depending on the energy (E) and pseudorapidity (η) of the cluster) and $0.1 < f_3 < 0.9$. f_1, f_2, f_4 are not used in most of the L2 "scripts".

The study of the transverse profile of a candidate is based on the pattern of energy deposition in EM_3 where most of an electron's energy is expected to be deposited (shower-maximum). The segmentation of this layer is 0.05×0.05 in the $\eta\phi$ space compared to 0.1×0.1 in most of the other layers. A smaller (core) cone and a larger (isolation) cone are defined, both centered on the hottest cell. The definition of the cones are different in the central and the endcap calorimeters: 0.15×0.15 and 0.25×0.25 rectangles in the EC and regions of comparable area in the CC. The energy in the annular region between the two cones is required to be small compared to the energy in the core cone, as one would expect of an isolated electron. The value of the cut, again, depends on the E and η of the cluster.

The cuts on the shape of an electromagnetic shower were tuned with test beam (TB) data to provide an efficiency of at least 0.99 for real electrons. Tests with collider data confirm that the efficiency of Level 2 cuts is high.

Offline, DØRECO makes stringent requirements on the distribution of energy within the shower and the quality of track-match in order to achieve the optimal signal-to-noise ratio in the identification of electrons. Beam tests conducted using electron and pion beams allow us to quantify the expected shape of such showers.

The identification of electrons in DØRECO proceeds through the following steps:

- Clusters are formed of adjacent towers (0.1×0.1 projective units in $\eta \times \phi$) with a significant amount of energy in the EM section of the calorimeter using a "nearest-neighbor" bridging algorithm [72].

- At least 0.4 of the energy of the cluster is required to be contained in a single tower. This is a strong requirement on the transverse containment of the shower.

- To qualify as an electron candidate, a cluster must have more than 0.9 of its total energy deposited in the EM calorimeter. Evidently, this is a cut on the longitudinal containment of the shower. Test beam measurements indicate that this cut has an efficiency greater than 0.99 for electrons between 10 GeV and 150 GeV in E_T.

If, in addition to satisfying the above conditions, a track is found by the central tracking system within $\Delta\eta = \pm 0.1$, $\Delta\phi = \pm 0.1$ of the centroid of the cluster,

then DØRECO brands the cluster as an electron. If no track is found within that window, then it is branded as a photon.

After being certified as an electron by DØRECO , an EM shower has to satisfy several additional requirements in order to qualify as an electron in our analysis [73]:

- Desirable shower profile: To quantify how well the pattern of energy deposition in a shower conforms to that expected of an electron or a photon, we calculate its χ^2 with respect to a covariance matrix calibrated on Monte Carlo electrons with E_T ranging from 10 GeV to 150 GeV. For an array $\vec{X}$ of D elements, the covariance matrix V is defined as [74]

$$V \equiv \frac{1}{N}\sum_{i=1}^{N}(\vec{x}(i) - \langle\vec{X}\rangle)(\vec{x}(i) - \langle\vec{X}\rangle) \tag{4.2}$$

where $\vec{x}(i)$ is the i-th of N measurements of $\vec{X}$ and

$$\langle\vec{X}\rangle \equiv \frac{1}{N}\sum_{i=1}^{N}\vec{x}(i) \tag{4.3}$$

is the expectation value of $\vec{X}$. We can define the "H-matrix" as

$$H \equiv V^{-1} \tag{4.4}$$

if $V_{ij}^2 \neq V_{ii}V_{jj}$ for all $i \neq j$. Subsequently, the scalar χ^2 for a measurement $\vec{x}$ of $\vec{X}$ is defined as

$$\chi^2 \equiv \vec{x}H\vec{x} \tag{4.5}$$

which measures how consistent it is with that expected from an electron. The fractional energies in layers 1,2 and 4 of the EM calorimeter, the

fractional energies in each cell of a 6×6 array in layer 3 (shower maximum) centered on the tower with the maximum energy, the interaction vertex determined by the central tracking system and the logarithm of the total cluster energy makes $D = 41$ for us. The last variable takes into account the dependence of deposition pattern on the cluster energy. There is a matrix for each of the 37 rings into which the calorimeter is subdivided in $|\eta|$.

The variable χ^2 does not quite follow the "χ^2 distribution" since for us, the individual elements of $\vec{X}$ are not distributed as gaussian variables. Nevertheless, studies show that it remains an extremely powerful variable to discriminate between signal and background. Figure 4.1(a) shows the distribution for χ^2 for the electrons from the $Z \rightarrow ee$ candidates compared to that for EM clusters from a loose L2 trigger. We require $\chi^2 < 100$ of the electrons in our analysis. This cut has an efficiency of 0.93 for electrons both in the CC and the EC.

- Good transverse isolation: We further expect an electron from a W decay to be isolated from other objects in the event. Let $E_{\rm tot}(0.4)$ be the total energy deposited in the cone $R = 0.4$ around the electron direction and $E_{\rm EM}(0.2)$ the energy deposited in the electromagnetic section of the calorimeter in the cone $R = 0.2$ about the same axis. We then define the isolation variable as

$$f_{\rm iso} \equiv \frac{E_{\rm tot}(0.4) - E_{\rm EM}(0.2)}{E_{\rm EM}(0.2)} \tag{4.6}$$

The solid histogram in Figure 4.1(b) shows the distribution of $f_{\rm iso}$. We

require $f_{\rm iso} < 0.1$. The efficiencies in the CC and the EC are 0.98 and 0.97 respectively.

- Excellent track-match: An important source of background for electrons is due to photons from the decay of neutral mesons such as π^0 or η which are copiously produced in $p\bar{p}$ collisions. This background doesn't create a track in the central detector (CD), but may acquire one if a soft charged particle flies in the same direction. Its charge creates a track, but its energy is low enough not to cause a significant perturbation in the photons' shower profile. This is a major disadvantage of not having a magnetic field in the CD volume which could provide an independent measurement of the momentum of the charged particle. Without the magnetic field, the only way to effectively remove such background is to have a calorimeter which can determine the center of gravity (COG) of the shower with a resolution that's good enough to allow an accurate matching with a track found by the CD (the TRD, as remarked earlier, offers little help at this time in the events of our interest). We define the COG of a shower as follows:

$$\vec{r}_{\rm COG} \equiv \frac{\sum_i w_i \vec{r_i}}{\sum_i w_i} \tag{4.7}$$

where the subscript i stands for the cell index within the cluster and the weight w_i is defined as

$$w_i = \max\left(0, w_0 + ln\left(\frac{E_i}{\sum_i E_i}\right)\right) \tag{4.8}$$

E_i being the energy deposited in the i-th cell. w_0 is a parameter chosen to

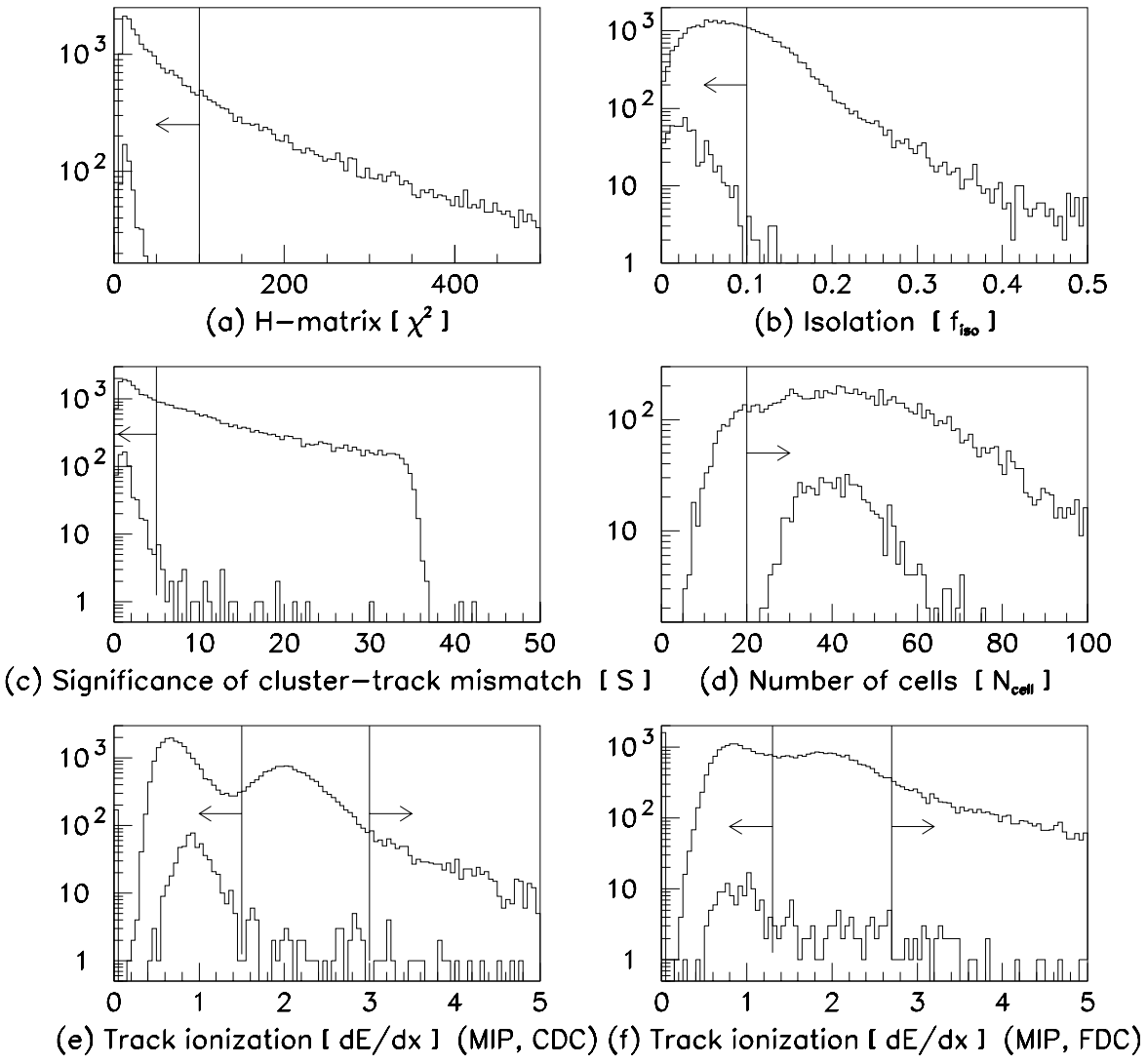

Figure 4.1: The variables used for the identification of electrons: (a) H-matrix χ^2; (b) cluster isolation ($f_{\rm iso}$); (c) significance of cluster-track mismatch (S); (d) number of cells in the cluster (N_{cell}); (e) track ionization in the CDC ($\frac{dE}{dx}$ in units of MIP) and (f) track ionization in the FDC ($\frac{dE}{dx}$ in units of MIP).

optimize the position resolution. The logarithmic weighting is motivated by the exponential lateral development of an electromagnetic shower. Results from beam tests indicate that a position resolution of 1.5 mm and 2.0 mm can be achieved in the CC and the ECs respectively.

In order to decide whether a track can be associated with a shower, we calculate the significance of the mismatch (S) between the COG of the shower and the track. This quantity is defined slightly differently in the CC and the EC:

$$S_{\rm CC} \equiv \sqrt{\left(\frac{\Delta\phi}{\sigma_{\Delta\phi}}\right)^2 + \left(\frac{\Delta z}{\sigma_{\Delta z}}\right)^2} \tag{4.9}$$

$$S_{\rm EC} \equiv \sqrt{\left(\frac{\Delta\phi}{\sigma_{\Delta\phi}}\right)^2 + \left(\frac{\Delta r}{\sigma_{\Delta r}}\right)^2} \tag{4.10}$$

where Δx is the mismatch in the variable x and σ_x is its resolution.

The distribution of S shown in Figure 4.1(c). We require $S < 5$. The efficiencies in the CC and the EC are 0.74 and 0.95 respectively for clean isolated electron candidates.

- Number of cells in the cluster: Sometimes a group of adjacent noisy channels (known as "hot cell"s) in the electromagnetic calorimeter can pass even our tightest criteria for an isolated electromagnetic cluster. However, such groups usually consist of fewer cells than expected in a typical electromagnetic cluster. Figure 4.1(d) shows the distribution of the number of cells ($N_{\rm cell}$) in electromagnetic clusters. We require $N_{\rm cell} > 20$.

- Ionization in the CD consistent with that expected of an electron: Since there is no magnetic field in the CD, e^+e^- pairs from photon conversions in the material upstream of the tracking chambers are often not separated and are reconstructed together as a single track. For an e^+e^- pair, the ionization per unit length ($\frac{dE}{dx}$) is expected to be twice that of a single charged particle. The distribution of $\frac{dE}{dx}$ for reconstructed single tracks in the central and the forward drift chambers are shown in Figures 4.1(e) and 4.1(f) respectively. Two clear peaks can be seen in the looser and larger set of electromagnetic clusters with an associated charged track: one due to tracks from single charged particles and the other due to e^+e^- pairs from photon conversions. Background to single electrons from such conversions can be reduced significantly by cutting on the $\frac{dE}{dx}$ of the associated track. To reject 2-MIP candidates (we do not want to reject the 3-MIP candidates since A genuine electron can occasionally have a 3-MIP trace if a photon radiated by it converts before reaching the tracking volume). The cuts are different for the CDC ($\frac{dE}{dx}<$ 1.5 MIP or $\frac{dE}{dx}>$ 3.0 MIP) and the FDC ($\frac{dE}{dx}<$ 1.3 MIP or $\frac{dE}{dx}>$ 2.7 MIP).

In Figure 4.1, the large-statistics histograms correspond to electrons found by DØRECO in events with $\not\!\!E_T$ < 15 GeV (to minimize the contribution from real W's) in the ELE_HIGH trigger (see section 5.2). The small-statistics histograms are made using electrons from a sample of $Z \rightarrow ee$ candidates. The vertical lines show the cuts we make and the arrows point to the sides accepted. The first four plots are based on the Central Calorimeter data only.

In general, the separation between signal and backgrounds is somewhat poorer in the forward region, but the cuts are the same. The combined efficiency for the electron selection defined above is approximately 0.72 and 0.43 in the central and the forward regions respectively [75]. The TRD is designed to offer good rejection of π^0 background to electrons. It has been used effectively in the cleaner environments of W and Z events that do not have much jet activity. However, in a busy environment like ours, it is more difficult to make effective use of it. Our understanding of the performance of the TRD in events of our interest is not yet good enough to allow us to utilize it in this analysis.

4.1.2 Correction

As pointed out in chapter 2, the electromagnetic shower initiated by an electron, a photon or a π^0 is concentrated in a much smaller volume compared to the typical hadronic shower. Also, the longitudinal and transverse profiles of an electromagnetic shower is relatively insensitive to its energy once its E_T is in the region of our interest (above $\sim$ 20 GeV). This fact has a very useful implication: it means that the energy scale is the sole major contributor to the correction of electromagnetic jets. The other factors whose effects increase with the volume of the jet (the next section contains a discussion of these) can be safely ignored. Linearity of response was one of the chief design goals of the DØ calorimeter. Test-beam studies indicate that it has been achieved remarkably well [76]. The process $Z \rightarrow e^+e^-$ has a cross-section that is barely sufficient to provide the statistics needed for the calculation of the energy-scale

correction function from the data accumulated by DØ from run 1A. Knowing M_Z accurately from the measurements performed by the experiments at LEP [77], it was thus possible for us to fix the scale for the electromagnetic jets at DØ .

4.1.3 Resolution

The parameters of Equation 3.7 for an electron is given in Subsection 3.2.2.

4.2 Jets (quarks and gluons)

4.2.1 Definition

At L1, a jet is identified simply by a trigger tower with E_T above some threshold (as with the electron, several pass/fail bits are available to cover a range of thresholds) [68]. The L2 jet algorithm receives a list of jet candidates from L1. A cone of $R = 0.3$ is formed around each candidate, except in cases when the candidate is absorbed by a neighboring jet of a higher E_T. A jet candidate for L2 is comprised of the contents of the cone. Basic properties such as the weighted mean and spread of E_T, η and ϕ, the electromagnetic fraction etc. of each surviving candidate are computed and stored [78]. To filter out interesting events, several cuts can be imposed at L2 e.g. a minimum threshold on the transverse energy, a minimum transverse size of a jet, a minimum number of jets and fiducial cuts on jet pseudorapidity.

Although alternatives are available, most analyses to date at DØ including this one have relied on a fixed-cone algorithm for the offline reconstruction of jets (DØRECO) [79]. Our fixed cone algorithm proceeds as follows:

- Preclustering: from a list of calorimeter towers (typically units of 0.1×0.1 in $\eta\phi$ space) ordered in E_T, seeds are formed centering on the "hottest" tower including all the contiguous towers that have $E_T > 1$ GeV and are within ±0.3 units in η and ϕ of the seed. These seeds are called "preclusters". At the end of this stage, all towers with $E_T > 1$ GeV have been assigned to a cluster. For each precluster, its E_T-weighted centroid defines the axis of the corresponding jet candidate.

- Cone clustering: A cluster is a cone of radius R which is formed around each precluster axis. The axis is redefined by the E_T-weighted centroid of the cluster. This step is repeated until the axis stabilizes. In the rare case of oscillation between multiple solutions, the procedure is terminated after 50 iterations.

- Merging/splitting: If two clusters overlap, they are merged into one if the energy shared is more than half of that of the cluster with smaller E_T, else the shared towers are split between the two clusters by assigning a shared tower to the cluster whose axis it lies closer to.

- A cluster qualifies as a jet if it has $E_T > E_T^{\min}$.

Various values of R ranging from 0.3 to 1.0 are used by the different

analyses with $E_T^{\min} = 8$ GeV for all of them. Other algorithms, for example the "nearest neighbor algorithm" which uses the relative moments of neighboring towers starting from the hottest tower as a seed are available and have been argued to be better, at least for busy events, but they have not been studied thoroughly enough and have not been used in this analysis.

In our analysis, $R = 0.5$ is considered to be the best choice. In the semileptonic decay channel, a $t\bar{t}$ event can be fairly busy. In such an event, using the next higher choice available ($R = 0.7$) frequently results in undesirable merging of jets. On the other hand, using the next lower choice available ($R = 0.3$) can prove too narrow, resulting in loss or undesirable splitting of jets due to the energy flowing out of the cone.

4.2.2 Correction

Our goal is to interpret the energy of a jet as that of the parton that initiated it. From this point of view, there are several factors which result in an incorrect measurement of jet energy at the end of the procedure described above. First of all, the calibration constants carried over from the TB studies may need some modification. In other words, a revision of the jet energy scale may be in order. Energy from the underlying ("spectator") event, energy of the parton escaping the fixed-size cone (hadron showers have a wide spread) and zero-suppression of the calorimeter signal are the three other most important contributors to this woe. After detailed studies, the QCD group at DØ has come up with an elaborate correction scheme for the jets [80][81].

The basic technique we use for the correction of the jet energies was first developed by CDF [82]. The "missing E_T projection factor" (MPF) algorithm, on which our jet energy correction scheme is based, assumes that any jet with a very high electromagnetic content is subject to the scaling described in section 4.1.2. First, from the events which have precisely two jets, those are chosen in which one jet is highly electromagnetic (EM). Specifically, it is required to be labeled as a photon by DØRECO as described in section 4.1.1. Events with a large $\not\!\!E_T$ along the EM jet were dropped to reduce the contamination from $W(\rightarrow \nu) + 1$ *jet* events in which the electron's track was lost in reconstruction resulting in its mislabelling as a photon. The jets are required to be back-to-back in the transverse plane ($\Delta\phi > 130°$). It is now assumed that in each of these events, the EM shower is either a photon or the result of a hadronic jet fluctuating into a large π^0 contribution. Either way, there is no energetic neutrino in the event. Any $\vec{\not\!\!E}_T$ in the event, after the scaling of the EM jet (which can be measured much more precisely than an average non-electromagnetic jet), is thus attributed to a mismeasurement of the other jet.

The "missing E_T projection factor" is defined as

$$MPF \equiv \frac{\vec{\not\!\!E}_T \cdot \hat{n}}{E_T} \tag{4.11}$$

where $E_T$and $\hat{n}$ are the corrected transverse energy and the unit vector along the direction of the EM jet respectively. such that

$$E_{\text{corr}} = E_{\text{meas}}(1 + MPF) \equiv E_{\text{meas}} \cdot f_{\text{MPF}} \tag{4.12}$$

Where $E_{\rm meas}$ and Ecorr are the measured and the corrected energies of the jet respectively. $f_{\rm MPF}$ is determined as a function of the jet energy, direction and electromagnetic content.

The fragmentation products from a final state parton constituting a jet can produce a shower in the calorimeter that is too broad to be fully contained in a fixed cone. This causes a part of the parton's energy to be absent in the measured value. To estimate this out-of-cone fraction, we substituted single particle test-beam showers for fragmentation products in the Monte Carlo event generators ISAJET and HERWIG. We find that typically 4% of the energy is lost for jets reconstructed with a cone of $R = 0.5$ and that this fraction is essentially independent of E_T.

The energy flow from the underlying event is assumed to be independent of the hard scattering that gives rise to the jets we observe. In order to correct for its estimated contribution within the jet cone, we measure the energy density in minimum bias events. An average of 0.6 GeV of E_T per unit area in the $\eta\phi$ space is subtracted from each jet as the contribution from the underlying event.

Much of the DØ calorimeter employs depleted uranium (DU) as the absorber. The asymmetric energy distribution from the residual radioactivity of this DU results in a net positive measured energy deposition after pedestal suppression. Analysis of non-suppressed pedestal data gives an average value of 1.2 GeV to be subtracted for the energy per unit area in the $\eta\phi$ space due to this effect.

Figure 4.2 shows the net correction factor plotted as a function of E_T of

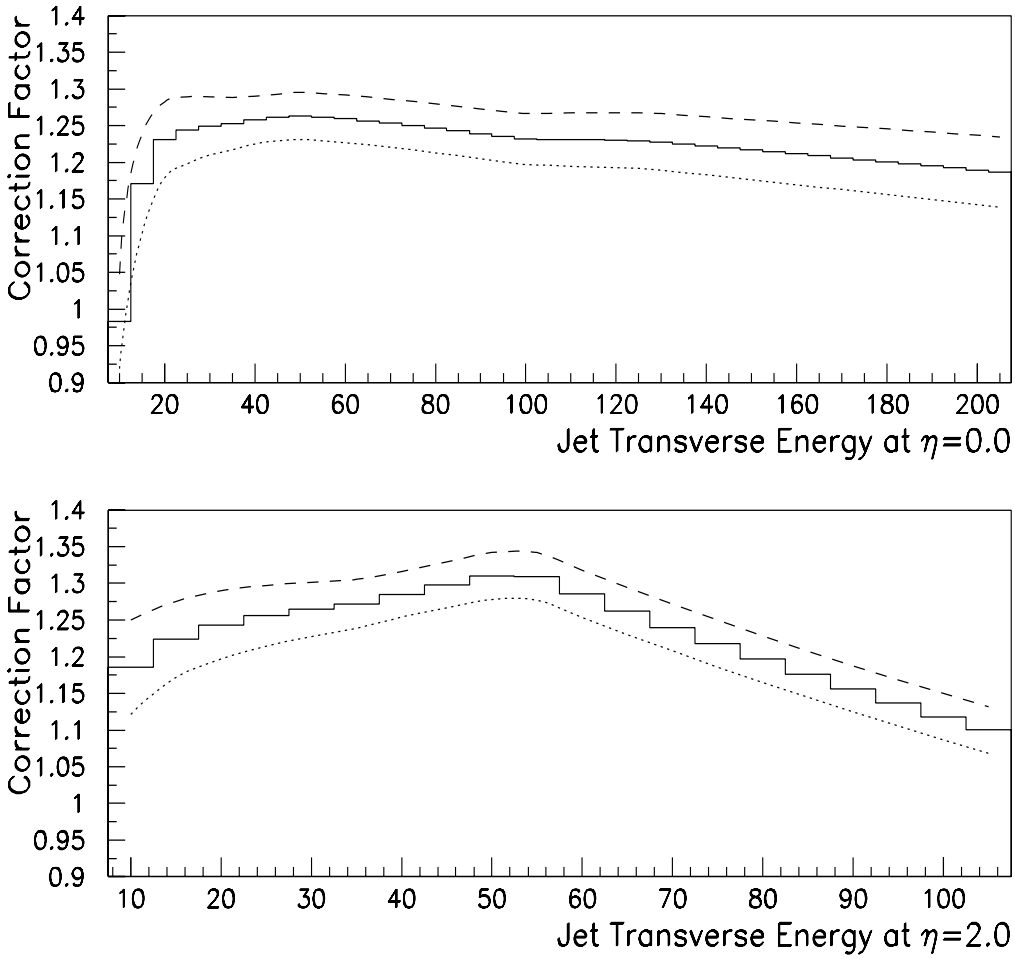

Figure 4.2: The cumulative energy scale correction factor for jets as a function of E_T $(R = 0.5)$ at the two extremes of our range of acceptance in $\mid \eta \mid$.

the uncorrected jet.

In order to investigate the validity of our jet corrections, we examine the properties of $Z(\rightarrow ee) + 1\ jet$ (exclusive) events. Since one expects the $\vec{p}_T$ of the Z ($\vec{p}_T(Z)$) and the $\vec{E}_T$ of the jet ($\vec{E}_T(j)$) to balance, we should have $\not\!\!E_T$ = 0 in these events. Indeed, we find that in the worst case, the mean $\not\!\!E_T$ is reduced from $0.05 \cdot P_T(Z)$ to less than $0.015 \cdot P_T(Z)$. The width of the $\not\!\!E_T$ spectrum is also reduced proportionately.

4.2.3 Resolution

We compute the resolution using the asymmetry variable, ξ, defined for clean dijet events [73]:

$$\xi = \frac{E_T(j_1) - E_T(j_2)}{E_T(j_1) + E_T(j_2)}, \tag{4.13}$$

where $E_T(j_i)$ denotes the E_T of the i^{th} jet in the event (ordered in decreasing E_T). The width of this variable may be written as:

$$(\sigma_\xi)^2 = \left(\left| \frac{\partial \xi}{\partial E_T(j_1)} \right| \sigma_{E_T}(j_1) \right)^2 + \left(\left| \frac{\partial \xi}{\partial E_T(j_2)} \right| \sigma_{E_T}(j_2) \right)^2. \tag{4.14}$$

Upon assuming $E_T(j_1) = E_T(j_2) \equiv E_T$ and $\sigma_{E_T}(j_1) = \sigma_{E_T}(j_2) \equiv \sigma_{E_T}$, the jet $E_T$resolution can be written as:

$$\left(\frac{\sigma_{E_T}}{E_T} \right) = \sqrt{2}\sigma_\xi. \tag{4.15}$$

We use corrected jet energies to compute the asymmetry from which the resolution is determined as a function of the average corrected energy of the two jets.

We expect the resolution to vary with pseudorapidity. It is therefore determined independently for each of the three different $|\eta|$ regions of the calorimeter. Figure 4.3 shows the data, and the fitted resolution curves in each of the three $|\eta|$ regions of the calorimeter as functions of the average corrected energy of the two jets. The best resolution is anticipated in the central region (CC, $|\eta| < 0.8$). The intercryostat region (ICD, $0.8 < |\eta| < 1.5$), which contains uninstrumented material and two different sampling technologies, and the forward region (EC, $1.5 < |\eta| < 3.0$), where large out-of-cone showering corrections introduce significant systematic uncertainties, are both expected to have somewhat poorer resolution. We note that, binned in suitable regions of pseudorapidity and the small contribution to the resolution due to angular smearing ignored, $\frac{\sigma_{E_T}}{E_T} = \frac{\sigma_E}{E}$.

Because we have low statistics for events where both jets are found in the EC (particularly at high E_T), we use dijet events generated with the ISAJET Monte Carlo (MC) generator in conjunction with a full detector simulation to compute the resolution in this region. To convince ourselves of the validity of this exercise, we perform a cross-check by comparing data and MC in the CC and in the ICD. From the good agreement in these regions, we contend that it should be reasonable in the EC as well.

The fitting is done using the functional form given in Equation 3.7. Fitting for each of the three terms C, S and N independently in each η region, we obtain the results shown in Table 4.1 [73].

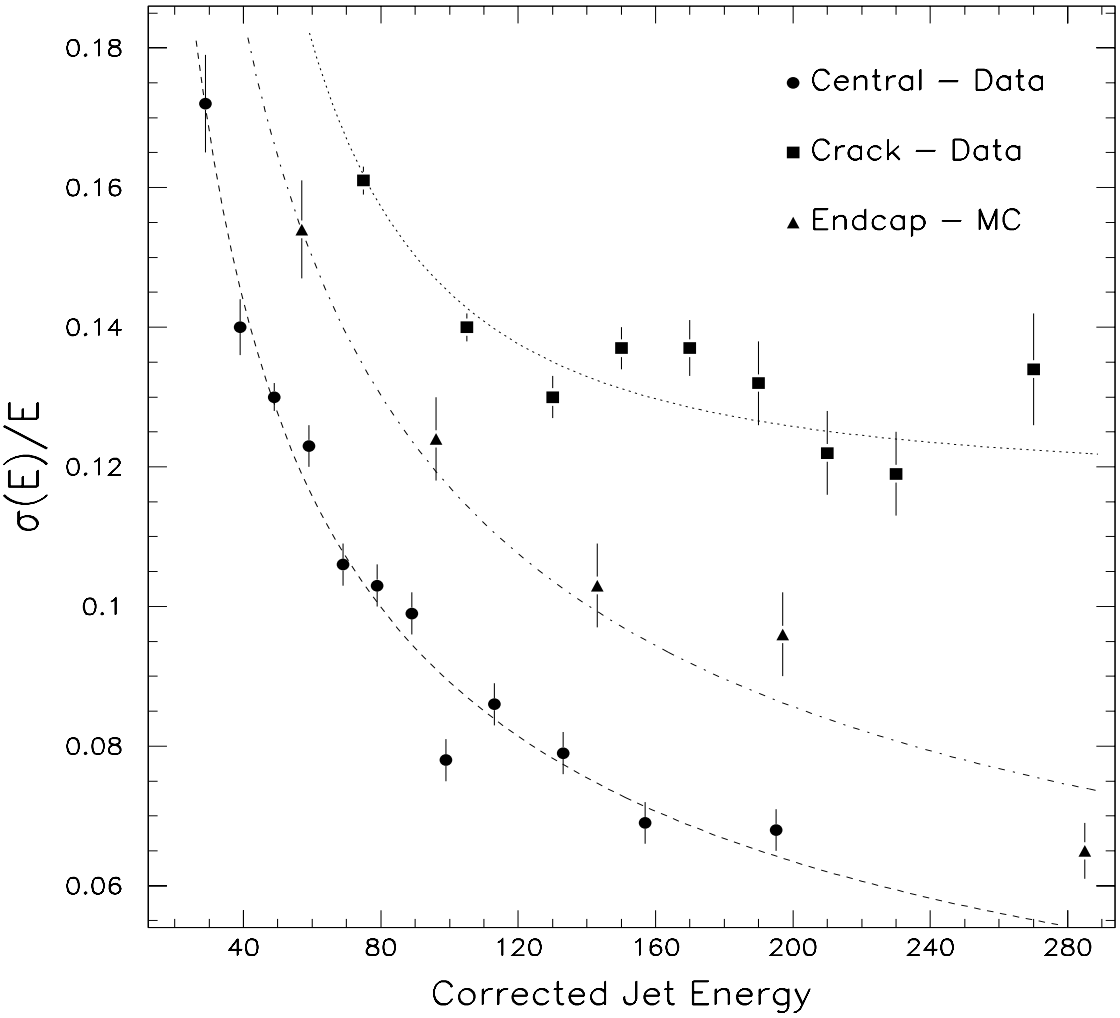

Figure 4.3: The jet E_T resolutions in CC, EC and ICD as functions of E_T.

4.3 $\vec{\not\!\!E}_T$ (Neutrinos)

4.3.1 Definition

The first calculation of $\vec{\not\!\!E}_T$ is done at L2 using an algorithm based on a vector sum of the contributions from all calorimeter channels [83]. The correction for the position of the interaction vertex is made on the basis of a fast vertex determination at LØ.

Attributing the energy deposited in each cell of the calorimeter to a massless particle, DØRECO computes the 4-vector for each cell using its coordinates and those of the reconstructed primary vertex. These 4-vectors are then added up for all the cells in the calorimeter. The negative of the component of this total 4-vector that is perpendicular to the z-axis is then termed "the calorimeter missing E_T" ($\vec{\not\!\!E}_{Tcal}$) so that if it were added as another object, the net E_T of the event, as far as the calorimeter is concerned, would be zero. To obtain the total $\vec{\not\!\!E}_T$, the 4-vectors of certified muons are also included in the summation of 4-vectors described above.

4.3.2 Correction

After correcting the jets as described in section 4.2.2, a concurrent correction has to be made to the $\vec{\not\!\!E}_T$. This is a straight-forward task: the corrections made to the jet 4-vectors are summed and the negative of the transverse component of the sum is added to the pre-correction $\vec{\not\!\!E}_T$ to obtain the corrected $\vec{\not\!\!E}_T$ [84].

4.3.3 Resolution

The resolution of the calorimeter $\not\!\!E_T$ ($\sigma_{\not\!\!E_{T\ cal}}$) can be parametrized using dijet data as a function of the scalar sum of the E_T of the event, S_T:

$$\sigma_{\not\!\!E_{T\ cal}} = a + b \cdot S_T + c \cdot S_T^2 \tag{4.16}$$

where

$$a = (1.89 \pm 0.05)\ \text{GeV} \tag{4.17}$$

$$b = (6.7 \pm 0.7) \times 10^{-3} \tag{4.18}$$

and

$$c = (9.9 \pm 2.1) \times 10^{-6}\ \text{GeV}^{-1} \tag{4.19}$$

$\sigma_{\not\!\!E_{T\ cal}}$ determined using QCD dijet events is shown as a function of S_T in Figure 4.4 [85].

The resolution of the total (muon-corrected) $\vec{\not\!\!E}_T$ is clearly dominated by muon momentum resolution if there are high-p_T muons found in the event. Fortunately, we do not have to deal with such events.

Region of the Calorimeter	C	S ($\sqrt{\text{GeV}}$)	N (GeV)
$\mid \eta \mid < 0.8$ (CC)	0.016	0.86	1.74
$0.8 < \mid \eta \mid < 1.5$ (ICD)	0.117	1.35	7.81
$1.5 < \mid \eta \mid < 3.0$ (EC)	0.034	1.10	1.97

Table 4.1: Parameters of the fit to the jet energy resolution for the three regions of the calorimeter.

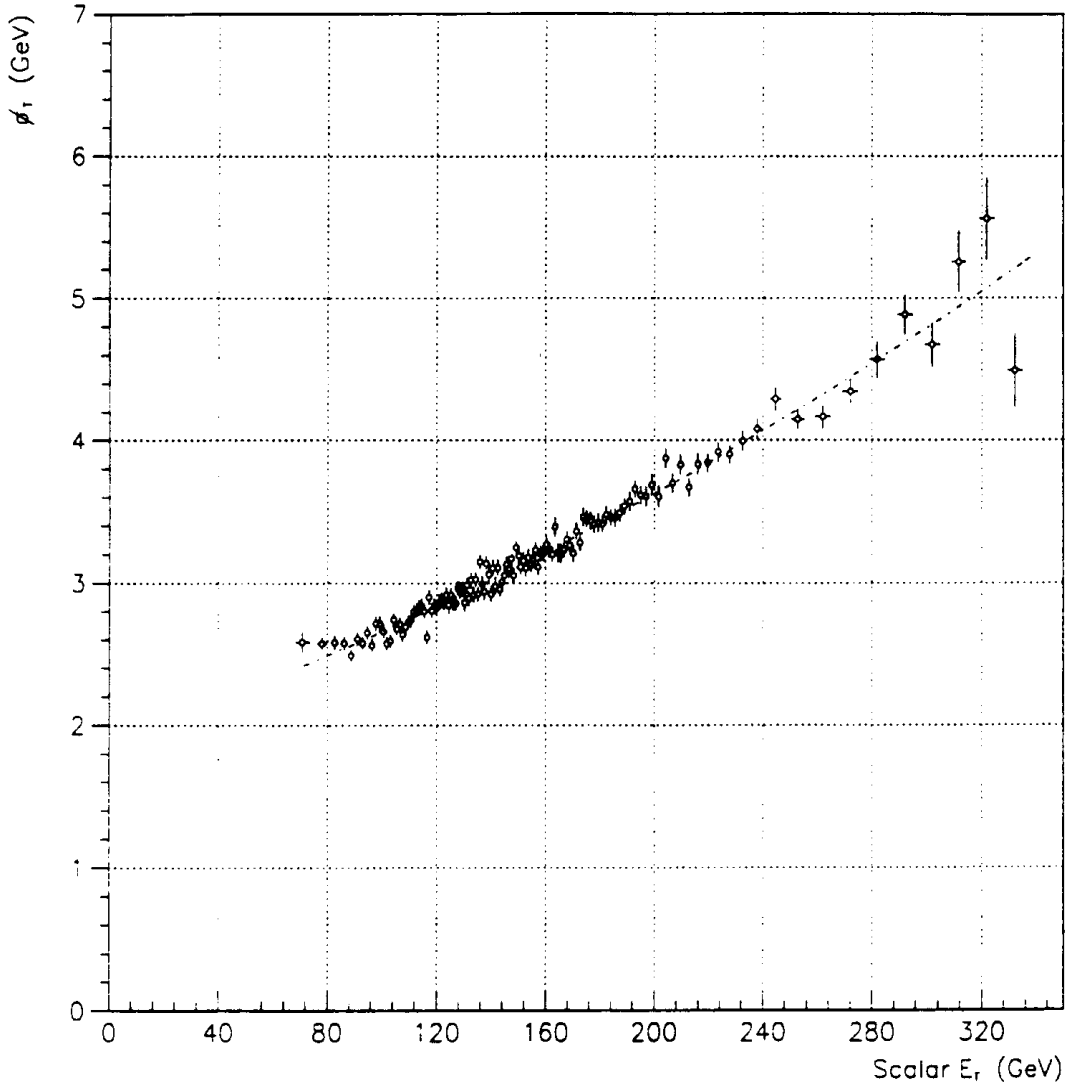

Figure 4.4: The $\not\!\!E_T$ resolution of the DØ calorimeter as a function of the total scalar E_T (S_T) of an event.

Chapter 5

Modelling the signal and the backgrounds

Let S and B be two sets of processes such that

$$S \cup B = \Omega \tag{5.1}$$

$$S \cap B = \Phi \tag{5.2}$$

where Ω and Φ represent the sample set and the null set respectively. Suppose $\rho_C(\vec{p})$ is the observed density of states at the point $\vec{p}$ of phase space for class C. Then

$$\rho_S(\vec{p}) + \rho_B(\vec{p}) = \rho_\Omega(\vec{p}) \tag{5.3}$$

By definition, if S represents our signal, B represents the background. $\rho_\Omega(\vec{p})$ is an observable; we seek to determine $\rho_S(\vec{p})$. The cross-section of the process C is defined as

$$\sigma_C \equiv N \cdot \int_{\vec{p}} \rho_C(\vec{p})\ d\vec{p} \tag{5.4}$$

Where N is an arbitrary constant containing all the dimensional units.

In the limit of infinite population, we would like to narrow our search down to the point $\vec{p}_0$ where $\frac{\rho_S(\vec{p})}{\rho_B(\vec{p})}$ is maximum if we knew $\rho_B(\vec{p})$. Limited

statistics forces us to extend our search over a large range of $\vec{p}$. Besides, we do not know $\rho_B(\vec{p})$ very well. Whatever the statistics may be, we need to have a good idea of the underlying distributions in order to focus our search in the right region of the phase space. Given a theoretical model, the determination of $\vec{p}_0$ is, in principle, a straightforward analytical exercise. To see the real challenge we face, let us express the density of states at point $\vec{p}$ as

$$\rho_C(\vec{p}) = W_C \ \xi_C(\vec{p}) \tag{5.5}$$

where W_C is a normalizing function such that $\mathcal{R}(\vec{p}_0) = 1$ where $\mathcal{R}(\vec{p}) \equiv \frac{\xi_S(\vec{p})}{\xi_B(\vec{p})}$. Our current theoretical knowledge lets us predict $\xi_C(\vec{p})$ much more accurately than W_C. In other words, we have more faith in our knowledge of the relative distributions than in that of the absolute cross-sections. To determine $\rho_S(\vec{p})$, we thus use the theoretical predictions for $\xi_S(\vec{p})$ and $\xi_B(\vec{p})$. If $\mathcal{R}(\vec{p})$ has a reasonably strong dependence on $\vec{p}$, then we can determine W_S and W_B by varying $\vec{p}$.

Whatever the means, our first task is to model $\xi_S(\vec{p})$ and $\xi_B(\vec{p})$ the best we can and to prepare a large sample of simulated signal and background events using those models. The next task, namely the analysis, consists of comparing these samples with data at different points of the phase space which leads us to the conclusions. To this end, a common practice is to use Monte Carlo (MC) event generators i.e., programs which randomly populate the phase space with events of a given kind according to a density function dictated by the theoretical model of choice. In principle, one can have virtually unlimited statistics using MC's, which is the strength of MC-based estimates. The weakness is the

cautionary reminder at the bottom: it is only as good as the theoretical model driving it, i.e. "garbage in, garbage out". For our signal, we do not have much of a choice, but for backgrounds, there are some options. As remarked earlier, our background has two components:

(a) the continuum production of W + *jets* events, which we shall henceforth refer to as the "W background" and

(b) the background due to imperfect instrumentation which we shall henceforth refer to as the "non-W background".

For the W background, we can and do go up to a certain point applying some simple theoretical extrapolations from our data away from $\vec{p}_0$ to $\vec{p}_0$, not using any MC at all. After this point, MC gives us a better handle. For the non-W background, it turns out that we can do very well without MC. We have a large sample of the events, a small fraction of which mimics our signal due to measurement fluctuations. Using this sample, we can estimate the non-W background to good accuracy.

This chapter describes how we prepare the samples of simulated signal and background events needed for our analysis. In the first section, we talk about the Monte Carlo samples and in the second, the samples derived from our data.

5.1 Simulation of events using Monte Carlo

We use MC to generate simulated samples of our signal and the W background events. All of our studies of the signal and much of our studies of

the W background are based on these samples. To reach the stage where an MC event can be treated in the same way as our data, one has to go through several steps:

- generation of a hard-scattering process at the parton level (ISAJET for signal ($t\bar{t}$), VECBOS for the W background,
- QCD evolution which allows further branching of the partons (ISAJET).
- fragmentation of the partons to a final state containing particles that hit the detector (ISAJET),
- addition of the rest of the beam-beam interaction that does not involve any hard-scattering (ISAJET),
- simulation of the response of the detector to the particles (DØGEANT), and finally,
- simulation of the data acquisition process (TRIGSIM).

In parenthesis above are the programs that we use in the exercise. This section contains the highlights of each of these programs.

5.1.1 ISAJET

ISAJET is a Monte Carlo program which simulates pp and $p\bar{p}$ interactions at high energy [86]. It is based on perturbative QCD (PQCD) plus phenomenological models for parton and beam jet fragmentation. Events are generated in four distinct steps (the first four in the above list):

- a primary hard-scattering is generated according to the appropriate QCD cross-section,
- QCD radiative corrections are added taking into account both the initial and the final states,
- partons are fragmented into hadrons independently, and hadrons with lifetime less than $\sim 10^{-12}$ s are decayed,
- beam jets are added assuming that these are identical to a minimum bias event at the remaining energy.

In this analysis, the parton-generating part of ISAJET is used only for signal, i.e. the $t\bar{t}$ events. The part that does the fragmentation and addition of underlying beam-beam interaction is used both for signal and for background.

Parton generation

The primary hard-scattering process is generated according to the general form

$$\sigma = \sigma_0 \cdot F(x_1, Q^2) \cdot F(x_2, Q^2) \tag{5.6}$$

where σ_0 is the appropriate cross-section calculated by perturbative QCD and $F(x, Q^2)$ is the structure function incorporating the leading-log QCD scaling violations, x_1 and x_2 are the fractions of the hadron momenta carried by the colliding partons and Q^2 represents the scale of the momentum-transfer. For each process included in ISAJET, the basic cross-section σ_0 corresponds to a two-body process. The user can define the phase space and the type for each

of the two primary jets. For our analysis, we use two-jet events restricting the outcome of the hard-scattering process to $t\bar{t}$.

To avoid collinear and infrared singularities, each parton in a process is required to have a mass larger than some cut-off threshold. In ISAJET, this threshold is hard-coded at 6 GeV, a rather large value. It is assumed that all physics at lower scales is incorporated in the jet fragmentation stage which is modeled independently. The high threshold cuts off the radiation of soft gluons. To compensate for this, equal and opposite transverse boosts are applied to the two-jet system and to the beam-jets after fragmentation with a mean value

$$\langle p_T^2 \rangle = \sqrt{Q^2} \times 0.1 \text{ GeV} \tag{5.7}$$

Jet fragmentation and addition of underlying beam-beam interactions

ISAJET evolves the primary partons through repeated branchings via bremsstrahlung and pair production according to the generally accepted QCD formalism using the Altarelli-Parisi splitting functions [87]. Following this, the quarks and the gluons are fragmented into hadronic final states using the independent fragmentation ansatz of Field and Feynman [88]. Such a scheme can model the fast hadrons in a jet satisfactorily but fails to conserve energy or flavor exactly. Energy conservation is imposed after the event is generated by boosting the hadrons to the appropriate rest-frame, rescaling all of the three-momenta and recalculating the energies.

Following the experimental observation of differences between beam-jets

in hard-scattering events and those in minimum-bias events, ISAJET uses an algorithm similar to the one used for generating minimum-bias events in order to simulate the underlying "spectator" event but with a different set of parameters. To bolster our confidence in the Monte Carlo, we have compared with another popular one, namely HERWIG. Figure 5.1 shows some of the results of the comparison:

(a) E_T of the $3^{\rm rd}$ jet (ranked in E_T),

(b) E_T of the $4^{\rm th}$ jet (ranked in E_T),

(c) H_T (see Subsection 6.3.2) and

(d) Aplanarity ($\mathcal{A}$) (see Subsection 6.3.1). We see that there is no significant disagreement between the two Monte Carlos. The cut $H_T > 140$ GeV (see section 6.4) is slightly more efficient for HERWIG compared to ISAJET. The cuts we use on the rest of the variables yield almost identical efficiencies.

5.1.2 VECBOS

To generate W + *jets* samples, which is the primary source of physical background to our signal, we use the VECBOS Monte Carlo program [89] [1]). VECBOS offers leading order parton-level calculations using the exact matrix elements for IWB + n *jet* processes for $0 \leq n \leq 4$ (where IWB stands for a "Intermediate Weak Boson", i.e. a W or a Z), generating events with a single specified value of n at a time. The jets refer to QCD partons, so the calculations are carried out at the tree-level in the order α_s^n. Also, the IWB

[1] See reference [90] for the details of the implementation of VECBOS at DØ

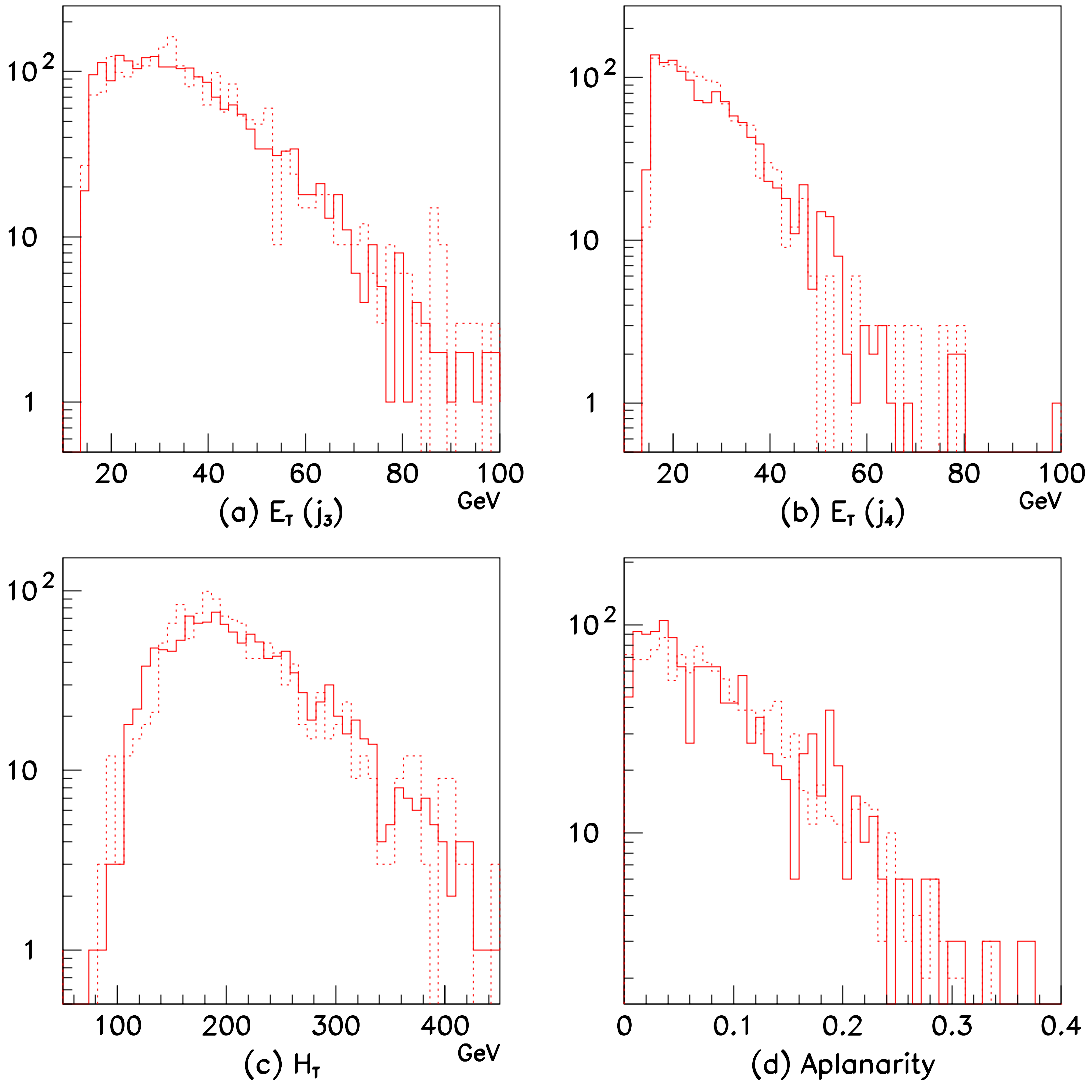

Figure 5.1: Comparison between ISAJET (solid lines) and HERWIG (dotted lines) $t\bar{t}$ events after full detector simulation (M_t = 160 GeV): (a) $E_T(j_3)$; (b) $E_T(j_4)$; (c) H_T and (d) Aplanarity ($\mathcal{A}$).

is decayed leptonically by VECBOS.

VECBOS uses the VEGAS program to integrate over the multidimensional phase space of the partons [91][92]. It is to be noted here that the calculations performed by VECBOS are based solely on the formalism of PQCD. Its accuracy is thus determined by the validity of the assumptions of PQCD. Therefore, the user has to exercise caution in defining and limiting himself to the part of the phase space where those assumptions hold reasonably well. This is done by setting minimum thresholds for the E_T's of and the separations between the jets carefully so as to remain safely away from the regions of soft and collinear extremes of radiation where PQCD is known to diverge. The higher order processes that cancel the soft and the collinear pieces are not incorporated in VECBOS. For our analysis, we required $E_T > 10$ GeV for all the final-state partons and $\Delta R \equiv \sqrt{\Delta\eta^2 + \Delta\phi^2} > 0.5$ for every pair of jets. From the available options, we chose the CTEQ1M for structure functions and $\langle Q^2 \rangle = M_W^2$ for the dynamical scale. Since VECBOS does not assign unique identification to the partons, we treat them all as gluons.

Before proceeding any further with a set of events generated by VECBOS, we perform an important operation, called "reweighting", on the sample. A few comments directed towards this procedure are in order. The distribution of $\frac{d\sigma}{d(LIPS)}$ is extremely non-uniform over the available LIPS (Lorentz Invariant Phase Space) for $W + nj$ events at high values of n. For $n = 4$, the difference between the maximum and the minimum can be several orders of magnitude. Hence, one would have to generate an enormous number of events to have a few

to study in the regions where $\frac{d\sigma}{d(LIPS)}$ is small. The authors of VECBOS didn't want to do this as it would be a waste of resources for their purpose of theoretical studies. So, they adopted the following solution: they generated events more or less uniformly over the specified LIPS assigning each event a weight proportional to its $\frac{d\sigma}{d(LIPS)}$ [93]. When we, the experimentalists requested a modification to have more events in the regions of high $\frac{d\sigma}{d(LIPS)}$ than at low, a single-parameter importance sampling scheme was incorporated. This improved the situation somewhat, but not quite enough. We wanted to be able to treat all the events on an equal footing, i.e., we didn't want to use a different weight for each event which requires more computing resources than what is available to us. We could put only a few thousand events through detector simulation and as we apply the offline cuts, only a handful survive. The high weight events stick out like needles in all distributions making it difficult to draw conclusions from them. So, we applied our own bit of importance sampling which is based on the shape of the weight distribution itself. The problem with this is that to do it in a completely unbiased way, we need enormous numbers of events to start with (precisely, we are trying to get into the situation requiring statistics that the authors of the program endeavored to work around). Hence, we adopted an interim solution: we accepted all events above a certain percentile rank in weight in the sample while for the rest, the weight curve was used for conventional importance sampling. For example, for the original $W + 3j$ sample generated by VECBOS, the qualifying minimum percentile rank for an automatic pass was set at 70 which corresponded (approximately) to a weight of 3.5×10^{-7} (70% of the events had a weight

less than 3.5×10^{-7}, see Figure 5.2a). For reweighting, a random number was generated with a uniform distribution between 0 and 3.5×10^{-7}. If the weight of the event was larger than the random number, the event was accepted, otherwise it was rejected. Note any event ranked higher than 70 percentile would necessarily pass since its weight is larger than 3.5×10^{-7}. Finally, all the events that passed (i.e. were accepted) were given the same weight. For $W + 0j$, the minimum percentile rank for an automatic pass was set at 99, (i.e. there we could afford a really unbiased sampling) while for $W + 4j$, we had to settle for 60. There are some valid objections to this scheme, but with the available resources, this is the best we could do. Figures 5.2a and 5.2b show the weight distributions for $W + 3j$ and $W + 4j$ events respectively (the unit of horizontal scale is arbitrary). The solid lines correspond to the weights of all the events originally produced by VECBOS. The dotted lines correspond to the original weights of the events which were retained after reweighting. By reweighting, all of these events were given a single weight which is the expectation value of their original weights. The point where the solid and the dotted lines merge shows the weight above which all events were accepted (70 percentile rank for $W + 3j$, 60 for $W + 4j$). Notice the overflows in the histograms. The event with the maximum weight has a weight of $\sim 2.6 \times 10^{-4}$ for $W + 4j$. The maximum of the horizontal scale of the histogram was set at $\frac{1}{500}$ of that value in order to make the difference between the pre-and post-reweighting curves visible. As another measure of the extreme spread of VECBOS weights in the $W + 4j$ sample before reweighting, more than 50% of the total weight comes from the top 1% of the events. We note how the skewness of the distribution

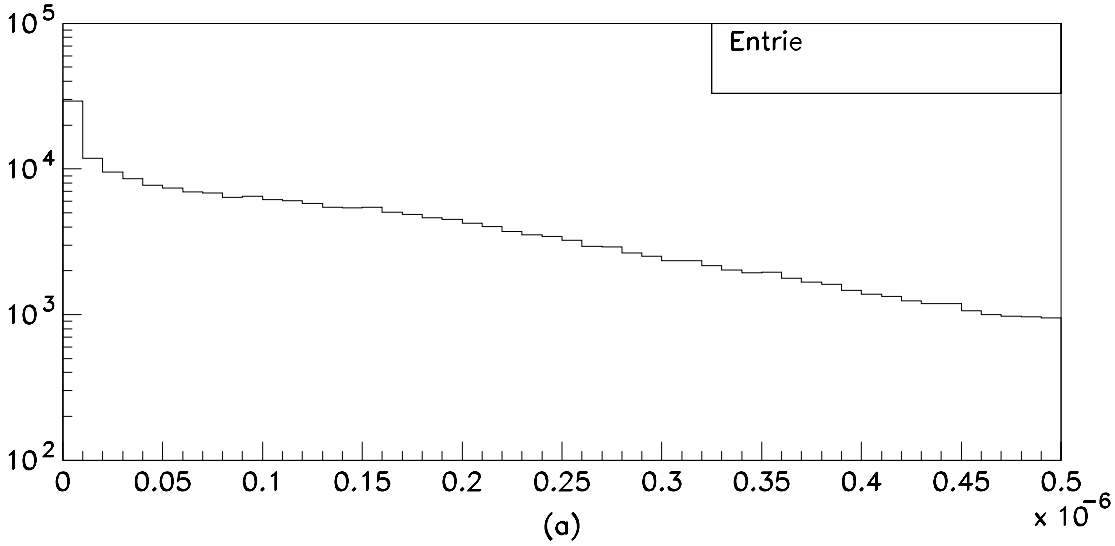

(a)

Chapter 7

Conclusion

The important conclusion to be drawn from the results of our analysis is the estimate for the cross-section for the production of t quark at the Tevatron. We address this issue in the first section. The second section contains some closing comments on the state of affairs.

7.1 *top* quark production cross-section

The estimate for the number of signal events in our data (N) combined with the knowledge of efficiency (ε, in which the branching ratio is included) and the total integrated luminosity (L) can be readily translated into an estimate for the cross-section (σ):

$$\sigma = \frac{N}{\varepsilon \cdot L} \tag{7.1}$$

The total integrated luminosity corresponding to our data is

$$L \equiv \int \mathcal{L} dt = 13.5 \pm 1.6 \text{ pb}^{-1} \tag{7.2}$$

where $\mathcal{L}$ stands for the instantaneous luminosity. The efficiency is estimated using the Monte Carlo sample. For $M_t = 160$ GeV, we have $\varepsilon = 0.027 \pm 0.005$ for methods A and B and $\varepsilon' = 0.016 \pm 0.004$ for method C. In addition to these, we include the systematic uncertainties in the jet energy scale ($\sim 20\%$) and the acceptance of our signal ($\sim$ 20%) for either method. For Method A, an additional $\sim$ 16% error comes from the quality of the exponential fit (this can be identified with the systematic uncertainty in the Berend's scaling rule). For Method B also, there's a systematic error associated with the fitting procedure. This is estimated to be $\sim$ 26% based on the quality of the least-square fit (at the minimum, we have $\chi^2 = 5.1$ for 4 degrees of freedom). The systematic errors are added in quadrature.

We can thus estimate the cross section from each of the three methods described in the last chapter:

$$\sigma^A(t\bar{t}) = 8.0 \ \pm 7.7 \ \pm 2.7 \text{ pb} \tag{7.3}$$

$$\sigma^B(t\bar{t}) = 5.1 \ \pm 7.9 \ \pm 2.1 \text{ pb} \tag{7.4}$$

$$\sigma^C(t\bar{t}) = 3.7 \ \pm 12.6 \ \pm 2.0 \text{ pb} \tag{7.5}$$

where, the first set of errors is the statistical and the second, the systematic component of the total uncertainty. These cross-sections have been evaluated using $M_t = 160$ GeV in the Monte Carlo. The estimates are not terribly sensitive to M_t in our range of interest, changing by less than 20% for a 20 GeV shift in either direction. These cross-sections are to be compared with the theoretical prediction of

$$\sigma(t\bar{t}) = 7.41^{+1.37}_{-0.55} \text{ pb} \tag{7.6}$$

For the upper limit to the cross-section, we use only the cleanest (and smallest) sample, i.e. method C:

$$\sigma^C(t\bar{t}) < 28.2 \text{ pb} \quad (95\% \text{ C.L.}) \tag{7.7}$$

7.2 Remarks

Thanks to the large uncertainties, the results obtained in this thesis are consistent with the Standard Model prediction as well as the recent CDF results quoted in Chapter 1. For better or for worse, the results are also consistent with the scenario of there being no t quark with a mass below the upper limit in those predictions.

We have not attempted to calculate a lower limit for the mass of the t quark just from this channel. However, the final state we have studied is a key contributor to the analysis that combines several other channels. We have not discussed in this thesis, the details of our analysis of the $e + \not\!\!E_T + jets$ channel that, combined with the $\mu + \not\!\!E_T + jets$, $e + \mu$ and $e + e$ channels, led us to the deduction of the current lower limit on M_t, mainly because of the large overlap it has with what we have presented here. In that analysis, we used basically the same set of variables although the cuts were different owing to the dependence of the dynamics and cross-section on M_t. The analysis methods were less developed at that point and we did not have enough confidence in our estimates for backgrounds to subtract them from the observed data. The search was focused at the range of M_t immediately above the then-current lower limit of 91 GeV. Having established a new lower limit from that analysis,

here we have focused on the region above it. Presently, DØ has results from all channels that involve at least one e or μ in the final state based on the same data set as the one used here. These results will soon be published [106]. The current estimate for the cross-section from the DØ data (all channels combined) stands at

$$\sigma_{t\bar{t}} = 7.2 \pm 5.4 \text{ pb} \tag{7.8}$$

The number of approaches presented here may seem too many for the available data. However, our aim has been to develop analysis techniques that will be useful in the long run. We note that the uncertainties are by far dominated by the statistical component. For a good while, the precision of the predictions made by these techniques will grow steadily with the size of our data sample even if no further reduction is achieved in the systematic uncertainties. Of course, our understanding of the detector performance in real life as well as in Monte Carlo simulation will grow with time. Much effort is being invested to attain this objective which will allow us to be more precise in our statements about the systematic effects as well in near future.

There are also other (more sophisticated) techniques to examine the data at hand. These include covariance matrix [107], Probability Density Estimators (PDE) [108] and Neural Networks [109]. Reference [110] contains a brief account of the working principle of these techniques which are better suited to approach the theoretical maximum for the discrimination between signal and background. However, our studies along these lines are not yet mature enough to be used for a prediction of cross-section. A better understanding of the sys-

tematics of these techniques is required before they can serve as "standard". Intensive studies are currently under way to achieve this end.

Finally, it is interesting to note that BR($b \rightarrow \mu + X$) $\approx$ 0.22 (inclusive). For high-p_T b jets, a muon from the b decay is expected to be embedded in the jet. Unlike the backgrounds, our signal always has two b quarks in the partonic final state. Hence, the probability of at least one of them containing a muon in its decay products is 0.44. Although the ability of the DØ detector to detect such muons is not particularly high, it is good enough to seduce people into studying only those events which have jets tagged with non-isolated muons. It is therefore only natural to ask if any of the 8 events in our 4-jet sample used in Methods A and B have a muon in it. The answer is "No".

Bibliography

[1] J. Thomson, Philosophical Magazine, vol. 44, series 5, 293 (1897).

[2] J. Chadwick, Nature, **129**, 312 (1932).

[3] J. Chadwick, Verh. d. Deutschen Phys. Ges., **16**, 383 (1914)

[4] N. Bohr, Philosophical Magazine, **26**, 1 (1913).

[5] P. A. M. Dirac, Proc. R. Soc., London **A114** 243, 710 (1927).

[6] R. P. Feynman, Phys. Rev., **76**, 749 (1949).

[7] R. P. Feynman, Phys. Rev., **76**, 769 (1949).

[8] W. Heisenberg, Z. Phys., **77**, 1 (1932).

[9] E. Fermi, Z. Phys., **88**, 161 (1934).

[10] Y. Yukawa Proc. Phys. -Math. Soc., Japan, **17**, 48 (1935).

[11] M. Gell-Mann, Phys. Lett., **8**, 214 (1964).

[12] G. Zweig, CERN report No. 8182/TH401 (1964).

[13] C. N. Yang and R. L. Mills, Phys. Rev., **96**, 191 (1954).

[14] T. D. Lee and C. N. Yang, Phys. Rev., **104**, 254 (1956).

[15] C. S. Wu *et al.* Phys. Rev., **105**, 1413 (1957).

[16] E. C.G .Sudarshan and R. E. Marshak, Phys. Rev., **109**, 1860 (1958).

[17] M. Gell-Mann and R. P. Feynman, Phys. Rev., **109**, 193 (1958).

[18] S. L. Glashow, Nucl. Phys., **22**, 579 (1961).

[19] S. Weinberg, Phys. Rev. Lett., **19**, 1264 (1967).

[20] A. Salam in "Elementary Particle Theory", Ed. N. Svartholm (Almqvist and Wiksell, 1969) p. 367.

[21] Gargamelle Experiment, F. J. Hasert *et al.* Phys. Lett., **46B**, 138 (1973).

[22] UA1 Collaboration, Phys. Lett., **122B**, 103 (1983).

[23] UA2 Collaboration, Phys. Lett., **122B**, 476 (1983).

[24] UA1 Collaboration, Phys. Lett., **126B**, 398 (1983).

[25] UA2 Collaboration, Phys. Lett., **129B**, 130 (1983).

[26] P. D. B. Collins, A. D. Martin and E. J. Squires, "Particle Physics and Cosmology", (John Wiley and Sons, 1989).

[27] C. Quigg, "Gauge Theories of the Strong, Weak and Electromagnetic Interactions", (Benjamin Cummings Publishing Co., 1983)

[28] I. J. R. Aitchison and A. J. G. Hey, "Gauge Theories in Particle Physics", (Adam Hilger, Philadelphia, 1989).

[29] M. Kobayashi and M. Maskawa, Prog. Theor. Phys., **49**, 652 (1953).

[30] Particle Data Group (L. Montanet *et al.*), "Review of Particle Properties", Phys. Rev. D, **50**, 1233 (1994).

[31] S. Glashow, J. Iliopoulos and L. Maiani, Phys. Rev., **D2**, 1285 (1970).

[32] P. W. Higgs, Phys. Rev. Lett., **12**, 132 (1964).

[33] P. W. Higgs, Phys. Rev., **145**, 1156 (1966).

[34] Particle Data Group (L. Montanet *et al.*), "Review of Particle Properties", Phys. Rev. D, **50**, 1191 (1994).

[35] G. L. Kane, "Top Quark Physics", (Invited lecture at the workshop on High Energy Phenomenology, Mexico City) (1991)
Also available as a University of Michigan preprint (UM – TH – 91 – 32).

[36] The LEP collaborations ALEPH, DELPHI, L3, OPAL and the LEP Electroweak Working Group, LEPEWWG/94-02, (1994) (unpublished) (Presented by D. Schaile at the 27^{th} international conference on High Energy Physics, Glasgow, July 1994).

[37] CDF Collaboration, F. Abe *et al.*, Phys. Rev. D., **45**, 3921 (1992).

[38] DØ Collaboration, S. Abachi *et al.*, Phys. Rev. Lett., **72**, 2138 (1994).

[39] CDF Collaboration, F. Abe *et al.*, Phys. Rev. D, **50**, 2966 (1992).

[40] Particle Data Group (L. Montanet *et al.*), "Review of Particle Properties", Phys. Rev. D, **50**, 1195 (1994).

[41] E. Laenen, J. Smith and W. van Neerven, Phys. Lett. B, **321**, 254 (1994).

[42] Particle Data Group (L. Montanet *et al.*), "Review of Particle Properties", Phys. Rev. D, **50**, 1315 (1994).

[43] Particle Data Group (L. Montanet *et al.*), "Review of Particle Properties", Phys. Rev. D, **50**, 1173 (1994).

[44] C. Hill, and S. Parke, "Top Production: Sensivity to New Physics", (Presented at the 27^{th} international conference on High Energy Physics, Glasgow, July 1994).

[45] J. Thompson, Ph. D. Thesis, State University of New York at Stony Brook, "Search for top quark in the Muon + Jets channel at DØ " (February 1994) (unpublished).

[46] "Design Report, Tevatron 1 Project", Fermi National Laboratory internal note (1984) (unpublished) .

[47] DØ collaboration, S. Abachi *et al.*, Nucl. Instrum. and Methods, **A338**, 185 (1994).

[48] F. Sauli, "Principles of operation of Multiwire Proportional and Drift Chambers" in "Experimental Techniques in High Energy Physics", Ed. T. Ferbel (Addison-Wesley Publishing Co., 1987) p. 79-188.

[49] R. Fernow, "Introduction to Experimental Partcle Physics", (Cambridge University Press, 1986) p. 234.

[50] A. R. Clark *et al.*, Nucl. Instrum. and Methods, **A279**, 245 (1989).

[51] J. Cochran, Ph. D. Thesis, State University of New York at Stony Brook, "Search for Truth the $e\mu$ channel at DØ " (December 1993) (unpublished).

[52] T. Behnke, Ph. D thesis, State University of New York at Stony Brook, "The Central Tracking Chamber for the DØ Experiment: Design, Construction, and Test" (August 1989) (unpublished).

[53] Dominico Pizzuto, Ph. D thesis, State University of New York at Stony Brook, "DØ central tracking chamber performance studies" (December 1991) (unpublished).

[54] D. Chakraborty and R. Engelmann, "Performance and Monitoring of the Central Drift Chamber of DØ : An overview based on the 1991 Cosmic Ray data", DØ internal note 1438 (1992) (unpublished).

[55] S. Rajagopalan, Ph. D. thesis, Northwestern University, "The $\frac{dE}{dx}$ capabilities of the DØ tracking system" (June 1992) (unpublished).

[56] J. Bantly, Ph. D. thesis, Northwestern University, "The DØ detector Forward Drift Chamber Performance and Physics Capability in the 1990 FNAL Testbeam Run" (June 1992) (unpublished).

[57] R. Fernow, "Introduction to Experimental Partcle Physics", (Cambridge University Press, 1986) p. 294.

[58] F. Feinstein, Ph. D. A'l'Universite de Paris-Sud, Centre d'Orsay, "Atude d'un Detecteur a Rayonnement de Transition pour l'Experience DØ au

FNAL" (December 1987) (unpublished).

[59] R. Fernow, "Introduction to Experimental Partcle Physics", (Cambridge University Press, 1986) p. 259.

[60] J. Kotcher, Ph. D. thesis, New York University, "Response of the DØ Calorimeter to cosmic ray muons" (October 1992) (unpublished).

[61] J. E. Brau and K. Furuno, "Hadron Calorimetry — Optimizing Performance" (Presented at the 1st International Conference on Calorimetry in High Energy Physics, FNAL, October 1990, Proceedings Ed. D. Anderson *et al.*, World Scientific, p. 3) This publication also has several illuminating articles on the DØ calorimeter.

[62] S. Aronson *et al.* Nucl. Instrum. and Methods, **A269**, 492 (1988).

[63] J. Yu, Ph. D. Thesis, State University of New York at Stony Brook, "Determination of the Strong Coupling Constant (α_s and a test of Perturbative QCD Using $W+$ Jet Processes in the DØ Detector" (August 1993) (unpublished).

[64] D. Hedin, Private Communication.

[65] J. Linnemann, "Triggering the DØ experiment", in "The Fermilab Meeting", DPF '92, vol. 2, 1642 (1992).

[66] F. Nang and R. Partridge, "Level 0 detector layout", DØ internal note 998 (1990) (unpublished).

[67] J. Bantly *et al.*, "The Level 0 trigger for the DØ detector", DØ internal note 1996 (1990) (unpublished, submitted to IEEE Trans. Nucl. Sci.).

[68] P. Laurens, "First level trigger data block description", `DO$LEVEL1:DO_NOTE_967.DOC`, DØ online documentation (1993) (unpublished).

[69] J. Hoftun, "Level 2 System, Programmer and User Manual", `DO$DOCS:LEVEL2_MANUAL.MEM`, DØ online documentation (1992) (unpublished).

[70] "List of locations of available documentation on existing Level 2 tools", `DO$DOCS:L2TOOLS.DOC`, DØ online documentation (1993) (unpublished).

[71] J. McKinley and J. Linnemann, "The level 2 electromagnetic cluster algorithm", `DO$CALOR_FILTER:L2_EM.DOC`, DØ online documentation (1993) (unpublished).

[72] S. Youssef, "Clustering with local equivalence relations", Computer Physics Comm. **45**, 423 (1987).

[73] DØ Collaboration, S. Abachi *et al.*, "Search for top quark in lepton+jets events", Phys. Rev. D. article in preparation (1994).

[74] R. Engelmann *et al.*, Nucl. Instrum. and Methods, **216**, 45 (1983).

[75] M. Narain, private communication.

[76] D. Chakraborty, M. Fatyga and M. Paterno, "CCEM Module Sampling Fractions and Uniformity of Response", DØ internal note 1375 (1992) (unpublished).

[77] Particle Data Group (L. Montanet *et al.*), "Review of Particle Properties", Phys. Rev. D, **50**, 1191 (1994).

[78] R. Astur, "The Level 2 jet algorithm", `DO$CALOR_FILTER:L2JETS.DOC`, DØ online documentation (1993) (unpublished).

[79] N. Hadley, "Cone Algorithm for jet-finding", DØ internal note 904 (1989) (unpublished).

[80] R. Astur, "Energy-scale corrections", DØ internal note 2089 (1994) (unpublished).

[81] R. Astur, R. Kehoe and A. Milder, "Determintation of hadronic energy scale corrections for the DØ experiment", DØ internal note in preparation (1994).

[82] CDF Collaboration, F. Abe *et al.*, Phys. Rev. Lett., **69**, 2896 (1992).

[83] J. White, J. Linnemann, M. Paterno and A. Boehnlein, "The Level 2 missing E_T algorithm", `DO$CALOR_FILTER:L2ETMISS.DOC`, DØ online documentation (1993) (unpublished).

[84] R. Astur, "Correction of $\not\!\!E_T$ " DØ internal note 2088 (1994) (unpublished).

[85] M. Paterno, "A study of the DØ calorimeter $\not\!\!E_T$ resolution using low E_T jet triggers", DØ internal note 1782 (1993) (unpublished).

[86] F. Paige and S. Protopopescu, BNL Report no. BNL38034 (1986) (unpublished), release v 6.49.

[87] G. Altarelli and G. Parisi, Nucl. Phys., **B126**, 298 (1977).

[88] R. D. Field and R. P. Feynman, Nucl. Phys., **B136**, 1 (1978).

[89] W. T. Giele, E. Glover and D. Kosower, Nucl. Phys., **B403**, 633 (1993).

[90] D. Chakraborty and Chip Stewart, "VECBOS at DØ : a sorcerer's manual", DØ internal note in preparation (1994).

[91] G. Peter Lepage, J. Comp. Phys., **27**, 192 (1978).

[92] G. Peter Lepage, "VEGAS - An adaptive multi-dimensional integration program", Cornell University preprint no. CLNS-18/447 (1980) (unpublished).

[93] W. T. Giele, private communication.

[94] S. D. Protopopescu, private communication.

[95] F. Carminati *et al.*, "GEANT Users' Guide", CERN Program Library, December 1991 (unpublished).

[96] A. Jonkheere, "DØGEANT user guide", DØ internal note 969 (1989) (unpublished).

[97] N. A. Graf, "The DØ Shower Library", (Presented at the 1^{st} International Conference on Calorimetry in High Energy Physics, FNAL, October 1990, Proceedings Ed. D. Anderson *et al.*, World Scientific, p. 539)

[98] "Level 1 simulator user's guide", `DO$LEVEL1:L1SIM.DOC`, DØ online documentation (1992) (unpublished).

[99] D. Claes, "Simulation of the Level 2 trigger", `DO$LEVEL2:L2SIM.DOC`, DØ online documentation (1994) (unpublished).

[100] D. Chakraborty and M. Fatyga, "QCD Backgrounds to $t\bar{t}\rightarrow e + jets$: A Study of fake electron probabilities", DØ internal note in preparation (1994).

[101] D. Chakraborty and M. Fatyga, "QCD Backgrounds to Electroweak Signals: A Study of fake electron and fake photon probabilities", DØ internal note 1753 (1993) (unpublished).

[102] M. Fortner, "Trigger list, version 7.2", DØNEWS 1265 (GENERAL), (1993) (unpublished).

[103] F. A. Berends, W. T. Giele, H. Kuijf and B. Tausk, Nucl. Phys., **B357**, 32 (1991).

[104] D. Chakraborty, "Harmonic Moments: an alternative shape-variable for $t\bar{t} \rightarrow lepton + jets$ analysis", DØ internal note 2337 (1994) (in preparation).

[105] V. D. Barger and R. J. N.Phillips, "Collider Physics", (Addison Wesley, Menlo Park, CA, 1989) p. 280.

[106] P. D. Grannis, "Search for the top quark: results from the DØ detector", (Presented at the 27^{th} international conference on High Energy Physics, Glasgow, July 1994).

[107] R. Raja, "A search for the top quark in the lepton + jets channel using Fisher Discriminants", DØ internal note in preparation.

[108] H. E. Miettinen, R. Ou, L. Holmstrom and S. Sain, "Searching for Top with Neural Nets. II. NN versus Probability Density Estimation", DØ internal note 1931 (1993) (unpublished).

[109] E. Amidi, P. Bhat, D. Chakraborty and H. Prosper, "Search for $t\bar{t}$ events in $e+jets$ channel using Neural Networks", DØ internal note 2334 (1994) (in preparation).

[110] P. Bhat, "Search for the top quark using multivariate analysis techniques", DØ internal note 2226 (1994) (Presented at the DPF meeting, Albuquerque, NM, August, 1994).